Mössbauer spectroscopy, nuclear inelastic scattering and density functional theory studies on oxobridged iron complexes and their reaction under Gif-type conditions

Von der Fakultät Chemie der Universität Stuttgart
zur Erlangung der Würde eines
Doktors der Naturwissenschaften (Dr. rer. nat.)
genehmigte Abhandlung

Vorgelegt von

Rajagopalan Subramanian

aus Mayiladuthurai, Indien

Hauptberichter: Priv.-Doz. Dr. Tanja Asthalter
Mitberichter: Prof. Dr. Emil Roduner
Mitprüferin und Prüfungsvorsitzende: Prof. Dr. Sabine Laschat

Tag der mündlichen Prüfung: 19 November 2010

Institut für Physikalische Chemie der Universität Stuttgart
2010

சிவன் அவன் என்சிந்தையுள் நின்ற அதனால்
அவன் அருளாலே அவன் தாள் வணங்கிச்
சிந்தை மகிழச் சிவ புராணம் தன்னை
முந்தை வினைமுழுதும் ஓய உரைப்பன் யான்

from Thiruvasagam by Saint Manikkavasagar

Because He, Civan, within my thought abides,
By His grace alone, bowing before His feet,
With joyous thought, Civan's ‘Ways of Old’ I'll tell,
That thus my former ‘deeds’ may wholly pass
translated by Rev. G. U. Pope

Abstract

This dissertation comprises studies of the Gif reaction of trinuclear oxobridged iron complexes aimed at predicting the intermediates formed during the Gif reaction. The experimental techniques used in these studies were ^{57}Fe transmission Mössbauer spectroscopy and synchrotron-based nuclear inelastic scattering (NIS). Quantum mechanical calculations based on density functional theory were also used to interpret the experimental results. Because NIS has rarely been applied to study catalytic reactions and nonheme and sulphur-free proteins with at least two iron centered complexes, we first used the Michael reaction to validate the reliability of the NIS technique before applying it to frozen solutions of the Gif reaction. The vibrational dynamics of another trinuclear oxobridged iron complex studied using the three above-mentioned methods together with Raman spectroscopy is also discussed in a separate chapter.

One chapter is dedicated to a discussion of the instrumentation of a ^{57}Fe transmission Mössbauer spectrometer built in the frame of this dissertation. This instrument can be used to analyze samples at room temperature with good instrumental resolution.

List of symbols and abbreviations

Symbols

α	Total internal conversion coefficient
α-Fe	Alpha iron foil (Metallic iron)
α_{K}	Internal conversion coefficient of electron in K-shell
β	$= 1/(k_{\mathrm{B}}T)$
β_{iso}	Isotopic abundance of Mössbauer nucleus
ΔE_{Q}, ϵ	Quadrupole splitting
ΔR	$= R_{\mathrm{e}} - R_{\mathrm{g}}$
Δx	Geometric thickness of absorber (sample)
δ	Isomer shift
$\delta(E)$	Dirac-δ function
$\delta_{\Gamma}(E)$	Lorentzian function of width Γ
η	Asymmetry parameter
η_{K}	K-shell fluorescence yield
γ	Gamma ray/radiation
Γ_{nat}, Γ	Natural and experimental line width, respectively
$\hat{I}$	Nuclear spin operator
$\hat{I}_x$, $\hat{I}_y$, $\hat{I}_z$	Nuclear spin component operator

λ	Wavelength of γ-ray
$\langle x^2 \rangle$	Mean square vibrational amplitude
$\mathcal{H}$	Hamiltonian
μ	Linear attenuation coefficient, also Nuclear magnetic dipole moment
$\mu_{\mathrm{e,\,g}}$	Nuclear magnetic dipole moments of nuclear excited (e) or ground (g) state
μ_{N}	Nuclear magneton
ν	Vibrational frequency
ω	Angular frequency
ω_{D}	Debye frequency
ω_{L}	Nuclear Larmor precession angular frequency
$\overline{v^2}$	Mean square velocity of nucleus
ϕ	Diameter of window of γ-ray detector
ρ	Mass density
ρ_{eff}	Effective area density of Mössbauer nuclei
σ_0, σ	Total and maximum cross section of resonance absorption, respectively
τ	Mean lifetime
τ_{e}	Electronic relaxation time
τ_{L}	$(= (\omega_{\mathrm{L}})^{-1})$ Nuclear Larmor precession time
θ_{D}	Debye temperature
^{57}Co	Cobalt nucleus with a mass number of 57 (radioactive isotope)
^{57}Fe	Iron nucleus with a mass number of 57
B	Baseline of Mössbauer spectrum

c	Speed of light in vacuum
d	Diameter of collimator
E	Energy relative to nuclear resonance
e	Proton charge
E_0	Nuclear transition energy in the absence of hyperfine interaction
E_j	Vibrational energy in j^{th} vibrational mode
e_j^2	Mode composition factor
E_γ	Energy of γ-radiation
e_{ac}^2	Acoustic mode composition factor
E_{D}	Doppler energy
$E_{\mathrm{e,\,g}}$	Nuclear excited (e) or ground (g) state energy
$E_{\mathrm{kin,\,pot}}$	Kinetic (kin) or potential (pot) energy of harmonic oscillator
e_{max}^2	Maximum possible mode composition factor
E_{Q}	Eigenvalues of electric quadrupole interaction
E_{R}	Recoil energy
$E_{\mathrm{S,\,A}}$	Nuclear transition energies in source (S) or absorber (A)
f, f_{LM}	Lamb-Mössbauer factor
$f_{\mathrm{a,\,s}}$	f of absorber (a) or source (s)
$g(\omega)$	Frequency distribution function of phonons (Debye model)
$g(E)$	Vibrational density of phonon states
$g_{\mathrm{e,\,g}}$	Gyromagnetic factor of nuclear excited (e) or ground (g) state
H	Magnitude of magnetic field vector

h	($= 2\pi\hbar$) Planck's constant
H_{int}	Internal magnetic field
I	Nuclear spin quantum number
$I(E)$	Flux of delayed K-fluorescence photons
I_0	Incident photon flux
$I_{\mathrm{e,\,g}}$	Nuclear spin quantum number of excite (e) or ground (g) state
$I'_{\mathrm{norm}}(E)$	Normalized NIS spectrum after removing elastic part
k	Magnitude of wavevector of γ-ray
k_{B}	Boltzmann constant
L	Length of collimator
l	Distance between source and absorber (sample)
M	Nuclear mass
m_I	Nuclear magnetic spin quantum number
$m_{\mathrm{Fe},\,k}$	Mass of iron (Fe) or k^{th} atom
M_{m}	Molar mass of Mössbauer isotope
M_{tot}	Mass of molecule
N	Number of atoms, also denoted for total number of channels
n	Quantum number or state, also used to denote alkyl spacer length
N_{A}	Avogadro's number
n_{B}	Bose occupation factor
N_{Fe}	Centre of reference (α-Fe) spectrum in channel number
n_{f}	Number of Mössbauer nuclei per molecule

$p_{1,\,6}$	Position of resonance lines 1 or 6
p_{n}, p	Magnitude of momentum of nucleus and γ-quantum, respectively
Q	Nuclear quadrupole moment
R	$(= (R_{\mathrm{e}} + R_{\mathrm{g}})/2)$ Mean nuclear radius
$R_{\mathrm{e,\,g}}$	Nuclear radius of excited (e) or ground (g) state
r_{eff}	Effective radius of detector window visible to source
S	Source strength, also spin state
$S(E)$	Normalized absorption probability per unit of energy
$S(t_{\mathrm{Pb}})$	Reduction in source strength due to lead shielding
S_{tot}	Total spin state
T	Temperature in Kelvin
t	Age of Mössbauer source
$T_{1/2}$	Half lifetime
t_{A}	Effective absorber thickness
$t_{\mathrm{Fe,\,Pb}}$	Thickness of iron (Fe) or lead (Pb)
$u^2_{\mathrm{Fe},j}$	Mean square vibrational displacement of Fe in j^{th} vibrational mode
$u^2_{k,j}$	Mean square vibrational displacement of k^{th} atom in j^{th} vibrational mode
v	Velocity of Mössbauer drive or nucleus
v_{R}	Recoil velocity
V_{zz}	Total effective EFG in principal axis system
Z	Atomic number
K-α	X-ray emission due to electronic transition from L- to K-shell

K-β	X-ray emission due to electronic transition from M- to K-shell
$\Psi(0)_{\mathrm{A,\,S}}$	Many-electron wave function at the Mössbauer nucleus of absorber (A) or source (S)

Abbreviations

APD	Avalanche photodiode
B3LYP	Becke 3-parameter (exchange), Lee, Yang, Parr (correlation)
BP86	Becke 1988 exchange and Perdew 1986 correlation functionals
CEPH	Ethyl 2-oxocyclopentanecarboxylate
CRL	Compound refractive lens
DFT	Density functional theory
EC	Electron capture
EFG	Electric field gradient
EPR	Electron paramagnetic resonance
ESRF	European synchrotron radiation facility
FC	Force constant
$Fe(acac)_3$	Ferric acetylacetonate
$Fe(ClO_4)_3$	Iron(III)perchlorate
$Fe(NO_3)_3$	Anhydrous iron nitrate
$FeCl_3 \cdot 6H_2O$	Ferric chloride hexahydrate
FIR	Far infrared
FWHM	Full width at half maximum
HRM	High-resolution monochromator
HS	High-spin

IC	Ionization chamber
ID18	Beamline: Insertion Device-18 of ESRF
LINAC	Linear accelerator
LS	Low-spin
MCA	Multichannel analyzer
MCS	Multichannel scaling
NIS	Nuclear inelastic scattering*
PC	Personal computer
ph	Photons
PHS	Pulse height spectrum
Rh	Rhodium
rmsd	Root mean square displacement
RT	Room temperature
SCA	Single channel analyzer
SDD	Stuttgart/Dresden pseudopotential
UHF	Spin unrestricted Hartree-Fock
UV/vis	Ultra violet/visible
VDOS	Vibrational density of (phonon) states, $g(E)$
XAS	X-ray absorption spectroscopy
XRD	X-ray diffraction

---

*At present there is no unique acronym for this synchrotron-based nuclear resonance technique, the other names, which are often used are nuclear inelastic absorption (NIA), nuclear resonance inelastic X-ray scattering (NRIXS), nuclear resonance vibrational spectroscopy (NRVS) and phonon-assisted Mössbauer effect

Contents

Abstract v

List of symbols and abbreviations vii

1 Introduction 1

1.1 Aim of the work . . . 1
1.2 Thesis outline . . . 3

2 Basics of Mössbauer spectroscopy 5

2.1 Introduction . . . 5
2.2 The Mössbauer effect . . . 5
2.3 Recoil energy loss . . . 6
2.4 Mössbauer spectral parameters . . . 8
  2.4.1 The Mössbauer line width and line shape . . . 8
  2.4.2 Recoil-free factor . . . 10
  2.4.3 Isomer shift . . . 14
  2.4.4 Electric quadrupole splitting . . . 16
  2.4.5 Magnetic dipole splitting . . . 18

3 Instrumentation of the Mössbauer spectrometer 19

3.1 Introduction . . . 19
3.2 Components of spectrometer . . . 19
  3.2.1 Source . . . 20
  3.2.2 Mössbauer drive . . . 20
  3.2.3 Collimator . . . 21
  3.2.4 Counting system and count rate . . . 22
3.3 Safety aspects . . . 24

3.4 Spectrometer geometry and source properties 25
3.5 Calibration and fitting 26
3.6 Notes 28

4 Nuclear inelastic scattering (NIS) 31
4.1 Introduction 31
4.2 Basics of synchrotron radiation 32
4.3 Instrumentation and measurement 34
4.4 Sample environment and holder 37
4.5 Basic features of NIS 39
4.6 Data evaluation 39

5 Reaction intermediates in the $FeCl_3$-catalyzed Michael reaction 45
5.1 Introduction 45
5.2 $FeCl_3$-catalyzed Michael reaction 46
5.3 Materials used and preparation 48
5.4 Normal mode analysis 48
5.5 Results and discussion 49
5.6 Conclusions 55

6 Gif reaction of a Fe complex as studied by Mössbauer spectroscopy 57
6.1 Introduction 57
6.2 The Gif reaction 58
6.3 Sample preparation and holder 59
6.4 Results and discussion 61
  6.4.1 Trinuclear iron catalyst 61
  6.4.2 Frozen solutions 62
6.5 Conclusions 71

7 Gif reaction of a Fe complex as studied by NIS and DFT 73
7.1 Introduction 73
7.2 Sample preparation 73
7.3 Measurement details 74
7.4 DFT and normal mode analysis 74
7.5 Force constant analysis 75

7.6 Results and discussion 76
7.6.1 Core of the trinuclear structure 76
7.6.2 Normal mode and force constant analysis of monomer 1 83
7.6.3 Normal mode and force constant analysis of monomer 2 88
7.7 Conclusions 93

8 Vibrational dynamics of a trinuclear Fe catalyst 95
8.1 Introduction 95
8.2 Sample preparation 96
8.3 Experiment and normal mode analysis 96
8.4 Results and discussion 97
8.4.1 NIS and DFT analysis 97
8.4.2 Raman analysis 105
8.5 Conclusions 106

9 Summary and outlook 107

10 Zusammenfassung und Ausblick 111

Appendix A ^{57}Fe Mössbauer constants 117

Appendix B Normal modes of D_{3h} and D_{4h} symmetries 119

List of Figures 125

List of Tables 131

Bibliography 133

Acknowledgments 143

Curriculum vitae 147

Chapter 1

Introduction

1.1 Aim of the work

The selective oxidation of organic molecules finds many applications in chemical industry and is important to life. Some of the widely known functions of selective oxidation are the reaction of heme-based metalloenzymes like cytochromes P450 and nonheme-based enzymes like methane monooxygenase. In these two selective oxidation reactions, the active metal center is iron. The reaction pathways of the metalloenzymes (many enzymes contain transition metals for their catalytic activity) are mainly determined by the electronic and geometrical structure of the transition metal ion and by the influence of the surrounding ligands [1]. Oxygen activation, which is e.g., responsible for the conversion of methane to methanol, occurs via iron intermediate species in methane monooxygenase. Moreover, the most extensively studied oxygen-activating enzymes are the cytochromes P450.

Despite their importance in biological functions, the mechanistic insights into the reaction pathways of selective oxidation is mostly lacking. The understanding of the operating modes of nonheme enzymes and their reactive intermediates, which are relevant to oxygen activation and carbon-hydrogen bond cleavage, is currently a major challenge because this knowledge is a prerequisite for biomimetic oxidations of hydrocarbons employing dioxygen [2].

This dissertation is focussed on the structure and dynamics of possible reactive intermediates formed in the Gif oxidation of a trinuclear iron complex. This (trinuclear iron) complex could be a model for ferritin mineralization, and recently the first crystal structure of a protein carboxylate coordinated oxobridged trinuclear iron cluster have been reported [3]. Traditional Raman and infrared spectroscopies can provide much insight into the reaction mechanisms, but their experimental data are limited due to the selection rules and low absorption intensities. Since the intermediates contain a reactive metal center, iron, a site-selective spectroscopy is in high demand. Nuclear inelastic scattering (NIS) is such a site-selective spectroscopic technique, which monitors only the vibrational displacement of iron and reveals the vibrational spectrum of the iron atom with all modes involving nonzero iron vibrational displacement. NIS takes advantages of high brilliance and pulsed structure of third-generation synchrotron radiation sources. In particular the low-energy spectral regions, where the metal-oxide vibrations occur, can be analyzed by NIS, in the light of computational predictions based on density functional theory (DFT). The spin and oxidation state of iron, which are necessary for quantum mechanical computations based on DFT, can be determined by ^{57}Fe transmission Mössbauer spectroscopy. Since NIS has never been applied to homogeneous catalytic reactions to reveal the structure of the catalytic intermediates, before applying NIS to the Gif reaction investigated within the cooperation of SFB706 on oxidation reaction, we first carried out a case study on the well-known Michael reaction.

NIS has been applied to study the vibrational dynamics of iron in heme proteins, all of which contain a porphyrin structure and nonheme proteins most of which consist of iron-sulphur clusters. There are a few results reported on NIS on nonheme and sulphur-free iron clusters with two, three or more iron sites [4]. Moreover, the iron storage protein (ferritin) may contain up to 4500 Fe(III) atoms, indicating that polynuclear iron proteins may exist in nature [5]. Recently, the crystal structure of such iron proteins have been reported [3]. In chapter 8, one such iron protein, which bears some structural similarity as in [3] is presented. The vibrational dynamics is analyzed by means of NIS and DFT calculations.

Keeping the above objectives in mind, the aim of the present work is to study the intermediates formed in the Gif-type oxidation reaction of trinuclear oxobridged iron complexes. For this purpose the experimental techniques used are Mössbauer spectroscopy and NIS. Quantum mechanical calculations based on DFT are also used to support the NIS data. In addition, a quantitative description of the vibrational dynamics of another trinuclear oxobridged iron complex is described in detail using the aforementioned three methods together with Raman spectroscopy are also presented. The instrumentation of a Mössbauer spectrometer is also discussed.

1.2 Thesis outline

Chapter 2 covers the fundamental theory of Mössbauer spectroscopy. The theory relevant for the present work is discussed in detail. The important Mössbauer spectral parameters, isomer shift and electric quadrupole splitting, are explained and illustrated.

Chapter 3 provides the instrumental aspects of a room temperature Mössbauer spectrometer built in the frame of this dissertation. This chapter also provides the details of the safety measures to avoid radiation exposure during sample mounting/changing. In addition, overviews of calibration of Mössbauer spectra, fitting procedures and counting system are briefly discussed. An emphasis on the theoretical and experimental count rate is discussed as a separate section.

Chapter 4 introduces the synchrotron-based technique NIS. Both the physics and the instrumental aspects are briefly discussed. The theory of the extraction of the vibrational density of phonon states (VDOS) from NIS data is shown. Some historical information together with relevant basic information of the synchrotron radiation, is given. Designs of the sample holders, which were used for measuring the NIS spectra, are also provided.

Chapter 5 describes the first study of the applicability of NIS to the well-known Michael reaction, by using NIS and DFT calculations. The intermediate formed in the Michael reaction, when the iron catalyst $FeCl_3 \cdot 6H_2O$ is dissolved in ethyl 2-oxocyclopentanecarboxylate, is predicted using NIS and DFT. This chapter serves as a basis for studying the new Gif reaction in chapter 6.

In chapter 6 the Gif reaction is studied using transmission Mössbauer spectroscopy. With the exception of the solid iron catalyst, all other (solution) samples are shock-frozen in liquid nitrogen and measured at 4.2 K. The Gif reaction is initiated by molecular oxygen in the presence of a trinuclear oxobridged iron compound. Mössbauer spectra of frozen solutions were obtained after stepwise addition of Gif reagents. This helps to monitor the oxidation and spin state of iron.

Chapter 7 is dedicated to NIS on the frozen solutions studied in chapter 6. Based on results obtained from Mössbauer spectroscopy, several model molecular structures were generated and optimized using the DFT method. Normal mode analysis was performed on the DFT optimized structures so as to simulate the VDOS of ^{57}Fe. The theoretically generated VDOS is compared with the experimental VDOS to analyze the molecular structures of the intermediates formed during the Gif reaction.

In chapter 8 a complete study of novel iron vibrational dynamics of a trinuclear iron compound is presented. The inequivalence of the iron sites was determined by Mössbauer spectroscopy. The VDOS of the trinuclear compound was obtained from NIS and the assignment of vibrational peaks was done using DFT calculations.

Finally chapter 9 presents the summary and conclusions produced from the analysis of the samples studied in this thesis.

Chapter 2

Basics of Mössbauer spectroscopy

2.1 Introduction

Mössbauer spectroscopy, also known as nuclear gamma resonance fluorescence spectroscopy, is a technique that probes transitions between the ground and low-lying excited states of the nucleus. The nucleus most favourite and amenable to Mössbauer spectroscopy is ^{57}Fe and hence iron containing compounds are widely investigated. Because of sharp nuclear transitions, the Mössbauer effect provides an extremely high energy resolution in the range of neV (with the γ-ray energy in the keV range) and, hence, it can be used to probe the chemical environment of a nucleus via its hyperfine interactions with the surrounding electron distribution. The atoms surrounding a Mössbauer nucleus influence the local electronic field around this nucleus and therefore, one can characterize the type of bonding. The Mössbauer technique is widely used in many branches of science including solid-state physics, chemistry, biophysics, materials science, geology, biology and mineralogy. Recently, miniaturized Mössbauer spectrometers were sent to the planet Mars for the exploration of the surface of the planet to access past climate conditions and their suitability for life [6].

2.2 The Mössbauer effect

The Mössbauer effect is the recoil-free emission and absorption of a γ-quantum in a transition between the ground state and an excited state of certain nuclei bound in a solid. It can be well described in terms of quantum mechanical phenomena. A source nucleus in an excited state of energy E_e undergoes a transition to the ground state E_g by emitting a γ-quantum of energy $E_0 = E_\mathrm{e} - E_\mathrm{g}$. This γ-quantum may be resonantly absorbed by another nucleus of the same isotope, which then undergoes a transition from its ground state to its excited state. After the resonant absorption of the γ-quantum, the absorbing nucleus stays in the excited state for the mean lifetime τ (=141.8 ns for ^{57}Fe). The subsequent deexcitation to its ground state either results in emission of either a conversion electron due to internal conversion (energy transfer from nucleus to the innermost electron shell) or a γ-quantum (nuclear resonance fluorescence). So in Mössbauer spectroscopy both a source (γ-emitter) and an absorber (the material under investigation) are needed. This phenomenon was discovered by Rudolf Ludwig Mößbauer in 1957, for which he received the Nobel prize in physics in 1961 [7].

2.3 Recoil energy loss

When the nucleus emits or absorbs a γ-quantum, a momentum transfer takes place between γ-quantum and nucleus. According to conservation of energy, when a nucleus at rest with an energy E_0 emits a γ-quantum of energy E_γ, it should experience a recoil energy loss E_R, and the recoil gives the nucleus a momentum in the opposite direction of the γ-quantum. Thus the available energy for emission of a γ-quantum is reduced according to the relation $E_\gamma = E_0 - E_\mathrm{R}$. Because of the large mass M of the nucleus bound in a solid and very small recoil compared to the transition energy E_γ, the situation can be treated in a nonrelativistic approximation. The kinetic energy or the recoil imparted to the nucleus is given by:

$$E_\mathrm{R} = M v_\mathrm{R}^2/2 = p_\mathrm{n}^2/(2M) \tag{2.1}$$

and the magnitude of the momentum of the γ-quantum is given by:

$$p = E_\gamma/c = \hbar k, \tag{2.2}$$

where v_R and c are the velocity of recoil and speed of light in vacuum, respectively, $\hbar = h/(2\pi)$, h is the Planck's constant and k is the magnitude of the wave vector of the γ-ray. According to conservation of momentum, the momentum of the γ-quantum and momentum p_n gained by the recoiling nucleus are equal in magnitude and opposite in sign, i.e. $\mid p_\mathrm{n} \mid = \mid p \mid$. Substituting eq. (2.2) in (2.1) we get:

$$E_\mathrm{R} = p_\mathrm{n}^2/(2M) = E_\gamma^2/(2Mc^2) = (\hbar k)^2/(2M). \tag{2.3}$$

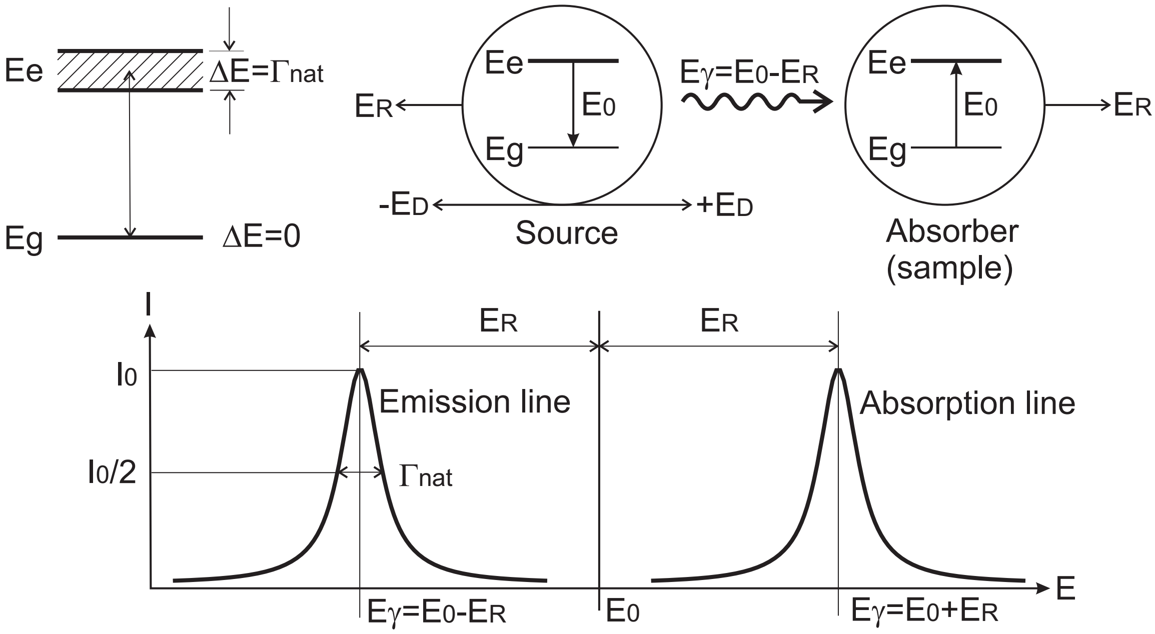

Figure 2.1: Schematic representation of the nuclear resonance transition between excited E_e and ground E_g states in two isolated nuclei. The ground state has $\Delta E = 0$ and the full width at half maximum of the spectral transition line is Γ_nat. The two Lorentzian lines (emission and absorption) are separated by $2E_\mathrm{R} \approx 10^6\Gamma_\mathrm{nat}$.

It should be noted that the nucleus that absorbs the γ-quantum will gain E_R, i.e. $E_\gamma = E_0 + E_\mathrm{R}$. As a result, the transition lines for emission and absorption are separated by a distance of $2E_\mathrm{R}$ (refer to fig. 2.1), which is about six orders of magnitude larger than the natural line width Γ_nat under consideration (for ^{57}Fe, $\Gamma_\mathrm{nat} = 4.641$ neV and $E_\mathrm{R} = 1.958$ meV). So resonance is not possible in isolated atoms or molecules in the liquid or gaseous state. For observing the Mössbauer effect the emission and absorption bands should overlap sufficiently. Although the recoil energy loss is relatively small with respect to the transition energy, one has to compensate it properly. This can be done by applying the linear Doppler effect to the γ-quantum to tune its energy, i.e. by moving the emitter nucleus in a well controlled manner. Thus the energy of the γ-quantum emitted from a nucleus moving with a velocity v along the direction of the γ-ray propagation can be shifted to E_D by a first-order linear Doppler effect according to:

$$E_\mathrm{D} = vE_\gamma/c. \tag{2.4}$$

The net energy emitted by the nucleus is now given by $E_\gamma = E_0 - E_\mathrm{R} + E_\mathrm{D}$ (for an absorbing nucleus $E_\gamma = E_0 + E_\mathrm{R} - E_\mathrm{D}$). From eq. (2.4), we see that for a nucleus moving with a v of 1 mm s^{-1} one has a shift of 48.08 neV. Typically for iron compounds a velocity of about ±11 mm s^{-1} is sufficient to obtain a complete Mössbauer spectrum. The Doppler shifting is achieved by mounting the emitter, i.e. the radioactive source ^{57}Co, onto a transducer (see fig. 3.1), the velocity of which can be precisely controlled by electronics.

2.4 Mössbauer spectral parameters

Electromagnetic waves interact with the nuclei in atoms by various processes that can follow resonant absorption of γ-quanta. The various backscattering processes and the decay scheme of ^{57}Co are shown in fig. 2.2. In transmission Mössbauer spectroscopy, one counts the γ-quanta transmitted through the absorber versus the Doppler-shifted energy (in velocity units, mm s^{-1}). The recorded spectrum is characterized by line shapes, positions, intensities and widths. The most important Mössbauer spectral parameters are the isomer shift, electric quadrupole splitting and magnetic dipole splitting. They arise from the hyperfine interactions between the nucleus and its surrounding electric and/or magnetic field. As a consequence there will be a small perturbation in the nuclear energy levels. These hyperfine interactions are very small compared to the energy levels of the nucleus itself. The other important parameters are line width, Lamb-Mössbauer factor and relativistic effects (second-order Doppler shift).

2.4.1 The Mössbauer line width and line shape

The time behaviour of the deexcitation of the nucleus follows an exponential function. Therefore, the shape of the line in the energy domain is a Lorentzian. The excited state of a nucleus with some mean lifetime spreads over a certain energy range ΔE (excited state of a nucleus cannot be assigned a sharp energy), which can be related to the uncertainty in time Δt via the Heisenberg uncertainty principle as:

$$\Delta E \, \Delta t \geq \hbar \tag{2.5}$$

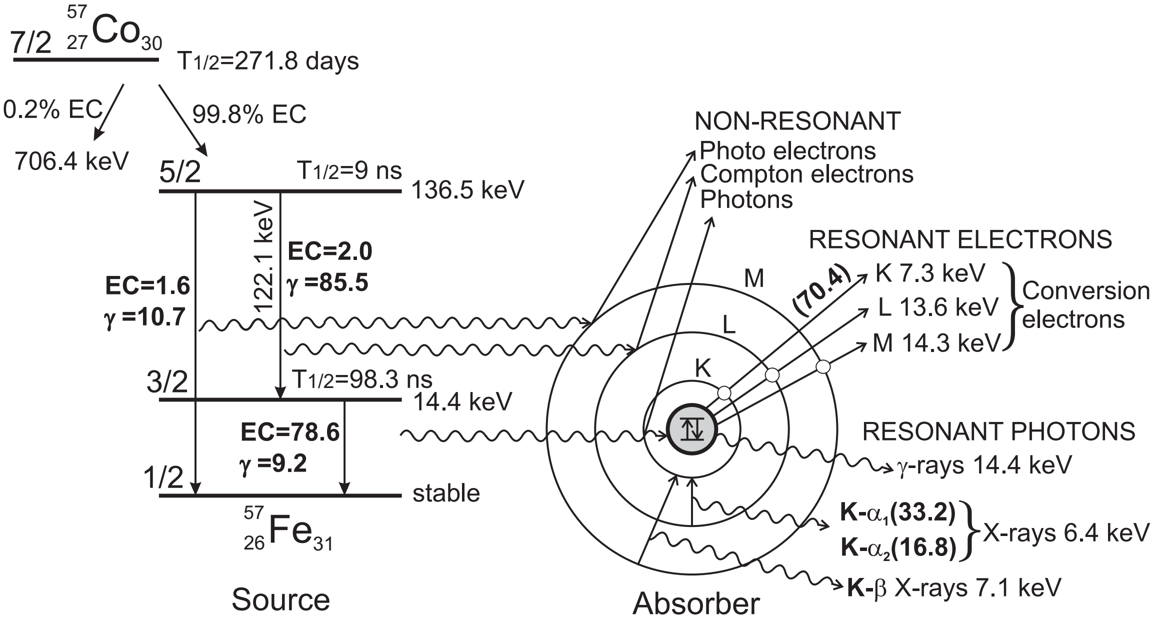
7/2 $^{57}_{27}$Co$_{30}$
T1/2=271.8 days
0.2% EC
706.4 keV
99.8% EC
5/2
T1/2=9 ns
136.5 keV
122.1 keV
EC=2.0
γ =85.5
EC=1.6
γ =10.7
3/2
T1/2=98.3 ns
14.4 keV
EC=78.6
γ =9.2
1/2
stable
$^{57}_{26}$Fe$_{31}$
Source
NON-RESONANT
Photo electrons
Compton electrons
Photons
RESONANT ELECTRONS
(70.4)
K 7.3 keV
L 13.6 keV
M 14.3 keV
Conversion electrons
M
L
K
RESONANT PHOTONS
γ-rays 14.4 keV
K-α1(33.2)
K-α2(16.8)
X-rays 6.4 keV
K-β X-rays 7.1 keV
Absorber

Figure 2.2: The nuclear decay scheme for $^{57}_{27}$Co–$^{57}_{26}$Fe and various backscattering processes that can follow resonant absorption of an incident γ-photon, modified from [8]. Approximately 12.3% (=(10.7+1.6)/99.8, γ and EC are the gamma and electron capture emission probabilities, respectively, per 100 disintegrations) of the deexcitations from the 136.5 keV state that occurs directly to the ground state. The remaining 87.7% (=(85.5+2.0)/99.8) decay occurs via the 14.4 keV level to the ground state. Of the 14.4 keV transitions, only 10.5% (=9.2/(9.2+78.6)) result in emission of a γ-ray, whereas the remaining 89.5% result in transfer of the transition energy to an atomic electron causing conversion electron emission, which leads to K-α_1 and K-α_2 X-ray emission. Values of EC and γ are taken from [9].

and the ground state is stable or has an infinite lifetime and so the uncertainty in energy is zero as shown in fig. 2.1 (top left). By applying the uncertainty principle (eq. (2.5)) to Mössbauer transitions, the relation between the line width Γ_{nat} and mean lifetime τ is [10]:

$$\Gamma_{\text{nat}}\,\tau \geq \hbar. \tag{2.6}$$

From eq. (2.6) we see that the mean lifetime is inversely proportional to the line width. Typically, the suitable lifetime for Mössbauer spectroscopy ranges from $\sim 10^{-6}$ s to ~10^{-11} s. Too short lifetimes (less than 10^{-11} s) produce broad emission and absorption transition lines, which are difficult to distinguish from the baseline of the spectrum, overlap between the lines is smeared out and hence the hyperfine structure may not be resolved. Longer lifetimes (greater than 10^{-6} s) produce narrow transition lines, which would not overlap sufficiently (extremely small Doppler velocity is required, but practically difficult). For ^{57}Fe, the mean lifetime is 141.8 ns, which is well suited for Mössbauer effect applications. The Mössbauer transmission spectrum is a record of transmitted γ-ray counts through the absorber/sample as a function of energy expressed as the Doppler shifted velocity or drive velocity v. Ideally, the line width Γ is equal to the sum of the natural line widths of the Mössbauer nuclei in the source and absorber (0.193 mm s^{-1} or 9.283 neV). The maximum resonance absorption occurs when the emission and absorption transition lines overlap completely. In other words, both transition lines should have the same energy. The cross section of resonance absorption of γ-rays as a function of energy E is given by [7]:

$$\sigma = \sigma_0 \frac{\Gamma^2}{4(E - E_0) + \Gamma^2}, \tag{2.7}$$

where the maximum absorption cross section σ_0 is given by [7]:

$$\sigma_o = \frac{\lambda^2}{2\pi} \cdot \frac{2I_\mathrm{e} + 1}{2I_\mathrm{g} + 1} \cdot \frac{1}{\alpha + 1}, \tag{2.8}$$

where I_e and I_g are the nuclear spins of excited and ground state, respectively, λ is the wavelength of the γ-ray and α is the total internal conversion coefficient, which is the ratio of the number of deexcitations via electron emission (no change in atomic number) and the number of deexcitations via γ-quantum emission. For ^{57}Fe, σ_0 and α are 2.56×10^{-22} m^2 and ~8.2, respectively.

2.4.2 Recoil-free factor

The Mössbauer effect in isolated atoms, molecules in liquids or gases is negligible due to large recoil (see section 2.3). In solids, the recoil energy consists of two different parts:

$$E_\mathrm{R} = E_\mathrm{trans} + E_\mathrm{vib}. \tag{2.9}$$

In solids the Mössbauer nucleus is almost rigidly fixed to the lattice so that $\mathrm{E}_\mathrm{trans}$ is negligible. The second term, E_vib in eq. (2.9), is the average lattice (phonon) vibrational energy that is transferred to the lattice. From quantum mechanics, it is known that the spacing between two successive populations of the vibrational energy levels is given by $h\nu$ or $\hbar\omega$ and the average energy in the n^{th} state (or in the phonon picture: number of phonons in a mode associated with frequency ν) for a single harmonic oscillator is given by:

$$E = h\nu\left(\frac{1}{2}+n\right) = \hbar\omega\left(\frac{1}{2}+n\right) \tag{2.10}$$

and from Bose-Einstein statistics, the averaged phonon occupation number or the expected number of phonons with energy $h\nu$ ($=\hbar\omega$) at a temperature T is given by:

$$\langle n\rangle = \frac{1}{\exp\left(\frac{h\nu}{k_{\mathrm{B}}T}\right)-1}, \tag{2.11}$$

where k_{B} is the Boltzmann constant. If E or E_{R} (i.e. E_{vib}) is larger than a vibrational energy quantum, the energy is usually transferred in the form of heat to the surroundings. The recoil energy of all Mössbauer nuclei known to date falls in the range $\sim 10^{-4}$ – $\sim 10^{-1}$ eV, which is in the order of $h\nu$ (atomic vibrations frequencies ν are in the order of 10^{12} – 10^{13} Hz). Therefore, there is a chance that $h\nu$ is greater than E_{R}. Thus, there should be a certain probability f that no energy transfer, i.e. no lattice excitation of phonons takes place during emission or absorption of quanta. This is called a zero-phonon transition. The recoil energy in terms of the fraction f—the number of recoil-free γ-quanta events (emission or absorption) relative to total number of γ-quanta events—is given by the following relation:

$$E_{\mathrm{R}} = (1-f)h\nu = (1-f)\hbar\omega. \tag{2.12}$$

In eq. (2.12), $(1-f)$ is the fraction for the creation of one phonon of energy $h\nu$ (one-phonon transition).

For a harmonic oscillator, the mean potential energy E_{pot} is equal to half of the total energy E, therefore we can write:

$$E = E_{\mathrm{kin}} + E_{\mathrm{pot}} = \frac{M\overline{v^2}}{2} + \frac{M\omega^2\langle x^2\rangle}{2} = M\omega^2\langle x^2\rangle \Longrightarrow \langle x^2\rangle = \frac{E}{M\omega^2}, \tag{2.13}$$

where $\langle x^2\rangle$ is the mean square vibrational amplitude in the x direction and $\overline{v^2}$ is the mean square velocity of the nucleus. Substituting eq. (2.10) in (2.13) by taking $n=0$ (zero-phonon transition) and using eq. (2.3), from (2.12) we obtain:

$$f = 1 - \frac{E_{\mathrm{R}}}{\hbar\omega} = 1-(k^2\langle x^2\rangle); \tag{2.14}$$

or in the most general form (taking also two-phonon and higher processes into account):

$$f = \exp(-k^2\langle x^2\rangle). \tag{2.15}$$

The Einstein model, which is often a good approximation for molecular vibrations, where all atoms vibrate with the single frequency ω, $\langle x^2\rangle$ can be derived by sustituting eq. (2.10) in (2.13) and using (2.11). Thus,

$$\langle x^2\rangle = \frac{\hbar}{M\omega}\left(\frac{1}{2} + \frac{1}{\exp\left(\frac{\hbar\omega}{k_\mathrm{B}T}\right) - 1}\right). \tag{2.16}$$

A more realistic picture, in particular for solids, is given by the Debye model, where different frequencies are assigned to different oscillators. The number of vibrational (phonon) states per energy—the distribution of energy levels of the phonons $g(\omega)$—is proportional to the square of the frequency, i.e.

$$g(\omega) \propto \omega^2 \Longrightarrow g(\omega) = \text{constant} \times \omega^2. \tag{2.17}$$

The phonon distribution function $g(\omega)$ has the following normalization (and using eq. (2.17)):

$$\int_0^{\omega_\mathrm{D}} g(\omega)\,\mathrm{d}\omega = 3N \Longrightarrow g(\omega) = 9N\omega^2/\omega_\mathrm{D}^3, \tag{2.18}$$

where N is the number of atoms. ω extends to a maximum allowed frequency, called Debye frequency ω_D. A temperature θ_D (Debye temperature) can be assigned to the Debye frequency according to:

$$\hbar\omega_\mathrm{D} = k_\mathrm{B}\theta_\mathrm{D}. \tag{2.19}$$

Thus for the Debye model we have,

$$\langle x^2\rangle = \frac{1}{3N}\int_0^{\omega_\mathrm{D}} \langle x^2\rangle g(\omega)\,\mathrm{d}\omega. \tag{2.20}$$

Substituting eq. (2.16) in (2.20) and using eqs. (2.18), (2.19) and (2.3), we obtain for f from (2.15) as:

$$f = \exp\left\{-\frac{3E_\mathrm{R}}{2k_\mathrm{B}\theta_\mathrm{D}}\left[1 + 4\left(\frac{T}{\theta_\mathrm{D}}\right)^2 \int_0^{\theta_\mathrm{D}/T} \frac{x}{e^x - 1}\,\mathrm{d}x\right]\right\}, \tag{2.21}$$

where $x = h\nu/(k_\mathrm{B}T)$ and the integral is known as the Debye integral. The expression (2.21) is mainly dependent on the temperature and so can be classified for three different temperature limits as follows:

For low temperatures $T \ll \theta_{\mathrm{D}}$, the integral in the above relation (2.21) becomes $\pi^2/6$ hence,

$$f = \exp\left\{-\frac{E_{\mathrm{R}}}{k_{\mathrm{B}}\theta_{\mathrm{D}}}\left[\frac{3}{2}+\left(\frac{T\pi}{\theta_{\mathrm{D}}}\right)^2\right]\right\}. \tag{2.22}$$

From the above relation (2.22), it is clear that $\ln f$ or $\langle x^2\rangle$ is proportional to T^2.

When $T \gg \theta_{\mathrm{D}}$, the integral in (2.21) becomes θ_{D}/T so $\langle x^2\rangle$ or $\ln f$ is linear in T:

$$\ln f = -\frac{6E_{\mathrm{R}}T}{k_{\mathrm{B}}\theta_{\mathrm{D}}^2}. \tag{2.23}$$

Classically, when $T = 0$ there should not be any oscillations, i.e. $\langle x^2\rangle = 0$ and eq. (2.15) implies $f = 1$. But due to zero-point energy at absolute temperature, f can take a highest possible value smaller than one. Therefore at low temperatures f depends only on the ratio $E_{\mathrm{R}}/\theta_{\mathrm{D}}$, taking $T = 0$ in eq. (2.21) we obtain:

$$f = \exp\left(-\frac{3E_{\mathrm{R}}}{2k_{\mathrm{B}}\theta_{\mathrm{D}}}\right). \tag{2.24}$$

Even at absolute zero, we find some vibrations, which are due to the fact that the lowest possible state of the quantum harmonic oscillator can never be zero and at least has an energy of $h\nu/2$. Thus, $\langle x^2\rangle$ is never zero and so $0 < f < 1$. Experimentally, the f fraction can be determined from the Mössbauer spectrum by making use of the transmission integral fit [11, 12]. In fact the Mössbauer spectrum is a convolution between the source emission spectrum and absorber transmission spectrum (both are Lorentzian functions). The transmission of γ-ray depends on the thickness of the absorber, therefore the transmission probability, i.e. area of the spectrum directly reflects the effect of thickness of the absorber. The effective absorber thickness t_{A} is given by [13]:

$$t_{\mathrm{A}} = f_{\mathrm{a}}\,\sigma_0\,N_{\mathrm{A}}\,\beta_{\mathrm{iso}}\,\rho\,\Delta x/M_{\mathrm{m}}, \tag{2.25}$$

with f_{a} being the Mössbauer factor of the absorber. N_{A} is Avogadro's constant, β_{iso} the relative isotopic abundance of ^{57}Fe in the absorber (0.02 for unenriched samples), ρ and Δx are the mass density and geometric thickness of the absorber, respectively, and M_{m} is the molar mass of the Mössbauer isotope. The above eq. (2.25) can be included in the absorber transmission function of the fitting routine based on the transmission integral fit to obtain the factor t_{A}. To make use of the transmission integral fit, one needs to know the f factor and line width for the source, which is usually given by the manufacturers (for details see [14]).

For an accurate determination of f_a for the study of lattice dynamics, the nuclear inelastic scattering technique is the better choice (for details see chapter 4). From the above discussions we see that f (also known as Lamb-Mössbauer factor) is an important parameter in Mössbauer effect applications to study the lattice dynamics. For a specific isotope, it depends only on the temperature of the absorber and the mean square displacement of the Mössbauer nuclei in the absorber (see eq. (2.15)). The Lamb-Mössbauer factor is roughly equivalent to the Debye-Waller factor used in neutron scattering or X-ray diffraction studies, in which the factor provides the details on the fraction of elastic scattering.

2.4.3 Isomer shift

The electrostatic Coulomb interaction between the nuclear charge and the electrons shifts the energy level of the nucleus both in the excited and in the ground state. The nuclear charge is considered as a uniform and spherically symmetrical charge. The isomer shift (also known as centre shift or chemical isomer shift) is due to the fact that the s-electrons have the ability to penetrate the nucleus and to spend a fraction of time in the nuclear region. Therefore, the charge densities of the s-electrons, which are closest to the nucleus, are the main contributors to the isomer shift. In a Mössbauer experiment, one measures energy differences in an absorber and in a source and therefore we have four electrostatic shifts: the shifts of excited and ground state levels in both the source and the absorber as shown in fig. 2.3. In an actual experiment we measure the difference in the shifts of the excited and ground state energy levels between absorber and source. The general expression for isomer shift is given by [15]:

$$\delta = \mathrm{Const}\,\frac{\Delta R}{R}\left(\mid \Psi(0) \mid_\mathrm{A}^2 - \mid \Psi(0) \mid_\mathrm{S}^2\right), \tag{2.26}$$

where $\mathrm{Const} = 4\pi Z e^2 R^2/5$; Z and e are atomic number and proton charge, respectively. ΔR is the change in the radius of the Mössbauer nucleus going from the excited state to the ground state ($\Delta R = R_\mathrm{e} - R_\mathrm{g}$) and R is the mean radius of the Mössbauer nucleus in both states ($R = (R_\mathrm{e} + R_\mathrm{g})/2$). The term inside the parenthesis represents the difference in total electron densities at the nucleus of the source and absorber. For ^{57}Fe, ΔR is a negative quantity, i.e. the radius of the nucleus in the excited state is smaller than that in the ground state ($R_\mathrm{e} < R_\mathrm{g}$). Therefore, a decrease of the electron density at the nucleus of the absorber results in an increase of its isomer

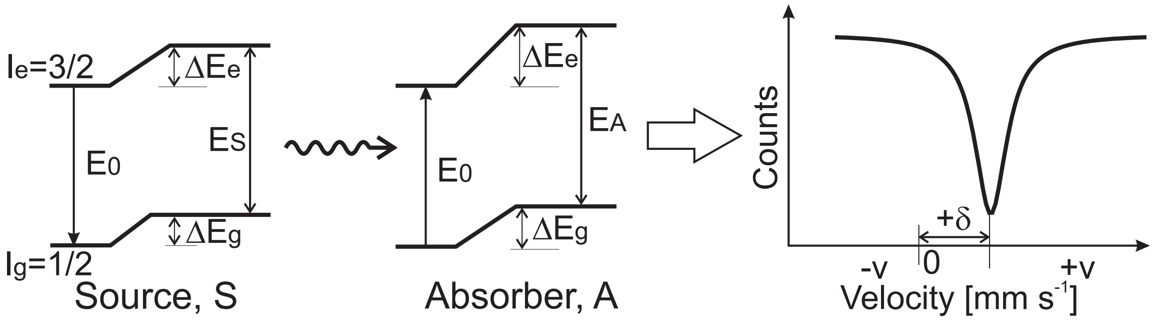

Figure 2.3: The nuclear levels are shifted without changing the degeneracy due to a finite electron density at the nucleus. Isomer shift δ is the difference in the shifts of nuclear levels of absorber and source, i.e. $\delta = (E_\mathrm{A} - E_\mathrm{S}) = (\Delta E_\mathrm{e} - \Delta E_\mathrm{g})_\mathrm{A} - (\Delta E_\mathrm{e} - \Delta E_\mathrm{g})_\mathrm{S}$. The schematic Mössbauer spectrum shown on the right displays a positive δ.

shift. A positive isomer shift means the electron density at the absorber nucleus is lower than that of the source nucleus, i.e. $\mid \Psi(0) \mid^2_\mathrm{A} < \mid \Psi(0) \mid^2_\mathrm{S}$.

Since Mössbauer spectroscopy is a relative technique, for a particular Mössbauer nuclide (in our case ^{57}Fe), observed changes of δ in the positive direction relative to the isomer shift of a reference absorber (usually α-Fe foil) indicate a decrease of the electron density at the absorber nucleus. Isomer shifts must always be reported with respect to a standard reference material and the temperature at which this material was measured. In a Mössbauer spectrum, this shift appears as the difference between the position of the center of mass of the resonance signal and zero Doppler velocity as shown in fig. 2.3. So far we have considered only the s-electron charge density at the nucleus, however it can be significantly influenced by the contribution from electrons from partially filled valence orbitals. From a chemical point of view, the valence electrons dominate the bonding with the surrounding ligands and define the oxidation and spin state of the Mössbauer nucleus. It has been known that an increase of the d-electron charge density will decrease the s-electron density at the nucleus and thus δ will be more positive (for ^{57}Fe). This is called screening or shielding effect. Therefore, the isomer shift gives valuable information about the oxidation state, spin state, and bonding properties. As an example, the isomer shift of Fe(II) compounds is usually more positive than that in Fe(III), since the extra electron in the d-shell present in Fe(II) decreases the s-electron density at its nucleus. The isomer shift is only weakly dependent on temperature, and a small dependency is generally due to the second-order Doppler effect [16].

2.4.4 Electric quadrupole splitting

The electric quadrupole interaction between the nuclear quadrupole moment Q and an inhomogeneous electric field or nonzero electric field gradient (EFG) from electrons around the nucleus leads to a splitting of the nuclear levels, i.e. it lifts all or part of their $(2I+1)$-fold degeneracy (I is the nuclear spin quantum number). This is called quadrupole splitting. The quadrupole splitting occurs only in nuclear states with spin $I > 1/2$ (see fig. 2.4), since nuclei whose spin is 0 or 1/2 have zero Q ($Q = I(2I-1)$). Therefore, the ground state of ^{57}Fe cannot exhibit quadrupole splitting, but has a two fold degeneracy (which can be lifted by magnetic dipole interactions, for details see section 3.5 of chapter 3). The nonsphericity can be described by the EFG tensor, which is a 3×3 tensor, the components of which are defined as the second derivatives of the electric potential V produced by extra-nuclear charges at the nuclear site $\left(\frac{\partial^2 V}{\partial x_i \partial x_j}\right)$. Unlike the nuclear charge distribution, the electronic charge distribution is generally not axially symmetric. However, it is possible to find a principal coordinate system, where the non-diagonal components of the EFG tensor V_{ij} vanish. A unique axis system of the Mössbauer atom, called the “ principal axes of the EFG tensor ”, can be defined such that the off-diagonal elements are ordered as $\mid V_{xx} \mid \leq \mid V_{yy} \mid \leq \mid V_{zz} \mid$. Moreover, as Laplace’s equation requires that the trace of V_{ij} be zero, i.e. $V_{xx} + V_{yy} + V_{zz} = 0$, only two components will be independent: V_{zz} and the asymmetry parameter $\eta = \mid (V_{xx} - V_{yy})/V_{zz} \mid$, thus η is restricted to $0 \leq \eta \leq 1$. The interaction between the electric quadrupole moment of the nucleus and the EFG at the nucleus can be described by the Hamiltonian [17]:

$$\mathcal{H}_{\mathrm{Q}} = \frac{eQV_{zz}}{4I(2I-1)} \left[3\hat{I}_z^2 - \hat{I}^2 + \eta(\hat{I}_x^2 - \hat{I}_y^2)\right], \tag{2.27}$$

where $\hat{I}$ is the nuclear spin operator and $\hat{I}_x$, $\hat{I}_y$ and $\hat{I}_z$ are the nuclear spin operators for components x, y and z, respectively. V_{zz} is the absolute value of the EFG in the z-direction at the site of the atomic nucleus. The eigenvalues of the Hamiltonian (2.27) can be written as:

$$E_{\mathrm{Q}} = \frac{eQV_{zz}}{4I(2I-1)} \left[3m_I^2 - I(I+1)\right] \left(1 + \frac{\eta^2}{3}\right)^{1/2}, \tag{2.28}$$

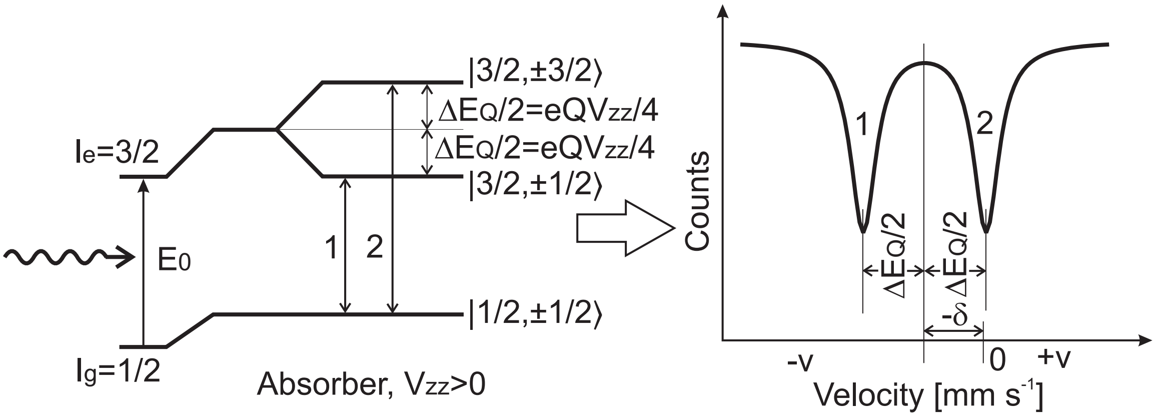

Figure 2.4: The nuclear excited state I_e is split into two substates $|3/2,\pm3/2\rangle$ and $|3/2,\pm1/2\rangle$ (magnitude of splitting is equal for both states) by quadrupole interaction energy. The schematic Mössbauer spectrum with two peaks corresponding to two substate transitions along with negative δ is shown on the right.

where $m_I = I, I-1, ..., -I$ is the nuclear magnetic spin quantum number. Q is a measure of the deviation of the nuclear charge from spherical symmetry and is a constant for a given Mössbauer nuclide. Therefore, changes in quadrupole interaction energy can only arise from changes of the EFG. The sign of Q can be positive or negative according to whether the nucleus is respectively elongated (prolate) or flattened (oblate) along the principal spin-axis. For the iron nucleus, the excited state $I = 3/2$ ($Q > 0$) is split in two doubly degenerate substates $|3/2,\pm3/2\rangle$ and $|3/2,\pm1/2\rangle$, without shifting the centre of gravity, see fig. 2.4. The ground state with spin 1/2 is unsplit. The difference in energy ΔE_Q between the two substates ($|3/2,\pm3/2\rangle$ and $|3/2,\pm1/2\rangle$) can be obtained from eq. (2.28) by taking $I = 3/2$:

$$\Delta E_\mathrm{Q} = E_\mathrm{Q}(m_I = \pm3/2) - E_\mathrm{Q}(m_I = \pm1/2) = \frac{eQV_{zz}}{2}\left(1+\frac{\eta^2}{3}\right)^{1/2}. \tag{2.29}$$

In a Mössbauer experiment using a single-line source one observes two resonance lines corresponding to the two nuclear transitions between the two substates and the ground state. The distance between the two resonance lines is equal to the energy ΔE_Q and the average of the two line positions is the isomer shift (see fig. 2.4). The sign of V_{zz} can be determined by applying an external weak magnetic field, typically less than 4 T (for details refer to [18]). V_{zz} is sensitive to the electron configuration of the valence shell, e.g., the Fe d-orbitals. The aspherical population of electrons in the d-orbitals due to the ligand field also influences V_{zz}. In high-spin (HS) Fe(III), each d-orbital contains one spin-up electron and $(V_{zz})_{\text{valence}} = 0$ because of symmetry. In HS Fe(II) there is one excess electron, which contributes significantly to the EFG, and for this reason the quadrupole splitting of HS Fe(II) ($\sim$3 mm s^{-1}) is large when compared to HS Fe(III) ($\sim$0.5 mm s^{-1}). For the low-spin states of Fe(II) and Fe(III), the former has a smaller ΔE_{Q} (less than 0.8 mm s^{-1}) while the latter has a larger ΔE_{Q} (0.7 to 1.7 mm s^{-1}), again reflecting the one electron difference in the d-orbital occupancy.

2.4.5 Magnetic dipole splitting

In all the results presented in this work no magnetic hyperfine structure is observed. The measurements were performed without external magnetic field. However, the calibration of the spectrometer is usually done by making use of the magnetic hyperfine splitting of the α-Fe foil. The procedure, together with the necessary theoretical background, is explained in section 3.5 of chapter 3.

Chapter 3

Instrumentation of the Mössbauer spectrometer

3.1 Introduction

In this chapter, the instrumentation adopted for the room-temperature (RT) Mössbauer spectrometer built in the frame of this dissertation will be briefly discussed. Details of calibration of the spectrometer, fitting procedure to the experimental spectra and information on count rates are also provided. The shielding and safety system that was used for the spectrometer to avoid the leakage of γ-rays is briefly discussed.

3.2 Components of spectrometer

A transmission Mössbauer spectrometer consists of the following four basic parts: source, Mössbauer drive, collimator and detector, as schematically shown in fig. 3.1. Mössbauer spectrometers are extremely sensitive to vibrations from external sources and therefore all basic components should be rigidly fixed to a heavy base. Moreover, relative motion between the four parts should be avoided completely. Due to the ionizing nature of γ-rays, an additional part, i.e. a safety shutter based on a servo mechanism that can be controlled externally to avoid radiation exposure during sample changing, becomes an integrated part of the spectrometer.

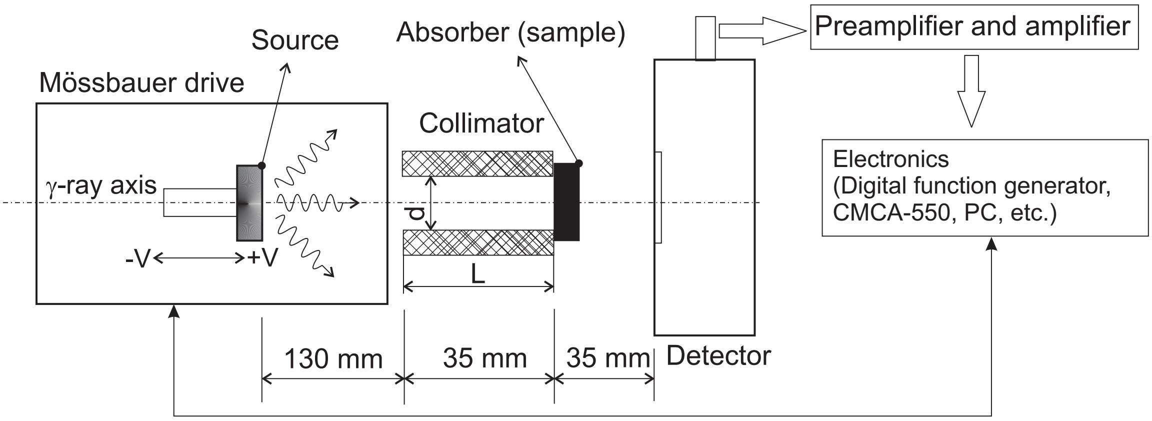
Source
Absorber (sample)
Preamplifier and amplifier
Mössbauer drive
Collimator
Electronics
(Digital function generator,
CMCA-550, PC, etc.)
γ-ray axis
d
-V
+V
L
130 mm
35 mm
35 mm
Detector

Figure 3.1: Schematic of a transmission Mössbauer spectrometer. The energy of the γ-ray is tuned by moving the source relative to the sample. The collimator $d/(2L)$ ratio is 0.07 (for other relevant information see section 3.4). Although the diameter ϕ of the detector window is 25 mm, only ϕ of 7.12 mm is visible to the source, therefore the effective radius of the detector window is $r_{\text{eff}} = 3.56$ mm.

3.2.1 Source

The source was ^{57}Co incorporated into a ~7 µm metal rhodium foil with an initial activity of 56.5 mCi. Other relevant properties are given in table 3.1. The source, whose surface is sealed/covered with a 40 µm aluminium foil, was purchased from Cyclotron Co., Ltd., Russia. Aluminium foils are important for two reasons, 1. to act as a filter to attenuate the 6.4 keV X-rays, which are more intense than 14.4 keV Mössbauer transition, thereby increasing the efficiency of the detector, and 2. to avoid the risk of radiation exposure.

3.2.2 Mössbauer drive

The radioactive source emits the 14.4 keV γ-rays as shown in fig. 2.2. The Mössbauer transition is monochromatic (energy is fixed) and in order to cover all the resonance lines that lie around 14.4 keV, the energy has to be tuned. Typically for iron compounds the resonance line(s) can be somewhere ±500 neV around the 14.4 keV transition. The modulation of the γ-rays can be achieved by fixing the source to a Mössbauer drive, which moves the source back and forth with respect to the sample, i.e. making use of the Doppler effect. The velocity of the Mössbauer drive is scanned from $-v$ to $+v$ and then goes back to $-v$, completing a backward scan, hence, in one scan period, a computer will record two spectra, which are mirror images of each other (+ means the source moving towards the sample). Therefore these two spectra should be added (before adding one of them is inverted in the channel scale) and the folding point, i.e. the point that separates the two spectra is determined by the least-squares method such that the relative shift between the spectra is minimum.

The Mössbauer drive is an electromechanical device similar to a loudspeaker system. It consists of rigidly connected driving and pickup coils moving in a homogeneous magnetic field. These two coils are connected in series with the reference signal. The current passing through the driving coil in a permanent magnet, which is attached to the Mössbauer drive, forms the driving force. A drive unit with an electronically controlled voltage (reference signal) is fed to the driving coil. The signal from the induced pickup coil feeds the information of the actual velocity back to the drive unit. The feedback system formed in this manner provides a motion with minimized deviation from its correct value. A switch is provided in the digital function generator for the selection of a reference signal, which can be either a triangular or a sine wave form of voltage, for source motion. The rest of the electronics is beyond the discussion of the present work. It is important that the source is screwed firmly to the mobile part of the drive, so as to eliminate velocity errors due to wobbling.

3.2.3 Collimator

Another important part is the collimator, which should be designed carefully to avoid cosine smearing, which causes line shifting and line broadening. Cosine smearing is due to the solid angle between source and detector. The recorded γ-rays may be emitted from the source under a finite angle relative to the direction of source velocity. This may also give rise to a nonsymmetrical line shape if the resonance is markedly shifted from zero velocity. To avoid all these problems, a lead circular block was used as a collimator. The collimator is designed according to the hole-to-length ratio as described in [19]. The ratio is as follows:

$$\frac{\text{radius of hole}}{\text{length of collimator}} \ll 1. \tag{3.1}$$

The length L and radius $d/2$ of the collimator is 35 mm and 2.5 mm, respectively (see fig. 3.1), which gives hole-to-length ratio of 2.5/35=0.07. Since the spectrometer was continuously relocated to different places, the Mössbauer drive is not screwed rigidly to the base so that the handling and transportation of the source is easier. But this will cause serious line broadening problems and in order to circumvent this issue a heavy collimator (lead block) of ~6.5 kg is used. The collimator was made by a casting process, i.e. melting lead in an electric oven and pouring it into a mould. For improving the strength and hardness, ~4% by weight of antimony powder was added during the melting. Finally the surface is cleaned by machining and a hole of diameter 5 mm for the γ-ray passage was drilled. The collimator reduces the line broadening by 44% on comparing the outer line widths of the spectrum obtained from an α-Fe foil (with 0.1 kg collimator: 0.36 mm s^{-1}, with 6.5 kg collimator: 0.25 mm s^{-1}).

3.2.4 Counting system and count rate

The gamma counting system consists of a gas proportional counter (filled with Xe-CO_2, maximum voltage: 3 kV), preamplifier, single channel analyzer (SCA), amplifier, discriminator and multichannel analyzer (MCA). All these components are commercially available. For the spectrometer built in the frame of this thesis, a special data acquisition module was used—CMCA-550, manufactured from Wissel GmbH, Germany. The CMCA-550 has the great advantage that it can work in multichannel scaling (MCS) mode, where the analog pulses from the output of the spectrometer/detector's amplifier are fed to the input of the CMCA-550 where pulses are converted to digital values, and finally the data are transferred to a personal computer (no need for an extra MCA card, only an appropriate software is needed). ^{57}Co emits (see fig. 2.2) γ-rays of 136.5, 122.1 and 14.4 keV and X-ray fluorescence of 6.4 keV. The emission of the 14.4 keV γ-ray only accounts for 10.5% of the quanta and the rest results in transmission of energy to atomic electrons, i.e. conversion electrons. Therefore, the gamma counter should be sensitive only to 14.4 keV γ-rays and of course the 6.4 keV peak should be discriminated by setting a window to select only the 14.4 keV signal. This is checked in the pulse height spectrum (by selecting the pulse-height mode). A typical pulse height spectrum (PHS) is shown in fig. 3.2. After selecting the 14.4 keV signal, the pulse-height mode is changed to the MCS mode for measuring samples. The measured spectrum is a record of counts versus velocity in terms of velocity points (channel numbers). In our case we set this to 1024, therefore the calibrated spectrum contains 512 channels or data points (see

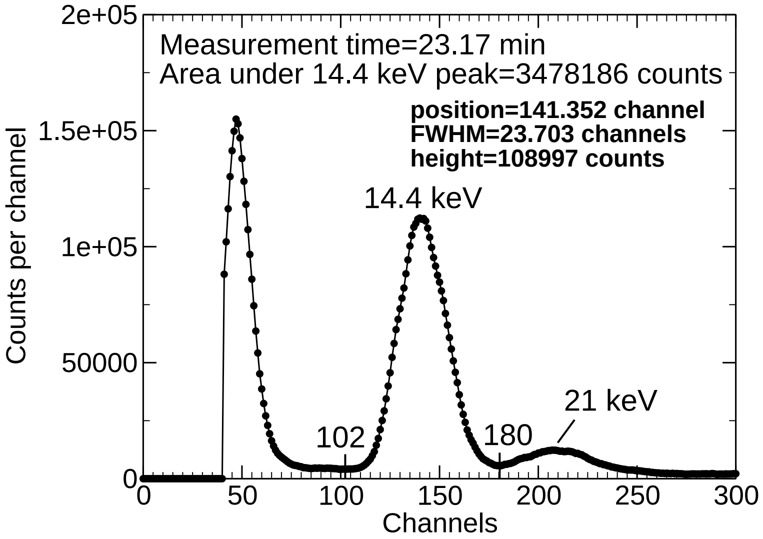

Figure 3.2: PHS of ^{57}Co source and the experimental count rate for the 14.4 keV peak is 2502 counts s^{-1} (=area/time). The peak's lower and upper limit which is indicated as vertical bars corresponds to 125–220 mV. The peak parameters in the plot are obtained by fitting the peak between 102 and 180 channel with a Gaussian function. The detector resolution for the peak is FWHM/position=16.8%. The broad peak corresponds to ~21 keV, which is the K-α X-ray emission from the source matrix, i.e. rhodium.

fig. 3.4). For the conversion of channels to velocity units, see section 3.5. Excluding the Mössbauer effect, the expected count rate for the 14.4 keV transition (9.2 per 100 disintegrations) when measured with a α-Fe foil can be calculated theoretically by [20]:

$$\text{Count rate} = S\,\frac{9.2}{100}\cdot\left(\exp\frac{-t\ln 2}{T_{1/2}}\right)\frac{\pi r_{\text{eff}}^2}{4\pi l^2}\exp\left(-\frac{\mu}{\rho}\,t_{\text{Fe}}\,\rho\right)\ \text{counts s}^{-1}, \tag{3.2}$$

where t is the number of days that passed from initial source strength of S (S in Bq). $T_{1/2}$(=271.8 days) is the half lifetime of ^{57}Co. r_{eff}(=3.56 mm) is the effective radius of the detector and l is the distance between source and detector. μ, ρ and t_{Fe} are the linear attenuation coefficient, density and thickness of iron, respectively. For the 14.4 keV γ-ray, iron has $\mu/\rho = 63.7$ cm^2 g^{-1} (taken from [21]).

The spectrum shown in figs. 3.2 and 3.4 was measured after 605 days from the date of purchase of the source. For the initial source strength and other geometrical parameters of the instrument configuration see table 3.1 and fig. 3.1. According to formula (3.2), taking $t = 605$ days and $t_{\mathrm{Fe}} = 25$ µm one obtains the count rate as 944 counts s^{-1}, which is slightly more than the count rate obtained from the spectrum shown in fig. 3.4. Alternatively, the experimental count rate of the Mössbauer transition in PHS can be checked by taking $t_{\mathrm{Fe}} = 0$ (in PHS no attenuation) in formula (3.2), which gives 3258 counts s^{-1}. This theoretical count rate is more than the experimental count rate of 2502 counts s^{-1} (from 14.4 keV peak) obtained from the PHS as shown in fig. 3.2. The reason for this deviation in count rate is that in the PHS shown in fig. 3.2, for the 14.4 keV peak, the count rate depends on the window size (left and right border of the peak), hence, a deviation of 756 counts $\mathrm{s}^{-1}(= 3258 - 2502)$ is not surprising. Therefore, a slight change in the window size might result in a considerable change in the PHS count rate. In addition, a slight change in the window size of the PHS does not affect the count rate of the MCS spectrum (or Mössbauer spectrum) significantly. Moreover, the formula (3.2) is typically valid for an isotropic point-like source. However, despite the above discussion the formula (3.2) can be used for a rough estimate of the count rate.

3.3 Safety aspects

The source with Mössbauer drive is completely shielded with serveral lead sheets each 3 mm thick to avoid radiation leakage to the outside. For a typical Mössbauer source some millimeters of lead are sufficient to decrease the radiation exposure by a factor of about 100 (for a detailed analysis of handling of source and exposure rate calculations, see [22]). The thickness of lead t_{Pb} needed to shield can be calculated from the Lambert law as follows:

$$S(t_{\mathrm{Pb}}) = S \exp\left(-\frac{\mu}{\rho}\, t_{\mathrm{Pb}}\, \rho\right), \tag{3.3}$$

where S is the initial activity of the source and $S(t_{\mathrm{Pb}})$ is activity observed outside the shielding. μ and ρ are the linear attenuation coefficient and density of lead, respectively. For the high probability emission, i.e. the 122.1 keV γ-ray, lead has $\mu/\rho = 3.21$ cm^2 g^{-1} (taken from [21]). Taking $S(t_{\mathrm{Pb}})$ and S as 1 and $2.09{\times}10^9$ Bq, repectively, one obtains t_{Pb} as 5.9 mm, which is needed to shield the radiation. In order to avoid radiation exposure during sample change, a safety shutter was made

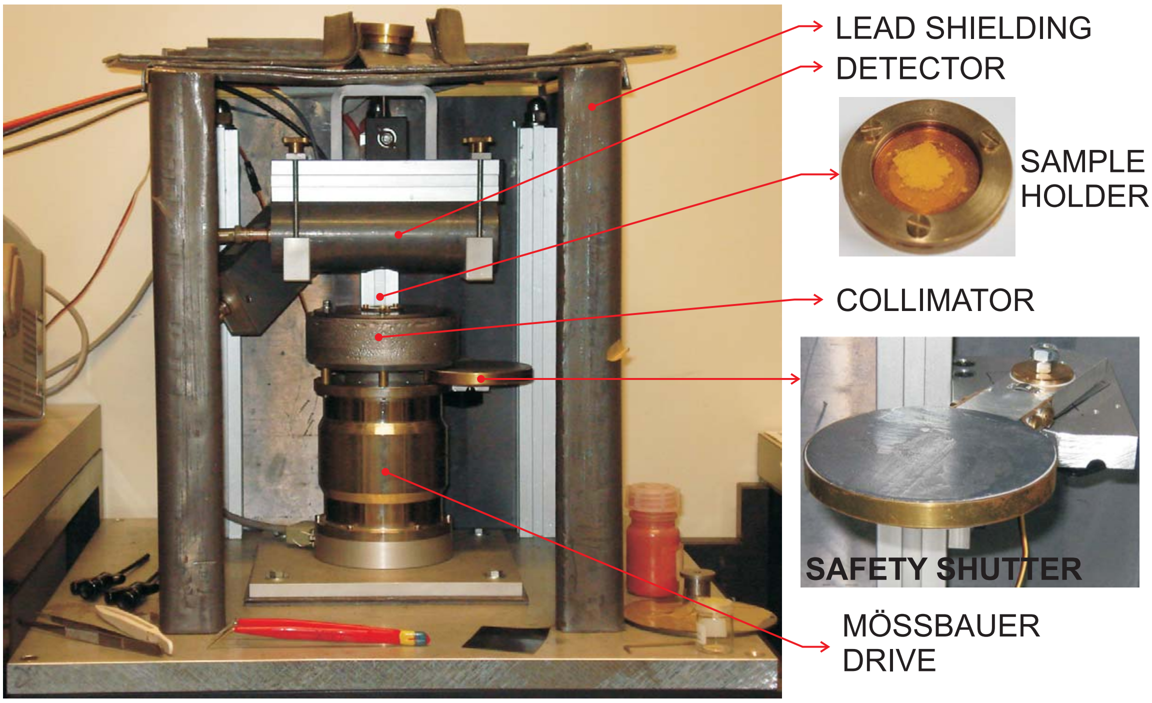

Figure 3.3: Front view of the Mössbauer spectrometer with safety shutter moved outside the γ-ray axis. The sample is placed via the top door. The front door is removed for taking the photo.

from ~9 mm thick lead (see fig. 3.3). It is connected to a servo system, which provides a sliding movement, i.e. the shutter can be moved in and out of the gap between the collimator and Mössbauer drive (see fig. 3.3 in which the shutter is moved outside allowing the γ-rays for measurement).

3.4 Spectrometer geometry and source properties

The spectrometer is vertically aligned, i.e. the Mössbauer drive, sample and detector are fixed above each other such that the γ-rays pass vertically. A photo of the spectrometer is shown in fig. 3.3. The source is not seen in fig. 3.3, as it is screwed to an adaptor, which lies somewhere in the middle of the hollow vibrating shaft of the Mössbauer drive. One can fix the source to the top end of the shaft, but there is some chances that the safety shutter may hit the source. After several attempts to get a good spectrum we optimized the various geometrical parameters for the spectrometer as given in table 3.1.

Table 3.1: Geometry of the Mössbauer spectrometer and source properties.

Sample-detector distance (see fig. 3.1)	35 mm
Source-detector distance l	200 mm
Effective diameter of detector window	$\phi = 2r_{\text{eff}} = 7.12$ mm
hole-to-length ratio $d/(2L)$	0.07
Resolution (measured with a 25 μm α-Fe foil)	outer line width=0.25 mm s^{-1}
Type of source	^{57}Co in rhodium metal matrix
Source line width	0.104 mm s^{-1}[a]
Source strength S (measured on 13 Nov 2007)	56.5 mCi (2.0905×10^{9} Bq)[a]
Active diameter of source	5 mm[a]
Emission efficiency for 14.4 keV photons	80%[a]
Lamb-Mössbauer factor f_{s} at 293 K	0.78[a]

[a] As provided by Cyclotron Co., Ltd., Russia.

3.5 Calibration and fitting

The calibration of the spectrometer is done by making use of the magnetic hyperfine-split spectrum obtained from an α-Fe foil, the line positions of which are accurately known. A 25 μm thick Fe foil (natural abundance of ^{57}Fe is 2.1%), purity of 99.5% purchased from Alfa Aesar GmbH & Co. KG, Germany was used for calibration. The interaction between the nuclear magnetic dipole moment μ and the magnetic field H at the nucleus produced by the surrounding electrons or ions is called magnetic dipole interaction or nuclear Zeeman effect and the splitting caused due to such interaction is known as magnetic hyperfine (or dipole) splitting. In the absence of quadrupole interaction, the magnetic dipole interaction splits the nuclear state with I into $(2I+1)$ equally spaced substates, each of these being characterized by the nuclear magnetic spin quantum number m_I. The energy eigenvalue of each level is given by [17]:

$$E_{m_I} = -\mu H m_I / I = -g \mu_{\text{N}} H m_I, \tag{3.4}$$

where $g(=g_{\text{g}}$ or $g_{\text{e}})$ is gyromagnetic factor. The subscripts e and g represent excited and ground state, respectively. μ_{N} is the nuclear magneton. The separation between the adjacent substates is $g\mu_{\text{N}}H$. Gamma transitions between the substates of the excited state and those of the ground state are almost exclusively magnetic dipole

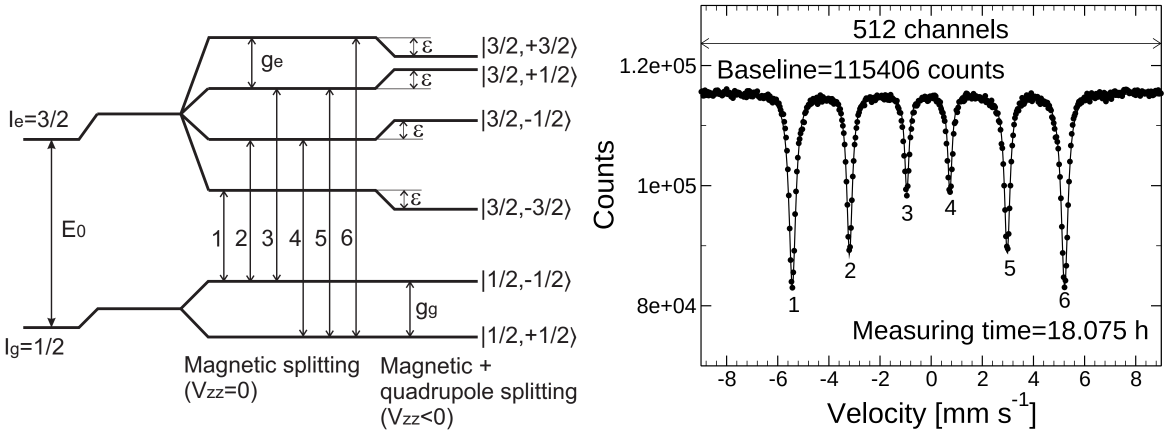

Figure 3.4: Pure magnetic hyperfine (i.e. $H \neq 0$ and $V_{zz} = 0$) structure of ^{57}Fe. For $\epsilon = 0$, all the excited substates are equidistant, whereas in the case when both interactions ($H \neq 0$ and $V_{zz} \neq 0$) are present, the excited substates are shifted by $4\epsilon = eQV_{zz} = (p_6 - p_5) - (p_2 - p_1)$. If $V_{zz} < 0$, the substates $|+3/2\rangle$ and $|-3/2\rangle$ are lowered and the other two substates are raised. On the right the Mössbauer spectrum of the α-Fe foil at RT is shown. The experimental count rate excluding the Mössbauer effect is 908 counts s^{-1} (=baseline×512/time). This spectrum was measured immediately after measuring the PHS and fixing the range for the 14.4 keV peak as shown in fig. 3.2.

(M1) transitions, and therefore, only transitions with $\Delta I = 1$, $\Delta m = 0, \pm 1$ are allowed. For ^{57}Fe, the six transition lines are shown in fig. 3.4.

Using a single-line source, one would expect a resonance sextet, the centre of which may be shifted from zero Doppler velocity due to electric monopole interaction (isomer shift). For ^{57}Fe, the nuclear magnetic moments of the excited μ_{e} and ground state μ_{g} are -0.15532 and 0.090604, respectively, in terms of nuclear magneton $\mu_{\mathrm{N}} = 3.15245 \times 10^{-8}$ eV T^{-1} and the internal magnetic field H_{int} is 33.0 T. The moments are related to the g-factors via $g = \mu/I$ and the μ-values are taken from [23]. By using these values, one can calculate the separation between any two lines of the hyperfine structure. For example, the separation between the lines p_1 and p_6 is given by:

$$p_6 - p_1 = c \cdot H_{\mathrm{int}} \cdot \mu_{\mathrm{N}}(g_{\mathrm{g}} - 3g_{\mathrm{e}})/E_{\gamma}. \tag{3.5}$$

Taking c (speed of light in vacuum) in m s^{-1}, H_{int} in T and E_{γ}=14.413 keV one obtains 10.643 mm s^{-1}. This value is used to check the velocity of the drive. If a deviation is found, then one has to reset the velocity. Because of the cubic crystal symmetry of iron, the quadrupole splitting is zero ($V_{zz} = 0$). After adding the two spectra, which are mirror images of each other, the channels N_i are converted to velocity v_i units according to:

$$v_i = (N_i - N_{\mathrm{Fe}})2v/(N-1), \tag{3.6}$$

where N_{Fe} is the channel number of the centre of the spectrum obtained from α-Fe foil and the isomer shift obtained from that spectrum is relative to α-Fe foil. If $N_{\mathrm{Fe}} = (N-1)/2$, then the isomer shift will be relative to the source. N is the number of data points. v is the drive velocity at which the spectrum is measured, in mm s^{-1}. The above relation (3.6) is valid only for constant acceleration mode—triangular source motion. All experimental data were fitted by the least-squares method using the following Lorentzian functions (same as eq. (2.7)):

$$f(v) = B - \sum_i \frac{I_i(\Gamma_i/2)^2}{(v_0 - v_i)^2 + (\Gamma_i/2)^2}, \tag{3.7}$$

where I_i, v_i and Γ_i are the height, position and full width at half maximum, respectively, of the i^{th} Lorentzian. B is the base line of the spectrum.

3.6 Notes

The isomer shift of an α-Fe foil relative to the ^{57}Co source in a rhodium matrix is -0.109 mm s^{-1*} with both source and Fe foil at RT. If the source is at 4.2 K and the Fe foil at RT then the isomer shift relative to α-Fe will be -0.235 mm s^{-1}. All the isomer shifts throughout this thesis are given relative to an α-Fe foil at RT, unless explicitly specified. Calibration was done using a standard 25 µm thick Fe foil. The internal hyperfine magnetic field of α-Fe at RT is 33.0 T, which is equivalent to the distance between the outer lines of the Mössbauer spectrum of the α-Fe foil at RT (10.643 mm s^{-1}). This distance is used for calibration. All the frozen solution samples were measured on a Mössbauer spectrometer at the Technische Universität München operated by Dr Uwe van Bürck and Prof. F. E. Wagner. In these measurements, both sample and source (Co/Rh source) were maintained at 4.2 K and the source follows a sinusoidal motion. RT measurements (except the RT spectrum shown in chapter 6) were performed on the spectrometer described in this chapter with a constant acceleration (triangular wave motion) mode of source motion.

---

*This shift value is valid for the spectrometer described in this chapter. It slightly depends on the purity of α-Fe foil used for calibration, hence, it usually varies from -0.102 to -0.114 mm s^{-1}.

Chapter 4

Nuclear inelastic scattering (NIS)

4.1 Introduction

In Mössbauer spectroscopy, the process of recoil-free absorption or scattering of resonant photons by an ensemble of nuclei is essentially an elastic scattering process. The corresponding probability is given by the Lamb-Mössbauer factor f_{LM}. Incident photons $E \neq 14.4$ keV are treated as nonresonant absorption, which may constitute the background and baseline of the spectrum. However, nuclear resonant scattering is also possible for the incident photons $E \neq 14.4$ keV due to the influence of lattice dynamics on the absorption of γ-quanta by nuclei. In this case, the interaction involves the recoil of the scattering nucleus with energy transfer from or to the crystal lattice in order to fulfil the resonance condition. This process of absorption with recoil (recoil fraction, $1 - f$) is called nuclear inelastic scattering (NIS), which appears as sidebands over an energy range of about ±100 meV.

Soon after the discovery of the Mössbauer effect, it was proposed by theorists that lattice vibrations should occur as sidebands of the absorption line, permitting the measurement of a phonon spectrum [24, 25]. However, in a conventional Mössbauer experiment it is very difficult to observe such vibrational sidebands that appear roughly ±100 meV in the vicinity of a resonance transition energy. The main reasons, which do not allow for the observations of sidebands are: 1. to scan an energy range of ±100.0 meV with Doppler shift, one needs a velocity of about 2080.1 m s^{-1} and it is practically difficult to achieve such a high velocity with a good count rate and 2. a very intense radiation is required since the energy range of the phonon spectrum is typically 10^7 times broader than the nuclear line width and the spreading of the recoil absorption probability over this energy range makes the cross section of inelastic scattering weak. Therefore, a very intense beam with typically 10^8 phonons s^{-1} is required and hence NIS is generally performed at synchrotron radiation sources. NIS does not deal with phonon dispersion relations but gives direct access to the vibrational density of phonon states (VDOS). In this chapter, the basics of synchrotron radiation as well as the theoretical and experimental aspects of NIS will be briefly discussed.

4.2 Basics of synchrotron radiation

Synchrotron radiation is electromagnetic radiation which is emitted by charged particles moving very close to the speed of light in vacuum. When electrons are accelerated to relativistic speed in a circular orbit while moving in alternating magnetic field, photons are emitted tangent to the orbit, see fig. 4.1. This kind of radiation was first observed in 1947 from electrons orbiting in a synchro-cyclotron [27, 28]. At the European Synchrotron Radiation Facility (ESRF), the electrons with an energy of 100 keV are generated from a triode gun and accelerated to an energy of 200 keV in a linear accelerator (linac). After a transfer line, the electrons enter the booster synchrotron of circumference of 300 m where the electrons after orbiting

Table 4.1: Comparison between a third-generation undulator synchrotron source and a commercially available ^{57}Co Mössbauer source with 10 mCi activity (values taken from [26]). The “ ph ” stands for photons.

Property	Synchrotron radiation	^{57}Co radioactive source
Spectral flux (ph s^{-1} eV^{-1})	2.5×10^{12}	2.5×10^{9}
Brightness (ph s^{-1} eV^{-1} sr^{-1})	2.8×10^{22}	2.5×10^{12}
Brilliance (ph s^{-1} eV^{-1} sr^{-1} mm^{-2})	2.8×10^{22}	2.5×10^{10}
Typical beam size (mm^2)	1×1	10×10
Focused beam size (μm^2)	6×6	—
Energy resolution	—	4.7 neV
Polarization	linear or circular	unpolarized

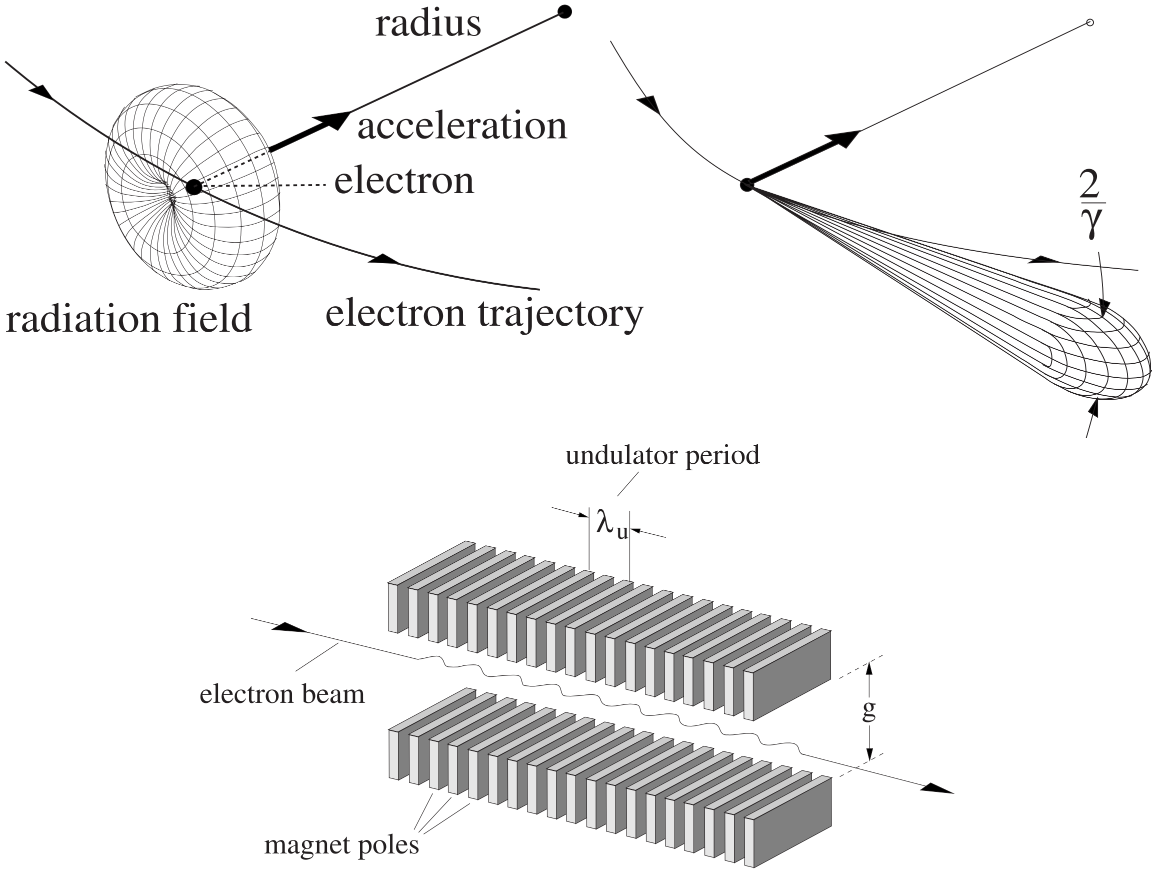

Figure 4.1: Emission of synchrotron radiation from a accelerated electron moving radially for nonrelativistic (top left) and relativistic velocities (top right), $1/\gamma = 8.46 \times 10^{-5}$ rad is the opening angle of the radiation cone. Schematic of an undulator (bottom) that forces the electrons on a sinusoidal trajectory. λ_u and g are the adjustable parameters of the undulator for controlling the beam (figures taken from [23]).

several turns will reach a nominal energy of 6.04 GeV. These high-energy electrons are then injected into a large 844.4 m circumference storage ring where they circulate in an ultra high vacuum environment, at a nominal energy, for many hours. In order to compensate for radiation losses, i.e. to accelerate electrons permanently inside the storage ring 3 radio frequency cavities are provided that supply the electric field to the storage ring.

Synchrotron radiation possesses special properties which distinguish it from all other X-ray sources, for example, brilliance, time structure and polarization. For comparison with a typical Mössbauer source, see table 4.1. After the original proposal by Ruby [29] that synchrotron radiation could be used for Mössbauer experiments, following the pioneering nuclear resonance experimental work in 1985 [30], the first NIS spectrum was reported in 1995 by Seto et al. [31]. Extracting the VDOS of ^{57}Fe from NIS spectrum is discussed in [32, 33].

All NIS experiments presented in this dissertation were performed at the nuclear resonance beamline ID18 of ESRF, Grenoble (in France), operated either in 16-bunch mode or hybrid mode. Bunches are the collection of electrons that occupy a finite number of stable positions within an orbit. The 16-bunch mode of operation of synchrotron provides a time window of 176 ns between bunches, i.e. every 176 ns, one synchrotron pulse hits the sample ($844.4\ \mathrm{m}/(16c) = 176$ ns). In hybrid mode $24 \times 8 + 1$ bunches providing a time window of 88 ns between bunches, i.e. every 88 ns, 8 synchrotron pulses hit the sample. In this mode the whole storage ring is divided into 32 bunches with 88 ns separation ($844.4\ \mathrm{m}/(32c) = 88$ ns), that includes 8 adjacent empty bunches with 2.84 ns separation and in the middle of 8 adjacent bunches a single bunch with a current of 4 mA is enabled. Very high brilliance synchrotron radiation is produced by insertion devices, which consist of periodic arrangement of magnetic structures (undulator) installed in the straight sections of the storage ring, see fig. 4.1 (bottom). Their main purpose is to force the electrons on a sinusoidal trajectory and enhance the emitted radiation without affecting the stored electron beam.

4.3 Instrumentation and measurement

The schematic of the experimental setup for NIS is shown in fig. 4.2. More details can be found in the beamline description [34, 35]. The synchrotron radiation produced from the electron consists of a broad energy distribution from 0 to 6.03 GeV. For NIS on iron compounds, the synchrotron radiation from the undulators is tuned with its specific harmonics such that the peak of emission centered around 14.4 keV is produced. In the ID18 beamline, there are three undulators: one U32 and two U20. The synchrotron radiation produced from the U32- and U20-undulators are tuned with their third and fundamental harmonic, respectively, to 14.4 keV*. This 14.4 keV

---

*Tuning and naming scheme of undulators and number of undulators used widely depend on the instrumentation available at the time of measurement. It may be changed by the local beamline scientist. Therefore, the scheme given here cannot be taken as ultimate choice.

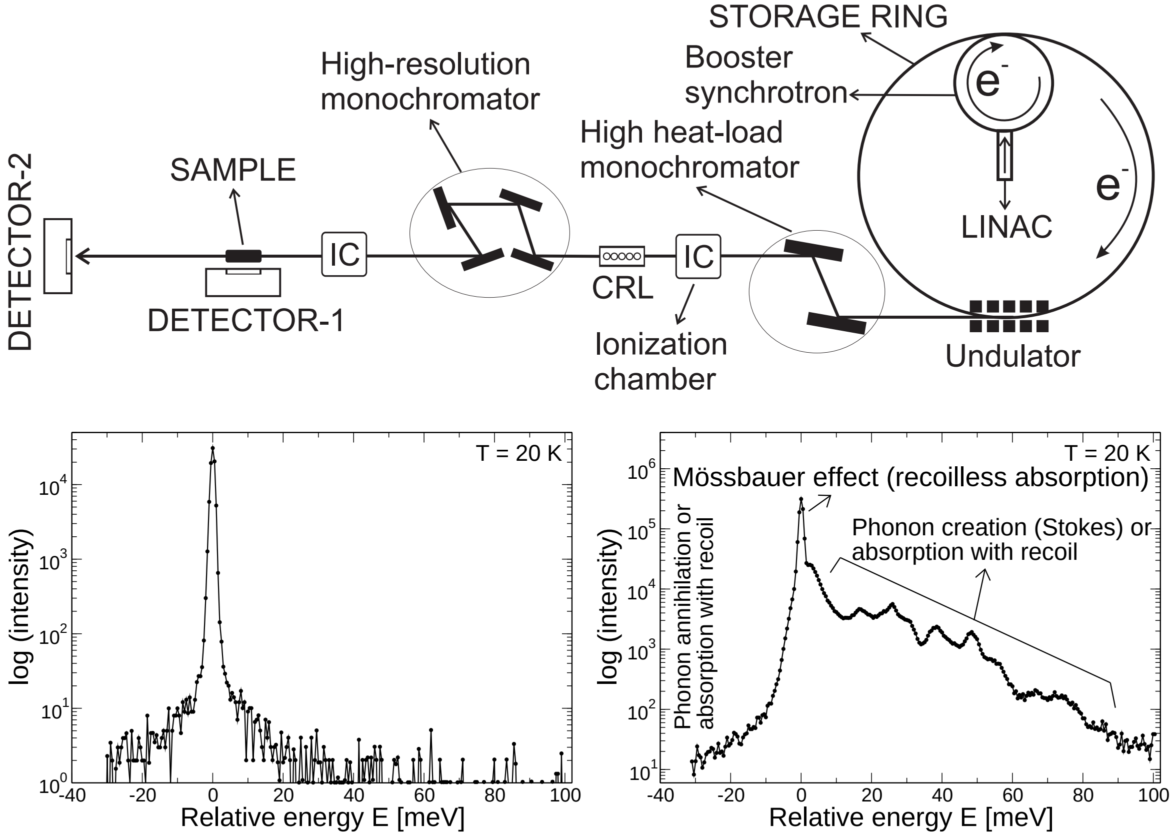
STORAGE RING
Booster synchrotron
High-resolution monochromator
High heat-load monochromator
e-
e-
LINAC
DETECTOR-2
SAMPLE
IC
IC
CRL
DETECTOR-1
Ionization chamber
Undulator
T = 20 K
log (intensity)
Relative energy E [meV]
T = 20 K
Mössbauer effect (recoilless absorption)
Phonon creation (Stokes) or absorption with recoil
Phonon annihilation or absorption with recoil
log (intensity)
Relative energy E [meV]

Figure 4.2: Top: schematic sketch of a NIS setup. Bottom: As an example, the NIS spectrum (right) recorded by detector-1 and instrumental function recorded by detector-2 (left) of a trinuclear complex shown in fig. 6.1. Note the phonon annihilation part in the NIS spectrum is close to zero.

X-ray coming out of the undulators has an energy bandwidth of approximately ∼300 eV, which is not directly suited for NIS experiments because of the large fraction of “ unwanted ” photons (having energies outside the narrow resonance bandwidth) that only overload the detector. Therefore, the bandwidth has to be reduced strongly which is done in two stages. In the first stage, the bandwidth is reduced down to a few eV by a high heat-load monochromator, which consists of two independent silicon crystals with reflections of (1 1 1). In the second stage, a further reduction down to approximately 1 meV by a high-resolution monochromator (HRM) occurs. The HRM consists of four high-symmetry silicon crystals either (inner: (4 0 0) and outer: (12 2 2)) or (inner: (4 4 0) and outer: (10 6 4)) reflection scheme. By tuning the high-resolution monochromator crystals even further, one can vary around the

14.4 keV level. The flux of the radiation is monitored in ionization chambers that are placed before and after the HRM. A beryllium compound refractive lens (CRL) is placed before the HRM, to collimate the beam.

After passing through all the sections, the beam finally irradiates the sample. For measuring the photons that are scattered from the sample, silicon-based avalanche photodiode (APD) detectors are used. APD detectors are highly efficient detectors used in almost all kinds of nuclear resonance scattering experiments. For a recent review of the APD detector technology, see [36]. The X-ray beam after irradiating the sample scatters both incoherently and coherently. These scattered photons are monitored by two APD detectors. The first APD detector located ~1 mm from the sample perpendicular to the X-ray beam, counts the intensity of the incoherently scattered photons (both elastical and inelastical). This detector has an active window area of 10×10 mm^2 and measures the NIS spectrum. The second APD detector (generally four detectors placed one after other each with a surface area of 5×5 mm^2), located ~2 m far from the sample in forward direction of the incident beam, counts the intensity of coherent and elastically scattered photons.

In order to obtain a NIS spectrum, the electronic scattering and the fluorescence resonant photons are discriminated by adopting a proper electronic system. The

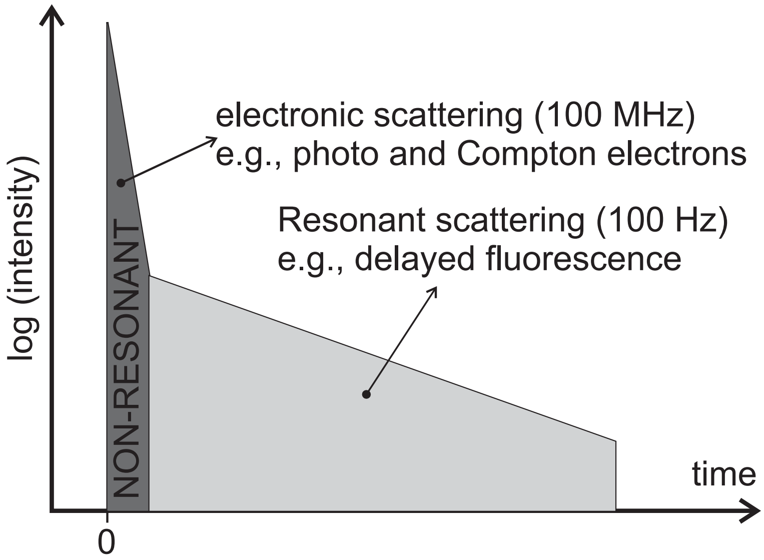
log (intensity)
electronic scattering (100 MHz)
e.g., photo and Compton electrons
Resonant scattering (100 Hz)
e.g., delayed fluorescence
NON-RESONANT
time
0

Figure 4.3: Synopsis of the time evolution of the scattered intensity of a material that contains the resonant nucleus after excitation by a synchrotron pulse.

electronic scattering means the emission of nonresonant photons and electrons, which occur very fast, i.e. within a few ps after the nucleus receives the synchrotron pulse. As shown in fig. 4.3, at time zero the synchrotron pulse excites a material containing a resonant nucleus. The prompt pulse is more highly intense than the delayed fluorescence. Therefore the two processes, i.e. electronic scattering and delayed events should be discriminated properly. This is achieved by a counting system, which consists of fast electronics synchronized with the revolutions of the electron beam, i.e. the bunch pattern of the storage ring such that the detector counts only the events between the pulses of synchrotron radiation, in other words, only the delayed quanta.

An excited nucleus deexcites via two channels: radiative decay (emission of γ-ray) and internal conversion, for details see section 2.2 and fig. 2.2 of chapter 2. For the deexcitation of the 14.4 keV transition in ^{57}Fe, the probability of radiative decay and internal conversion are 10.5% and 89.5%, repectively. Thus the dominating decay is via internal conversion, so that the Fe K-α fluorescence X-rays (6.4 keV) dominate in the detected photons. As the internal conversion process is nearly isotropic, the exact position of the detector does not matter. For this reason it seems that phonons with any momentum, which is allowed by the dispersion relations for a particular energy transfer, contribute equally to NIS. However, strictly, this is not valid for all samples since the inelastic nuclear resonant absorption, which is independent of the direction of the scattered wavevector, but is dependent on the direction of incident wavevector, and therefore it is anisotropic in general [37, 38]. In such cases only the partial phonon VDOS of the resonant atom are obtained where the contributions from the vibrational modes of the resonant atoms are weighted by the projections of their phonon polarization vectors on the direction of the incident beam (for more details see [23]). The anisotropy vanishes only for spherically symmetric samples, i.e. for cubic crystals (also depends on the specific basis of the unit cell) and polycrystalline samples, NIS provides the total phonon VDOS.

4.4 Sample environment and holder

All NIS spectra of frozen liquid samples were recorded during several beamtimes at 20 or 70 K using a helium flow cryostat. The sample holders were made from pure copper and some from pure aluminium for a good thermal conductivity. A 25 µm

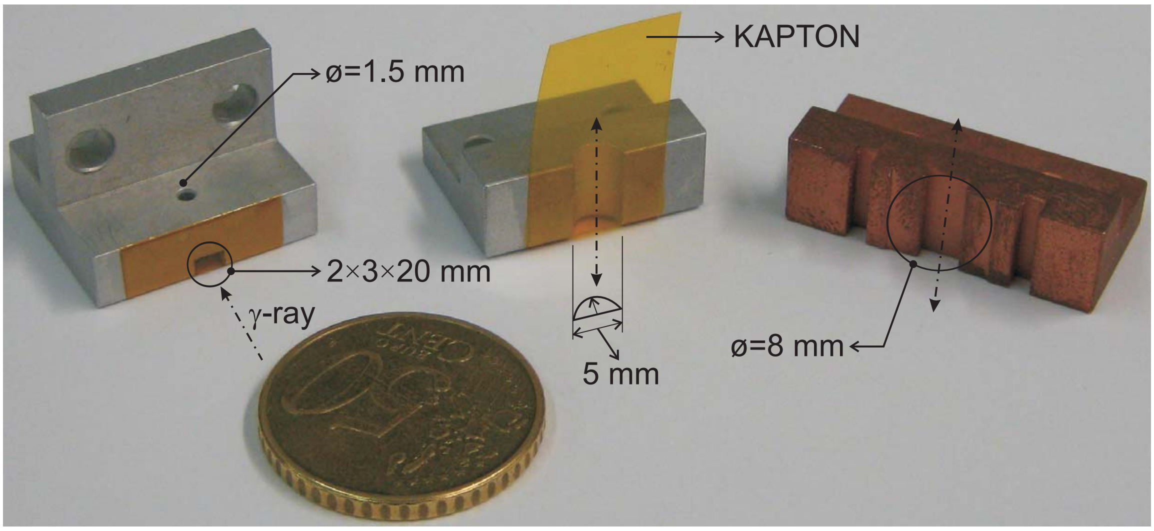

Figure 4.4: Left: liquid sample holder with a small hole $\phi = 1.5$ mm for injecting the sample liquid; middle: powder sample holder pre-glued on two sides with a kapton foil before loading the powders; right: holder for mounting solid sample in the form of a 8 mm disc.

thick kapton foil glued to the holder is used as a window for the X-ray transmission, for details see fig. 4.4. For the liquid sample holders, the glue used was EPO-TEK 377®, which is a two-component glue (cure time of 1 h at 400 K). For the powder samples different holders were used as shown in fig. 4.4. All the sample holders were coated with parylene-D so as to avoid the corrosion of the copper by acetic acid. The powder samples were pressed into disk shapes, sealed between two thin beryllium sheets and then attached to the sample holder. Some powder samples were mounted directly in the copper holder and then sealed with a standard epoxy glue, for example a two-component UHU®.

The holder with the sample powder is fixed to the coldfinger of the cryostat by screws. Since some of the liquid samples were sensitive to air, the mounting of such samples was done after freezing the sample (dropping the sample holder in liquid nitrogen) and then quickly attached to the coldfinger precooled at 20 K. During sample mounting, care was taken that the temperature of the liquid sample does not raise above ~100 K. A cernox temperature sensor was attached to the sample holder for monitoring the sample temperature.

4.5 Basic features of NIS

The energy tunability of synchrotron radiation in the range of meV around the nuclear transition energy E_γ is a necessary condition to measure a NIS spectrum. In our experiments the energy E of the incoming synchrotron radiation was tuned from -20 meV to $+100$ meV around the nuclear resonance in steps of 0.25 meV. The inelastic scattering process is spatially incoherent; therefore the inelastically scattered photons are emitted in all directions, i.e. in a 4π solid angle.

A NIS spectrum shown in fig. 4.2 (bottom), which consists of three parts: the phonon annihilation ($E < E_\gamma$) part, the central elastic peak at $E = E_\gamma$ (Mössbauer peak that corresponds to recoilless absorption) and the phonon creation ($E > E_\gamma$) part. Phonon annihilation means that the incident photon gains some energy from the existing phonon to excite the nucleus or in other words, the X-ray energy is too small so phonons must be annihilated, i.e. vibrations must be deexcited to produce resonant excitation. The central peak is the dominating peak, which corresponds to the elastic scattering process. This peak involves no energy transfer to the lattice and contains mostly fluorescence radiation after absorption at $E = E_\gamma$. Unlike in conventional Mössbauer spectroscopy, synchrotron-based NIS technique does not directly resolve the hyperfine splitting of the recoilless resonance at $E = E_\gamma$. The high-energy sidebands ($E > E_\gamma$) are the region of phonon creation. In this region the energy of the X-ray is too large to excite the nuclear resonance directly, and therefore the phonons must be created (i.e. vibrations are excited) simultaneously. As mentioned in section 4.3, the forward detector monitors the elastic scattering at nuclear resonance ($E = E_\gamma$), which provides the resolution of the NIS setup, i.e. the energy bandwidth of the high-resolution monochromator. Moreover, this peak gives a reference for the position of the nuclear resonance.

4.6 Data evaluation

In a NIS experiment, the incident energy shifted by E relative to the nuclear resonance E_γ, and the photons that are re-emitted after the nuclear absorption, are monitored.

Therefore in the following, the energy E is given relative to E_γ. The total yield of the delayed K-α fluorescence photons is given by:

$$I(E) = I_0\,\rho_{\mathrm{eff}}\,\sigma_0\,\frac{\eta_{\mathrm{K}}\,\alpha_{\mathrm{K}}}{1+\alpha}\,\frac{\pi}{2}\Gamma_{\mathrm{nat}}\,S(E) \Longrightarrow I(E) = \mathrm{Const}\,\rho_{\mathrm{eff}}\,S(E), \tag{4.1}$$

where I_0 is the incident photon flux, σ_0 is the nuclear resonant cross section (given by eq. (2.8)), η_{K}(=0.352) is the K-shell fluorescence yield, α_{K}(=7.7) is the internal conversion coefficient of the electron in the K-shell, i.e. the ratio of the conversion electron emission from K-shell (70.4) and γ-ray emission (9.2), probabilities (for details see fig. 2.2 of chapter 2) and α is the total internal conversion coefficient. Γ_{nat} is the natural line width of the resonant nucleus. $S(E)$ is the normalized absorption probability per unit of energy. The effective area density ρ_{eff} of nuclei also accounts for absorption within the material and it is not constant over the measured energy range [32].

Assuming that the sample material behaves like a harmonic lattice with well-defined phonon states, $S(E)$ can be expanded in multiphonon contributions as follows [39]:

$$S(E) = f_{\mathrm{LM}}\left(\delta_\Gamma(E) + \sum_{n=1}^{\infty} S_n(E)\right), \tag{4.2}$$

where f_{LM} is the Lamb-Mössbauer factor of the nuclei, $\delta_\Gamma(E)$ is a Lorentzian function of width Γ. $\delta_\Gamma(E)$ can be approximated by the Dirac δ-function $\delta(E)$, i.e. $\lim_{\Gamma\to 0}\delta_\Gamma(E) = \delta(E)$ because Γ is several orders of magnitude smaller than typical phonon energies.

According to the relation (4.2), the phonon spectrum $I(E)$ can be decomposed into an elastic part that is described by a δ-function and an inelastic part $S(E)$:

$$I(E) = \mathrm{Const}\,f_{\mathrm{LM}}\left(\rho_{\mathrm{eff}}\delta(E) + \rho_{\mathrm{eff}}\sum_{n=1}^{\infty} S_n(E)\right). \tag{4.3}$$

It should be kept in mind that the area of the central elastic peak is not proportional to the recoilless fraction f_{LM} whereas the area of the inelastic peak is proportional to the recoil fraction $(1-f_{\mathrm{LM}})$. The reason is a large saturation at resonance due to a high cross section of elastic absorption and the influence of the forward scattering on the yield of atomic fluorescence [40]. Therefore, ρ_{eff} strongly decreases at nuclear resonance and the ratio between the elastic peak and the remaining spectrum is not well defined. This peculiar problem is solved by normalization of $I(E)$ in (4.3) by a procedure as described in [32] by using Lipkin's first sum rule [41] as discussed below.

Lipkin has shown that the average energy transfer to the lattice per photon emission is just the recoil energy E_{R} of the free atom. The first moment (Lipkin's first sum rule) of the energy spectrum of inelastic absorption equals the recoil energy E_{R} [41]:

$$\int_{-\infty}^{+\infty} E\,S(E)\,\mathrm{d}E = E_{\mathrm{R}}. \tag{4.4}$$

By applying the sum rule (4.4) to the measured phonon spectrum we obtain:

$$\int I_{\mathrm{norm}}(E)\,\mathrm{d}E = I(E)\frac{E_{\mathrm{R}}}{\int E\,I(E)\,\mathrm{d}E} = 1. \tag{4.5}$$

Thus the spectrum is normalized to 1. In the above relation (4.5), the convolution of the instrumental function, which appears as an additional small correction factor, is not included. The normalization procedure is not affected by the central elastic peak, which is symmetric around $E = 0$ and provides the resolution function of the instrument, hence, does not contribute to the integral in (4.4).

In order to calculate the recoil fraction $(1 - f_{\mathrm{LM}})$ of the nuclear absorption from the area of the normalized spectrum, the elastic central peak has to be subtracted from the NIS spectrum. This is done by fitting and subtraction or by intrapolation of the experimental data in a certain energy range around the central peak [42]. The normalization process can also be performed after subtraction of the central elastic peak for the reason just mentioned above. After subtraction of the elastic central peak from the normalized phonon spectrum, the resulting inelastic part $I'_{\mathrm{norm}}(E)$ is equivalent to the n-phonon part $f_{\mathrm{LM}} \sum S_n(E)$ and for f_{LM} we can write (removing the first term in eq. (4.3)):

$$1 - f_{\mathrm{LM}} = \int I'_{\mathrm{norm}}(E)\,\mathrm{d}E \equiv f_{\mathrm{LM}} \sum S_n(E) \Longrightarrow f_{\mathrm{LM}} = 1 - \int I'_{\mathrm{norm}}\,\mathrm{d}E. \tag{4.6}$$

The f_{LM} obtained from eq. (4.6) is much more precise than the value obtained from conventional Mössbauer spectroscopy. Moreover, f_{LM} can be determined without any knowledge about the effective thickness or number of Mössbauer nuclei in the sample (see eq. (2.25) of chapter 2; more details in [43]).

In the harmonic approximation, the one-phonon contribution $S_1(E)$ is directly related to the phonon VDOS $g(E)$ [24, 39]:

$$S_1(E) = \frac{E_{\mathrm{R}}\,g(|E|)}{E(1 - \mathrm{e}^{-E\beta})}, \tag{4.7}$$

with $\beta = 1/(k_\mathrm{B}T)$ and k_B is the Boltzmann constant. The higher-order contributions $S_n(E)$ for $n \geq 2$ are obtained by convolution of $S_{n-1}(E)$ with $S_1(E)$:

$$S_n(E) = \frac{1}{n}\int_{-\infty}^{+\infty} S_{n-1}(E-E')\, S_1(E')\, \mathrm{d}E'. \tag{4.8}$$

Once after extracting $S_1(E)$ from the measured NIS spectrum with all the above information, the VDOS $g(E)$ is derived using eq. (4.7).

Alternatively, f_LM is related to the VDOS as follows (eq. (21) in [24]):

$$f_\mathrm{LM} = \exp\left(-E_\mathrm{R}\int_0^{\infty} \frac{g(E)}{E}\,\frac{1+\mathrm{e}^{-\beta E}}{1-\mathrm{e}^{-\beta E}}\,\mathrm{d}E\right). \tag{4.9}$$

The above eq. (4.9) can be used to check the deviation of the VDOS for consistency with the value obtained from (4.6). According to (4.9), $g(E)$ is weighted by $1/E$ in the low-temperature limit and by $1/E^2$ in the high-temperature limit.

Using the Bose-Einstein statistics (eq. (2.11) in section 2.4.2 of chapter 2), one may write:

$$n_\mathrm{B} = \frac{1}{\mathrm{e}^{E\beta}-1}; \quad n_\mathrm{B}+1 = \frac{1}{1-\mathrm{e}^{-E\beta}}; \quad \frac{n_\mathrm{B}+1}{n_\mathrm{B}} = \mathrm{e}^{E\beta}, \tag{4.10}$$

where n_B is the Bose occupation factor. Using this relation, the single-phonon term $S_1(E)$ can be rewritten for the phonon annihilation and creation separately as follows:

$$\text{for annihilation} \rightarrow E<0: \; S_1(-E) = \frac{E_\mathrm{R}\, g(|E|)}{-E(1-\mathrm{e}^{E\beta})} = \frac{E_\mathrm{R}\, g(|E|)}{E}\, n_\mathrm{B}, \tag{4.11}$$

$$\text{for creation} \rightarrow E>0: \; S_1(E) = \frac{E_\mathrm{R}\, g(|E|)}{E(1-\mathrm{e}^{-E\beta})} = \frac{E_\mathrm{R}\, g(|E|)}{E}\,(n_\mathrm{B}+1). \tag{4.12}$$

From the above eqs. (4.11) and (4.12) the energy spectrum of absorption probability satisfies the detailed balance rule as shown below:

$$S_1(E) = \mathrm{e}^{\beta|E|} S_1(-E). \tag{4.13}$$

In eq. (4.13), $S_1(E)$ and $S_1(-E)$ accounts for the absorption probability of the left side (phonon annihilation) and right side (phonon creation), respectively. The resulting VDOS is derived as:

$$g(E) = \frac{E}{E_\mathrm{R}}(S_1(E)+S_1(-E))\tanh\left(\frac{\beta E}{2}\right) \quad \text{with} \quad E \geq 0. \tag{4.14}$$

According to eq. (4.13), for any particular energy the ratio of phonon creation and phonon annihilation probability is given by $\mathrm{e}^{\beta|\mathrm{E}|}$. The accurate temperature of the sample can be obtained from this detailed balance calculation. Although eq. (4.13) is valid for the entire spectral range in practice it is calculated for the verification of temperature between the features roughly from 2–10 meV. Below 2 meV the data suffers from statistical accuracy due to the subtraction of the elastic peak and above a certain energy, ∼40 meV, the count rate for the low-energy side is usually low [44].

From the above discussions (see also eqs. (4.11) and (4.12)) it is clear that the phonon annihilation part is proportional to n_B and vanishes at low temperatures. The phonon creation part is proportional to $(n_\mathrm{B}+1)$ and remains finite even at $T=0$ which means $f_\mathrm{LM} \neq 1$. Since all our NIS measurements were performed at 20 K, the phonon annihilation part is weak as an incident X-ray can gain energy only from an existing phonon, i.e. an excited vibration.

Chapter 5

Reaction intermediates in the $FeCl_3$-catalyzed Michael reaction

5.1 Introduction

In this chapter, the application of nuclear inelastic scattering (NIS) to a well-known reaction is presented. The main idea of the work presented in this chapter is to show how reliably this technique can be applied to a well-known reaction before applying it to frozen solutions of the new compounds, which is presented in chapter 6. For this purpose we chose the Michael reaction, which is one of the most important carbon-carbon bond-forming reactions in organic chemistry. To our knowledge the first reported literatures on NIS experiments with solutions are [45] and [46]. Both of them were performed at room temperature. The first one deals with the atomic motion of Mössbauer ions in hydrochloric acid and experimentally determining the recoil energy from the shift of the elastic peak of the NIS spectrum towards high energy. In the second literature despite of the poor instrument resolution (∼9 meV), authors reported by observing one intramolecular vibration that NIS can also be applied to solutions to study the vibrational dynamics of the Mössbauer nucleus. The sample was an iron bipyridine complex. Then, NIS on frozen solutions was mainly performed on heme proteins like myoglobin and cytochrome porphyrins [47, 48, 49, 50], and nonheme proteins [51, 52, 53], which are mostly consisting of iron-sulphur clusters. However, NIS was never performed on homogeneous catalytic reactions for predicting possible reactive intermediates, formed in solution. Therefore, before applying NIS

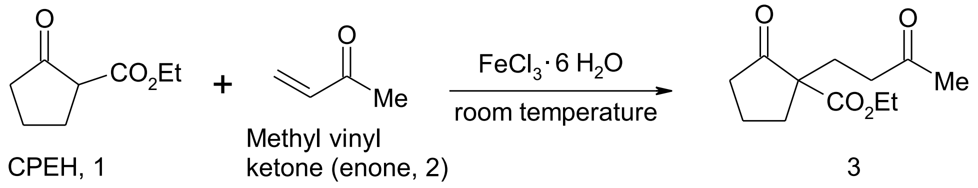

Figure 5.1: Reaction scheme of the Fe(III)-catalyzed Michael reaction.

on solutions (in our case all solution samples are frozen) to the new compounds (in chapter 6), we first studied the Michael reaction.

In the Michael reaction, ferric chloride hexahydrate ($FeCl_3 \cdot 6H_2O$) catalyzes the addition of 1,3-dicarbonyl compounds to α,β-unsaturated ketones under mild and nonbasic conditions. In the following chapter, a detailed investigation on the chemical species formed during the first reaction step, i.e. 1,3-dicarbonyl compound, ethyl 2-oxocyclopentanecarboxylate (CPEH) in $FeCl_3 \cdot 6H_2O$ using NIS and density functional theory (DFT) calculations will be presented. NIS studies were also performed on three model complexes. The results obtained from NIS were compared with normal mode analysis on the basis of DFT calculations of different isomers of simplified model complexes.

5.2 $FeCl_3$-catalyzed Michael reaction

The Michael reaction is the addition of carbon nucleophiles (donors) to activated unsaturated systems (conjugated acceptors), generally promoted by a base catalyst. With a base in stoichiometric amounts, the coupling of a nucleophile (usually enolate obtained as a result of deprotonation of 1,3-dicarbonyl compound) and α,β-unsaturated ketones or enones takes place under ambient conditions (the reaction scheme is shown in fig. 5.1). It was found by Christoffers et al. [54] that among all metal catalysts, $FeCl_3 \cdot 6H_2O$ seems to be the most efficient and economical with respect to quantitative yield. The Fe(III) catalyst is also environmentally friendly when compared to base catalysts. Hence the Fe(III) catalysts can be a good alternative to the base catalysts for the Michael reaction.

A mechanism for the underlying catalytic cycle for the reaction scheme shown in fig. 5.1 was proposed and corroborated by kinetic studies and DFT calculations is shown in fig. 5.2 [54]. According to the mechanistic scheme shown in fig. 5.2, under

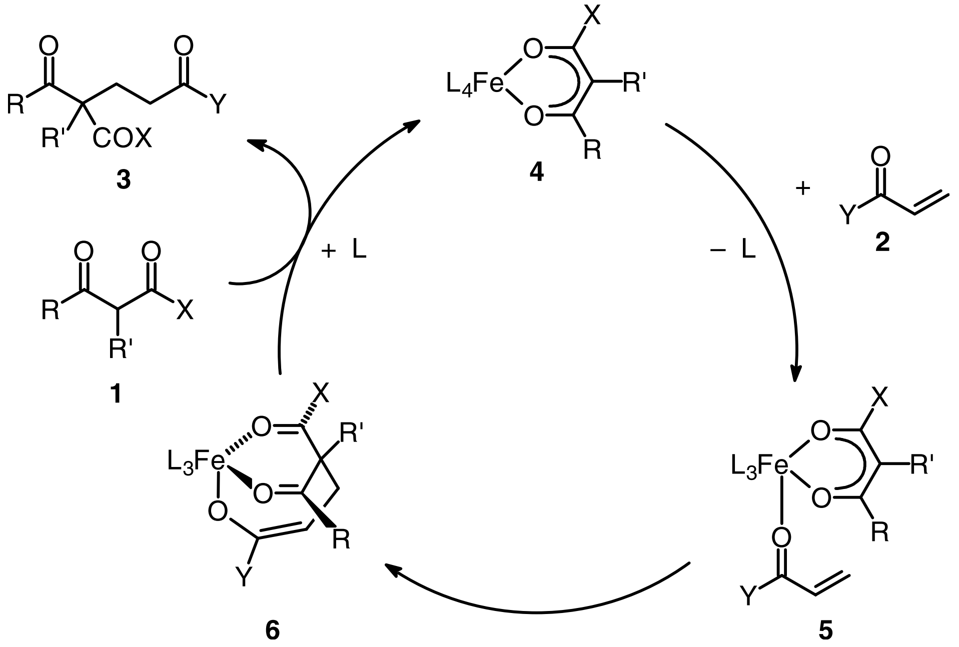

Figure 5.2: Proposed reaction mechanism of the Fe(III)-catalyzed Michael reaction [55].

mild conditions the 1,3-dicarbonyl compound **1** reacts with $FeCl_3 \cdot 6H_2O$ to form 1,3-diketanato species **4**. Then the enone **2** is proposed to coordinate to **4** at the vacant site to form species **5** and subsequently species **6** (see [55, 56] for a detailed explanation of the mechanism of the catalytic cycle to produce **3** and regeneration of **4**). In the reaction shown in fig. 5.1, the iron acts as a Lewis acidic center, which facilitates the reaction of both deprotonation of 1,3-dicarbonyl compound **1** and subsequent coupling to ketones to form **4**. In other words, both reactants are coordinated to the metal center and are activated through its Lewis acidity. In this chapter, the complex species **4** is the subject of investigation.

It was known from studies using X-ray absorption, UV/vis and Raman spectroscopy that the species **4** formed in the first reaction step, i.e. when $FeCl_3 \cdot 6H_2O$ is dissolved in the Michael donor CPEH, can be described as a bis(diketonato)−iron(III) unit containing the anion which is probably coordinated with two water molecules [57]. Based on the mass spectroscopic analysis the counterion (anion) for CPEH is $[FeCl_4]^-$, which acts as an iron sink and therefore decreases the efficiency of the reaction. Moreover, the existence of $[Fe_2Cl_7]^-$ is still under debate [58]. Despite the above discussion, information on the precise geometry and bonding properties is still lacking.

In order to proceed towards further understanding of the species **5** and **6**, and in the overall Michael reaction the species **4** is of crucial importance.

5.3 Materials used and preparation

CPEH and methyl vinyl ketone were purchased from Sigma-Aldrich Chemie, GmbH and used as received. The catalyst $FeCl_3 \cdot 6H_2O$ was prepared from 95.4% ^{57}Fe isotope powder by redox reaction with hydrochloric acid. The model complex $[N(CH_3)_4]^+[FeCl_4)]^-$ was obtained from this enriched $FeCl_3 \cdot 6H_2O$ by reacting it with $[N(CH_3)_4]Cl$. For more detail information on the synthesis of this model complex as well as iron(III) acetylacetonate ($Fe(acac)_3$) refer to [59].

The solution **4** was prepared by dissolving 25 mg (0.13 mmol) of ^{57}Fe enriched $FeCl_3 \cdot 6H_2O$ in 0.35 ml (2.36 mmol) of CPEH, which was stirred for ∼5 min. Soon after mixing, the solution turned to dark violet colour. Using a syringe, 0.12 ml of the solution was injected into the copper sample holder, which had kapton windows for X-ray transmission. The copper holder was coated with parylene-D so as to avoid corrosion of the copper. The entire reaction was carried out in open atmosphere, i.e. the solution was air stable. After injecting, the holder was immediately dropped into liquid nitrogen. This may further avoid the damage of the gluing of kapton to the holder. Three solid samples were measured at 70 K, $Fe(acac)_3$, $[N(CH_3)_4]^+[FeCl_4]^-$, $FeCl_3 \cdot 6H_2O$, and species **4**. Further with enhanced statistics the frozen sample **4** was prepared again as described above and measured at 20 K. The vibrational density of states (VDOS) was extracted from the NIS spectrum using the Fortran program DOS 2.1c as described in [60].

5.4 Normal mode analysis

The geometry optimization and subsequent vibrational frequency calculations were carried out using the DFT B3LYP hybrid exchange-correlation functional [61, 62] and BP86 exchange-correlation functional [63, 64] as implemented in the Gaussian 03 package [65]. The Dunning's correlation-consistent polarized-valence double-ζ basis sets, which were augumented by diffuse functions, were used for the carbon, oxygen and chlorine atoms [66]. For the hydrogen atom, the same basis set was used, but without diffuse functions. For the metal Fe atoms, the core-electron wavefunctions were replaced by the scalar relativistic Stuttgart/Dresden effective core potential (SDD), which was combined with the corresponding basis set for the Fe valence shells as described in reference [67]. For the Fe atom in the anion $[\mathrm{FeCl_4}]^-$, an optimized segmented contracted Gauss-type orbital split-valence basis set with contraction scheme 63311/53/41 was also used [68]. For the sake of comparison with literature, one calculation using the DFT B3LYP theory with the standard basis set 6-31G$*$ for all the atoms was also carried out for the anion $[\mathrm{FeCl_4}]^-$. In all calculations, the spin state for the Fe atom is taken as $S = 5/2$. We note that the calculated vibrational frequencies presented throughout this chapter are not scaled with any adjustable scale factors.

For a given molecule containing N atoms there exist $3N-6$ normal modes of molecular vibrations that can be calculated in the harmonic approximation with DFT methods. The VDOS is extracted from the DFT calculated normal coordinates of all modes assuming the low temperature approximation according to [69, 70]:

$$g(E) = \frac{1}{3}\sum_{j=1}^{3N-6} \frac{m_{\mathrm{Fe}}\, u^2_{\mathrm{Fe},j}}{\sum_{k=1}^{N} m_k\, u^2_{k,j}}\, \delta(E - E_j), \tag{5.1}$$

where m_{Fe} (56.94 a.u.) is the mass of the resonant atom (^{57}Fe), $u^2_{\mathrm{Fe},j}$ and $u^2_{k,j}$ are the mean square displacement of the Fe and the k^{th} atom, respectively. The index j stands for normal vibrational mode, E is the difference between the incoming photon energy and the recoil-free resonance energy, and E_j is the energy of the molecular vibration. The term $\delta(E - E_j)$ is a normalized Gaussian line shape function, which includes a width equal to 1.1 meV (instrument resolution).

5.5 Results and discussion

The cation in the species **4** is a $[\mathrm{Fe}(\mathbf{1}{-}\mathrm{H})_2(\mathrm{H_2O})_2]^+$ complex, which contains two deprotonated CPEH ligands, $(\mathbf{1}{-}\mathrm{H})^-$, and the anion is tetrachloroferrate $[\mathrm{FeCl_4}]^-$. A case study of the theoretically determined vibrational frequencies and Fe$-$Cl bond lengths of the anion together with the literature values is given in table 5.1. From table 5.1, we see that all the theoretical methods based on pseudopotential calculations gave an underestimation of the observed vibrational frequencies, which is, however, less pronounced for the all-electron calculations. Among the pseudopotential

Table 5.1: Experimental vibrational wavenumbers obtained from NIS ($[N(CH_3)_4][FeCl_4]$), Raman ($[Et_4N][FeCl_4]$) and Fe−Cl bond length from X-ray diffraction (XRD) ($[(CH_3)_4N][FeCl_4]$), together with various theoretically predicted data for anion $[FeCl_4]^-$.

Method	E [cm^{-1}]	T_2 [cm^{-1}]	A_1 [cm^{-1}]	T_2 [cm^{-1}]	d (Fe−Cl) [Å]	E/E_h
XRD [72]					2.171/2.178/2.191	
Raman [73]	114	136	330	378		
Raman	113	138	338			
NIS		138		383		
BP86/SDD[a]	90	116	294.1	345	2.238	−1965.321
B3LYP/SDD[a]	94	123	301	348	2.243	−1965.135
BP86/all-e[b]	97	127	313	359	2.230	−3105.063
B3LYP/all-e[b]	96	124	306	355	2.236	−3104.782
B3LYP/6-31G*[b]	98	131	319	369	2.227	−3104.700
B3LYP [74]	99	133	320	370	2.230	−3104.701
UHF [74]	103	147	334	386	2.258	−3100.536

[a] Pseudopotential calculations
[b] All-electron calculations

calculations listed in table 5.1, the underestimation of vibrational frequencies is severe in the BP86 functional method. This can be explained by the fact that with the B3LYP hybrid functional, the exchange energy is treated correctly. It should be noted that the anion $[FeCl_4]^-$ is slightly distorted from the T_d symmetry (see 1st row in table 5.1), which leads to the splitting of the higher-frequency stretching band near 383 cm^{-1} [71]. The all-electron Hartree-Fock treatment gives a better agreement for some of the frequencies (not for all), but it is more costly for large complexes. Therefore, the pseudopotential method is adopted for the rest of all model complexes and isomers.

The Raman spectrum at room temperature (RT) is shown in fig. 5.3 together with the ^{57}Fe VDOS extracted from the NIS spectrum at 70 K of the model complex $[N(CH_3)_4]^+[FeCl_4]^-$. In the VDOS spectrum there are three dominating peaks at 50,

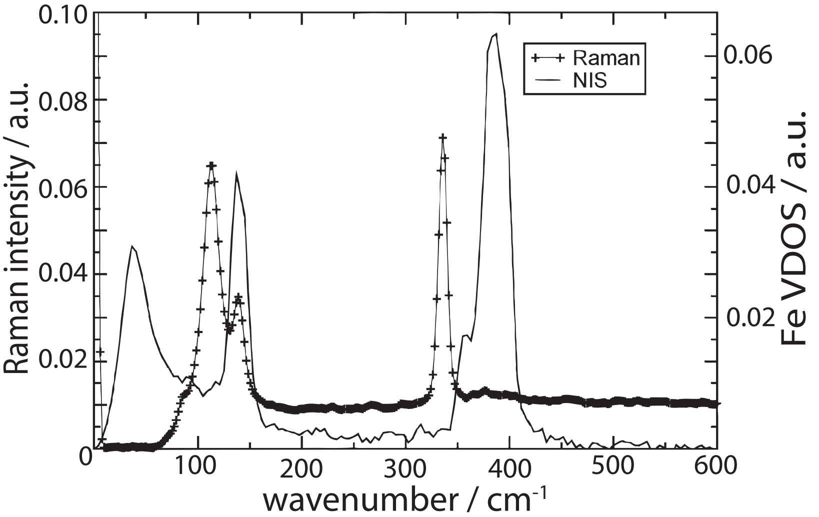

Figure 5.3: Comparison of Raman and NIS spectra for solid $[N(CH_3)_4][FeCl_4]$. The Raman data were obtained at RT and the NIS at 70 K.

138 and 383 cm^{-1}. The peak at 50 cm^{-1} or the region below 90 cm^{-1} is due to lattice modes, i.e. the three acoustic (also translational) and rotational vibrational modes. In a local T_d symmetry of an isolated anion $[FeCl_4]^-$ there are nine fundamental normal modes of vibration: the symmetric stretch A_1 (ν_s), the deformation E (δ_d, doubly degenerate), the stretching T_2 (ν_d, triply degenerate) and the deformation T_2 (δ_d, triply degenerate) [75]. The modes A_1 and E are inactive to NIS as the motion of the Fe atom is excluded by symmetry. Therefore the features of the NIS have to be assigned to two T_2 modes. By comparison of the theoretically calculated frequency with NIS and Raman analysis the peak at 138 cm^{-1} is assigned to T_2 (δ_d) involving mostly Cl−Fe−Cl bending. The peak at 113 cm^{-1} in the Raman spectrum and its absence in NIS is exclusively assigned to E (refer to table 1) since there is no Fe motion in the E mode of vibration. The largest peak at 383 cm^{-1} is primarily a Fe−Cl stretching motion, i.e. a T_2 mode. Although this peak is Raman active, it is seen only as a very tiny peak in the Raman spectrum (see fig. 5.3).

In NIS, the band intensity is directly proportional to the mean square displacement of the resonant nucleus, ^{57}Fe, in the respective mode, leading to exclusive observation of the T_2 modes. Therefore, the stretching mode Fe−Cl has the largest intensity compared to the other peak at 138 cm^{-1}. Thus, if different isomers of a complex possess different symmetries, this should lead to significant differences in their NIS spectra.

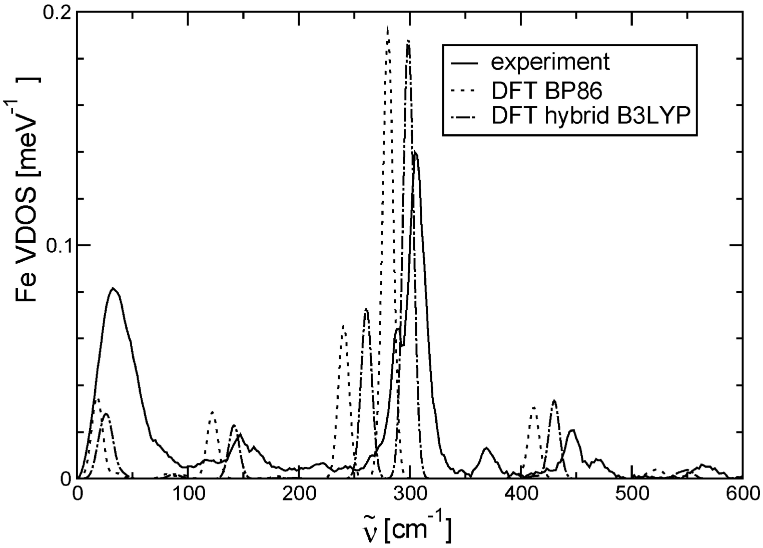

Figure 5.4: Experimental (at 20 K) and DFT predicted VDOS of solid $Fe(acac)_3$.

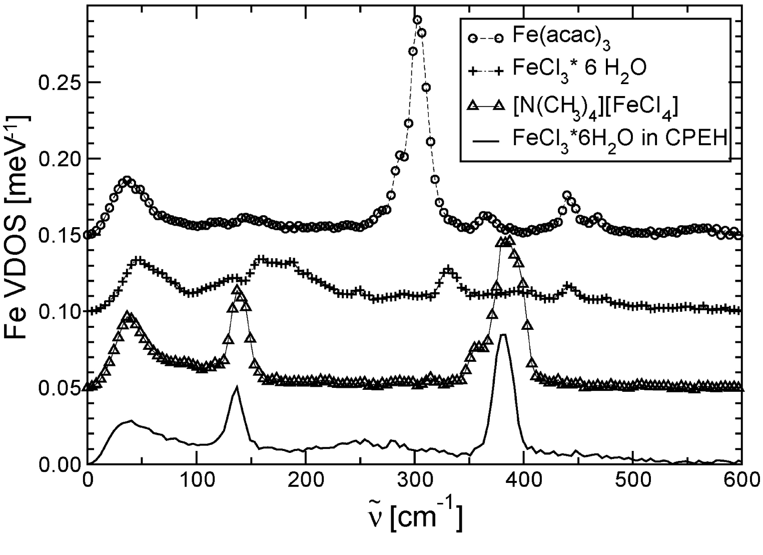

Figure 5.5: Experimental VDOS of the three solid reference compounds $Fe(acac)_3$, $FeCl_3 \cdot 6H_2O$ and $[N(CH_3)_4][FeCl_4]$, together with the spectrum of $FeCl_3 \cdot 6H_2O$ in CPEH at 70 K. The upper curves are offset for clarity.

The VDOS of the model complex $Fe(acac)_3$ from NIS and the DFT calculated spectrum are shown in fig. 5.4. As discussed before, the faster Becke-Perdew DFT calculations tend to underestimate the experimentally observed vibrational frequencies by 20 cm^{-1}, whereas the B3LYP method gives a better agreement with the experiment. NIS gives access to low-frequency modes, some of which were

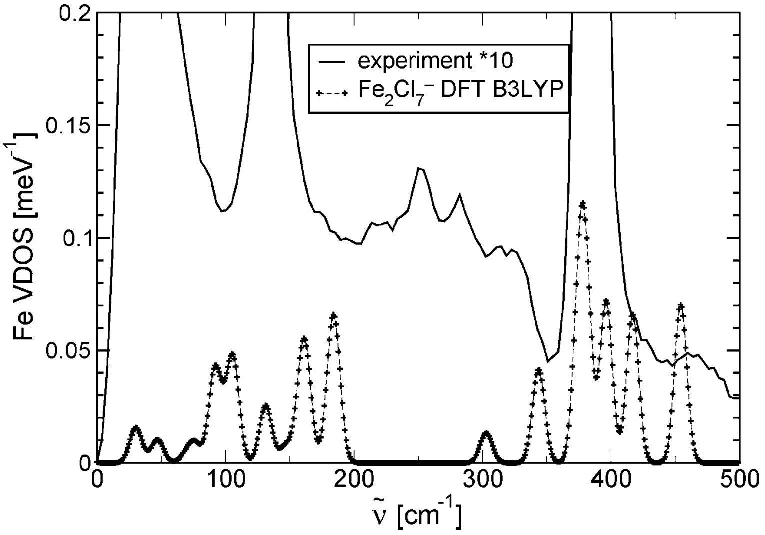

Figure 5.6: Experimental VDOS of a frozen solution of $FeCl_3 \cdot 6H_2O$ in CPEH at 20 K and the theoretical VDOS of $Fe_2Cl_7{}^-$ (B3LYP).

not visible in a previous far-infrared (FIR) study, such as the 28 and 141 cm^{-1} skeletal modes, where the acac$^-$ units move as a whole with respect to the central Fe atom [76]. Moreover, the DFT calculations were carried out on single molecules and hence neglect intermolecular interactions in the solid. The dominating large peak at 303.5 cm^{-1} can be compared to the Fe—O stretching vibration that involves a large displacement of the Fe atom (see fig. 5.4). This is close to the previously reported values of 300.5 or 298 cm^{-1} [76, 77]. The tiny peaks around 450 cm^{-1}, especially the 441.7 cm^{-1} peak is also a Fe—O stretching vibration but coupled with a C—CH_3 bending mode [77]. Fig. 5.5 depicts the VDOS extracted from the NIS spectrum of the model complexes $FeCl_3 \cdot 6H_2O$, $Fe(acac)_3$ and $[N(CH_3)_4]^+[FeCl_4]^-$, together with the shock frozen sample **4**, i.e. $FeCl_3 \cdot 6H_2O$ in CPEH at 70 K. By comparison, it is obvious that the anion species $[FeCl_4]^-$ is present in $[N(CH_3)_4]^+[FeCl_4]^-$ and in sample **4** as indicated by the two strong peaks at 138 and 383 cm^{-1}, which are primarily due to Cl—Fe—Cl bending and Fe—Cl stretching, respectively. Moreover, this confirms the previous Raman findings that $[FeCl_4]^-$ is present in species **4**, but in addition, we see a number of vibrational bands in the 200–300 cm^{-1} range (see fig. 5.6), which may be compared to the wavenumber (290 cm^{-1}) of the Fe—O stretching vibration in $Fe(acac)_3$ [76].

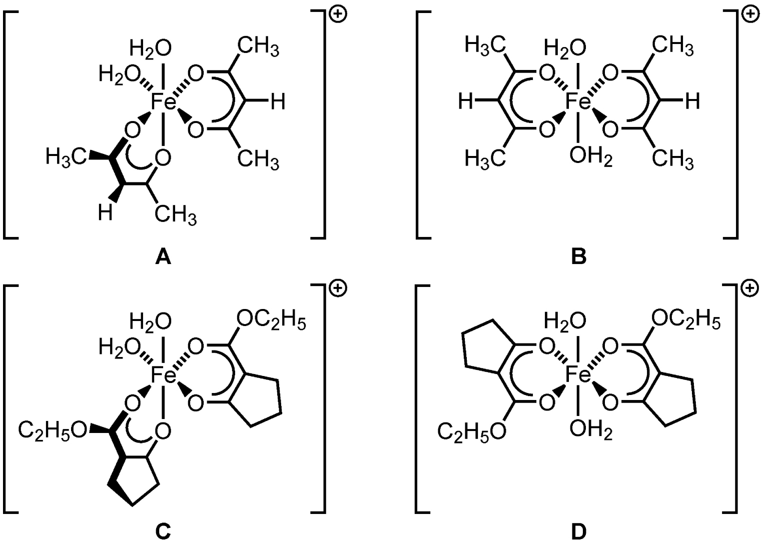

Figure 5.7: Complexes treated by DFT calculations. The geometries optimized using the BP86 functional are shown; however, the geometries as obtained by B3LYP are almost identical.

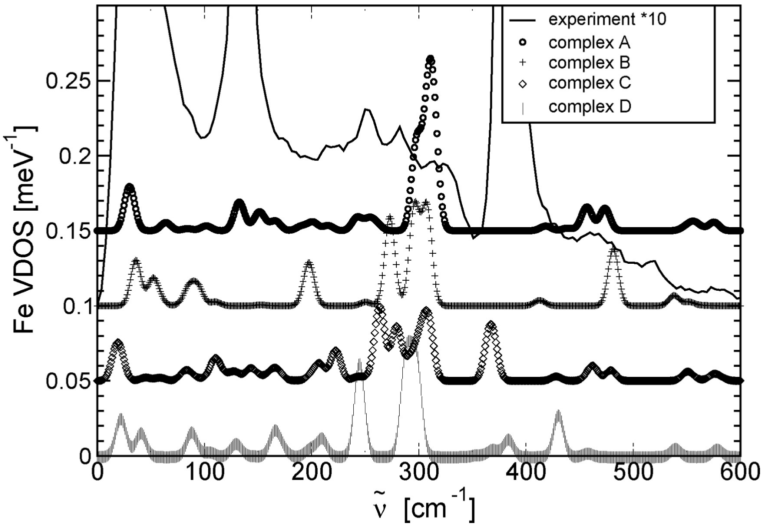

Figure 5.8: Experimental VDOS of the frozen reaction mixture of $FeCl_3 \cdot 6H_2O$ in CPEH and the DFT calculations of the species depicted in fig. 5.7. The upper curve is offset for clarity of representation.

To improve this finding, sample **4** was prepared again and measured with much better statistics (more scans) and at lower temperature (20 K), so as to minimize multiphonon contributions. The experimental curve, together with the calculated VDOS of $Fe_2Cl_7^-$, is shown in fig. 5.6. Obviously, the species $Fe_2Cl_7^-$ is not present in considerable amounts, as shown by the presence of the peaks in the range ∼150–200 cm^{-1}, which are not seen in the experimental VDOS. For the theoretical anaylsis, two isomers of $Fe(acac)_2 \cdot 2H_2O$ (facial A and meridional B) and two isomers of $FeC_{16}H_{26}O_8$ (facial C and meridional D), were generated using MOLDEN [78]. The DFT optimized structures of these four model complexes are shown fig. 5.7. The experimental VDOS from NIS analysis together with the theoretically predicted spectra are depicted in fig. 5.8. It is immediately obvious that the simplified complex (A or B), where $acac^-$ replaces the β-diketo species, gives no good description of the experimental data. The stiffness introduced by the existence of the cyclopentane ring has a decisive influence on the normal modes around the Fe atom. Moreover, the agreement of the DFT calculation and the experimental data is better for the facial isomer (C) than that of the meridional one (D) (note the relative intensity of the peaks between 200–350 cm^{-1} for C and compare with A, B and D). Also for both isomers (A vs B and C vs D), the facial isomers are about 8×10^{-3} E_h or 21 kJ mol^{-1} lower in energy than the meridional ones, which is in accord with earlier findings [55] (see table 5.1). Thus the species C might prevail in solution and maybe also be the complex via which the further reaction proceeds [79].

5.6 Conclusions

For the first time the NIS technique was performed on frozen solutions of homogeneous reactions catalyzed by transition-metal complexes. The result obtained from NIS is compared with the theoretically predicted vibrational spectra based on the normal mode analysis via quantum mechanical calculations. Based on NIS and DFT calculations, the intermediate formed during the first step of the reaction, i.e. when $FeCl_3 \cdot 6H_2O$ dissolved in CPEH, is an octahedral complex (isomer C) described as bis(diketonato)−iron(III) unit coordinated with two water molecules. The results for the anion $[FeCl_4]^-$ are in good aggrement with previous literature values. Moreover, NIS together with Raman, UV/vis and DFT studies provides complementary information. Owing to the special NIS selection rules, isomers that are otherwise very similar may be distinguished when experimental statistics are sufficiently good.

Chapter 6

Gif reaction of a Fe complex as studied by Mössbauer spectroscopy

6.1 Introduction

The selective oxidation of organic molecules forms part of many reactions important in biochemistry and is highly useful in chemical industry. A widely studied example is the biochemical role of iron in cytochrome P450 that catalyses the oxidation of organic molecules [80]. In chemical industry, the selective oxidation is considered as the most favored process for converting petroleum-based raw materials to useful chemicals such as alcohols, carbonyl compounds and epoxides [81]. There are various ways to catalyze such reactions in the presence of naturally occuring molecular oxygen. Using a metal catalyst is notable for the following reasons: 1. the reaction takes place at ambient operating conditions and 2. in an environmentally friendly manner. The central metal ion is often chosen to be iron because of its importance in many biological processes. Moreover, iron is cheap and known for its abundance in the geosphere. It is known that Gif catalysis is one of the most successful and well-known ways to catalyze the oxidation of organic substrates to ketones [82]. In this chapter we describe the study of a new Gif-type catalytic system prepared within a cooperation with the Institute of Organic Chemistry by ^{57}Fe transmission Mössbauer spectroscopy. Liquid samples were converted into frozen solutions, with the aim to identify the intermediate species that are formed in the reaction. The catalyst used in the present work is a trinuclear oxobridged iron complex [83].

6.2 The Gif reaction

The Gif reaction is the oxidation of an organic molecule in the presence of molecular oxygen by a system comprising an iron catalyst, metallic zinc, pyridine and acetic acid. There are different classes of Gif reactions based on the reagents used. The reaction studied in this chapter is similar to the Gif^{IV} system where the catalyst is usually a trinuclear mixed valence iron compound [82, 84]. In our case it is not a mixed valence iron complex but a structurally similar trinuclear Fe(III) compound. This reaction is shown in fig. 6.1 (bottom) and converts a cyclohexene (substrate) to the corresponding ketone. In a Gif reaction, pyridine is used as an organic base, which plays an important role for obtaining good turnover numbers.

When the trinuclear catalyst is dissolved in pyridine and/or acetic acid, a monomeric ferric iron species is formed (see section 6.4.2). On adding metallic zinc, which is a reducing agent, the ferric iron species is reduced to a ferrous iron species. This ferrous species might be a possible intermediate, which is responsible for the initial step of the carbon-hydrogen activation. In this chapter, all the Mössbauer spectra obtained from frozen solution samples and trinuclear iron compounds will be discussed. The

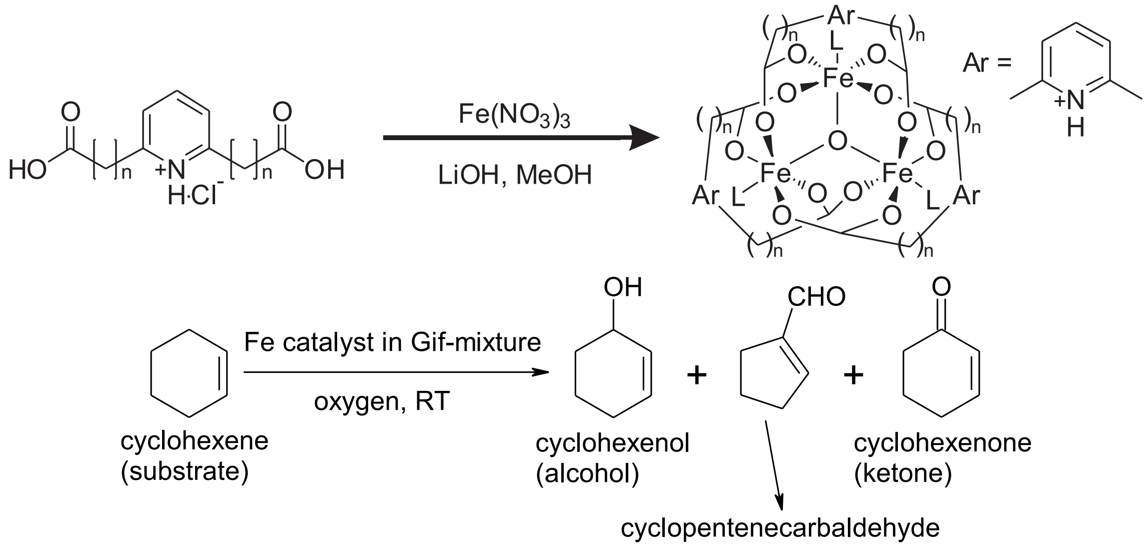
HO
OH
+N
H·Cl⁻
n
Fe(NO3)3
LiOH, MeOH
Ar
L
Fe
Ar =
+N
H
Fe catalyst in Gif-mixture
oxygen, RT
cyclohexene
(substrate)
OH
cyclohexenol
(alcohol)
CHO
cyclopentenecarbaldehyde
O
cyclohexenone
(ketone)

Figure 6.1: Top: Preparation of trinuclear iron complex ($n = 2$). Bottom: Catalytic oxidation of cyclohexene under Gif type conditions. The Gif mixture is the mixture of pyridine, acetic acid and zinc.

structural details of the ferric and ferrous iron species that are formed during reaction will be studied in the next chapter.

6.3 Sample preparation and holder

The solid trinuclear complex is prepared by the reaction of the deprotonated ligand with anhydrous iron nitrate ($Fe(NO_3)_3$) and subsequent removal of the solvent. For more details on the preparation of ligands and complexes, see [83, 85]. In order to study the reaction kinetics of the Gif reaction, various liquid samples were prepared by dissolving the iron catalyst in different combinations of reagents (see table 6.1), which are required for the reaction and transferring a drop of sample liquid into the sample holder by a 1 ml syringe. From experience we learnt that a small drop is better than taking one full drop. This can be done easily by carefully controlling the

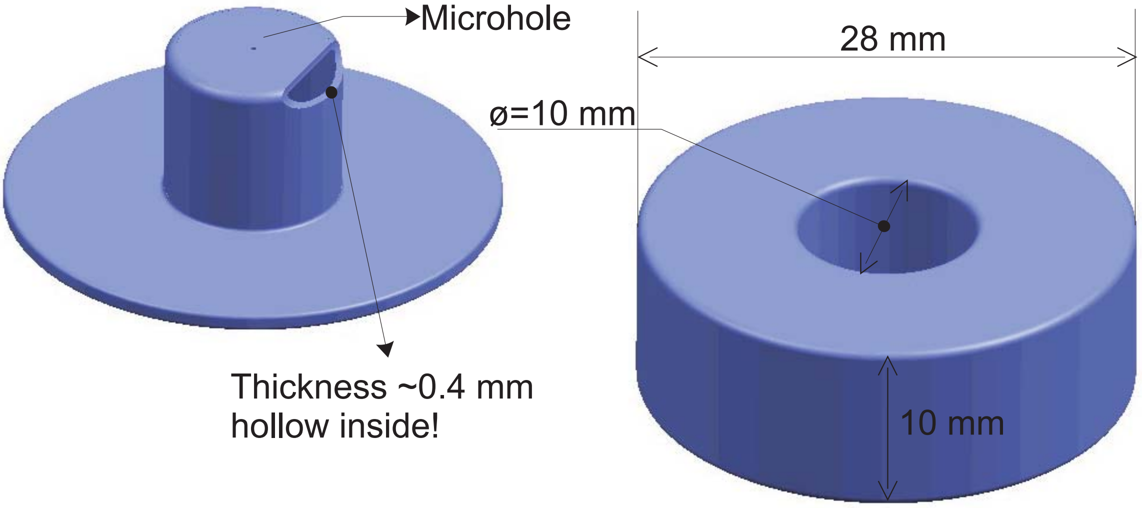

Figure 6.2: Schematic drawing of a teflon sample holder used for low-temperature Mössbauer measurements. The sample liquid is taken in a syringe and transferred to the bottom part (right). Then the top part (left) is inserted onto the bottom part before freezing. The top part, which also avoids the movement of the frozen liquid after freezing, has a microhole so as to facilitate the escape of air while inserting. The top part shown here contains a small cut for better understanding of geometry, however, in real sample holders there is no such cut.

Table 6.1: Sample numbering and preparation scheme.

Sample No.	Compounds	Remarks
1	trinuclear Fe catalyst	solid/powder
2	31.8 mg of sample 1 dissolved in 0.9 ml of pyridine	prepared in open atmosphere and then frozen for measurement
3	0.07 ml of acetic acid added to sample 2	prepared in open atmosphere and then frozen for measurement
4	61 mg of Zn powder added to sample 3	prepared and frozen under inert gas
5	sample 4 flushed with O_2 gas	prepared by taking a small amount from the remainder left after preparing sample 4
6	0.05 ml cyclohexene added to sample 4	prepared and frozen under N_2 gas
7	reaction after 1 min	these three samples were prepared according to the reaction shown in fig 6.1 in a single reaction
8	reaction after 5 min	
9	reaction after 30 min	

piston of the syringe, i.e. the size of the drop formed at the tip of the needle can be approximately controlled by the piston of the syringe. When a very small drop is formed at the tip of the needle, this drop can be transferred easily to the sample holder by just touching the sample holder with the needle, on the tip of which the small drop is hanging.

The sample holders for Mössbauer measurements were made of teflon, for further details see fig. 6.2. Liquid samples, which are sensitive to air, were prepared inside a glove bag filled with inert gas and then transferred to the sample holder using a syringe. The holder with liquid is then dropped into liquid nitrogen. The frozen samples were measured at 4.2 K in a bath cryostat, using a gas proportional detector in transmission geometry and a ^{57}Co source in a rhodium matrix. In these measurements both the source and the sample were maintained at 4.2 K and the source follows a sinusoidal motion.

After preparing the first liquid sample (2 in table 6.1), subsequent liquid samples were obtained from the remainder of this first liquid sample as shown in table 6.1. In order to study the reaction kinetics, three samples (7, 8 and 9 in table 6.1) were prepared from a single reaction mixture by taking a small amount (less than a drop, see section 6.3 for details) of sample liquid after the start of reaction. These were taken after 1, 5 and 30 min and frozen quickly, i.e. to stop the reaction by immersing into liquid nitrogen.

6.4 Results and discussion

6.4.1 Trinuclear iron catalyst

On the basis of the analytical data obtained from electrospray ionization mass spectrometry, elemental analysis and X-ray absorption spectroscopy, the complex contains a central trinuclear iron unit $Fe_3(\mu_3\text{-}O)$ with three pyridine-2,6-dicarboxylate ligands as shown in fig. 6.1 (top) [83]. The Mössbauer spectra of the catalyst precursor trinuclear oxobridged iron complex (see 1 in table 6.2) are shown in fig. 6.3. At room temperature (RT) the spectrum displays a doublet and at 4.2 K a doublet and a broad singlet. The isomer shift $\delta = 0.410$ mm s^{-1} and quadrupole splitting $\Delta E_\mathrm{Q} = 0.574$ mm s^{-1} obtained at RT are consistent with a typical high-spin (HS) Fe(III) species [13]. The line width Γ of 0.41 mm s^{-1} is larger than the instrument resolution of $\sim$0.26 mm s^{-1}, hence, the quadrupole doublet may contain overlapping doublets with different ΔE_Q accounting for the three Fe ions. At 4.2 K, δ slightly increases, which is probably due to the second-order Doppler effect. On comparing the line width obtained from the RT and 4.2 K spectra, Γ increases from 0.41 to 0.60 mm s^{-1}, this increase in line width on decreasing temperature is mainly due to the onset of electronic relaxation. Moreover, for this reason, at 4.2 K the spectrum shows a broad shoulder see fig. 6.3 (bottom). The absence of the broad singlet in the RT spectrum and presence of it in the 4.2 K spectrum is again due to electronic spin relaxation.

It is widely known, according to the Heisenberg, Dirac and van Vleck formalism, that at very low temperatures (4.2 K) the Fe_3O triangle (oxygen in the centroid of the triangle) significantly distorted leading to an isosceles structure [86, 87]. Therefore, two Fe atoms in the Fe_3O triangle which has a shorter Fe−Fe bond are magnetically

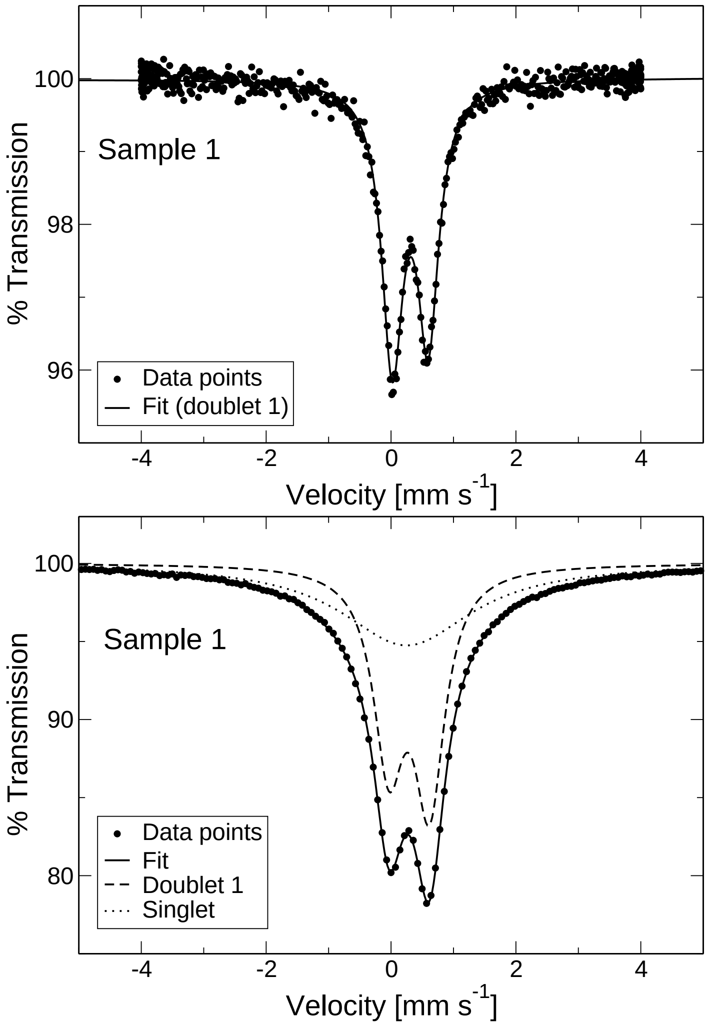

Figure 6.3: Mössbauer spectrum of the trinuclear iron catalyst at RT (top) and 4.2 K (bottom).

coupled to form a diamagnetic pair, i.e. $S = 0$. As a consequence the third Fe is magnetically isolated and this HS Fe accounts for the ground-state spin [86, 88]. Presumably in our complex at 4.2 K this HS Fe causes a part of the electronic spin relaxation together with increased line width, hence, a broad singlet is included in the fitting routine, see table 6.2 for details.

6.4.2 Frozen solutions

The spectra of the iron catalyst precursor in pyridine and after addition of acetic acid are shown in fig. 6.4. These spectra show very complex non-Lorentzian line

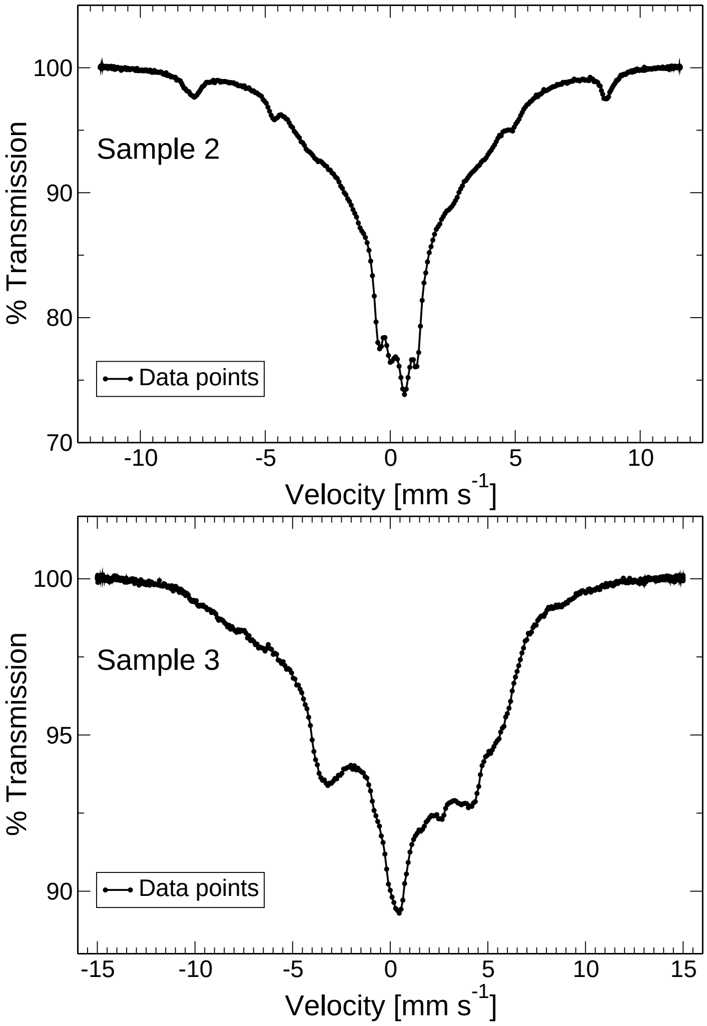

Figure 6.4: Mössbauer spectrum of catalyst in pyridine (sample 2) and in a mixture of pyridine and acetic acid (sample 3) at 4.2 K.

shapes, which are primarily due to relaxation effects. It is known that these unusual spectral line shapes are widely observed in HS Fe(III) paramagnetic ions [89, 90]. The relaxation is an electronic spin-flip which results in a reversal of the internal magnetic hyperfine field (in zero applied field). In other words, the direction of the internal magnetic field is not fixed, but fluctuates with a time constant because of paramagnetic relaxation process. The relaxation effects on Mössbauer line shape depend on the relative time scales of measurement and the relaxation mechanism itself. The three known time scales are: 1. the life time τ of the Mössbauer event, i.e. life time of the Mössbauer nucleus, 2. the nuclear Larmor precession time τ_{L} and 3. the electronic relaxation time τ_{e}. The first time scale, which is a fixed quantity for a given Mössbauer nucleus, is the limiting factor of the measurement technique for the observation of a magnetic split spectrum. The first excited state 14.4 keV of the ^{57}Fe has a mean life time of 1.41×10^{-7} s, which is often compared to the other two time scales for understanding the relaxation phenomenon. Generally hyperfine magnetic fields are detectable when $\tau_\mathrm{e} > \tau \geq \tau_\mathrm{L}$. For iron oxides the internal magnetic field ranges from 35–60 T, which gives τ_L of the order of $\sim 10^{-8}$ s, hence, hyperfine fields can be obtained.

The second time scale is the nuclear Larmor precession time, which is generally defined as the time due to precession of the nuclear magnetic moments of the nucleus in a magnetic field. The third important time scale is the electronic relaxation time, which is associated with the time dependent fluctuations of the electron spin. In order to observe a magnetic hyperfine field, the nuclear Larmor precession time should be small compared to electronic relaxation time, i.e. the electronic relaxation time should be constant for at least one Larmor precession period ($\tau_\mathrm{e} \gg \tau_\mathrm{L}$). This is often called slow relaxation limit, where the hyperfine field is static during a single Larmor precession period. The line width is influenced by the relaxation as long as the relaxation times are short compared to τ (Γ will increase when $\tau_\mathrm{e} \approx \tau$). In the case when $\tau_\mathrm{e} \ll \tau_\mathrm{L}$, i.e. in the fast relaxation limit, the spectrum collapses to one or two lines usually with sharp Lorentzian profiles, the line width of which decreases with decreasing relaxation time. The nucleus experiences a time-averaged hyperfine field. The magnetic hyperfine field tends to zero as τ_e decreases and it is less than the value obtained for a static field as the interaction will have changed many times during a single Larmor precession period. In paramagnetic Fe(III) ions, when the Larmor precession time is comparable to the electronic relaxation time ($\tau_\mathrm{e} \approx \tau_\mathrm{L}$), complex broad non-Lorentzian line shapes as in fig. 6.4 are obtained [89]. In this intermediate range, the time-dependent hyperfine interactions lead to a spread in line widths and the overall spectrum will be broadened. As the spectrum shown in fig. 6.4 (top) displays complicated line features, only a rough determination of the τ_L can be made as shown below. The nuclear Larmor precession time is given by [89]:

$$\tau_\mathrm{L} = (\omega_\mathrm{L})^{-1} = \frac{2\pi\hbar}{g\,\mu_\mathrm{N}\,H}, \tag{6.1}$$

where $g(=g_\mathrm{e}$ or $g_\mathrm{g})$ is the gyromagnetic factor. The subscripts e and g stands for excited and ground state, respectively. $\hbar = h/(2\pi)$, μ_N is the nuclear magneton and H is the hyperfine magnetic field, which is equivalent to the line separation of outer lines.

Table 6.2: Mössbauer parameters of all samples at 4.2 K unless specified obtained from fitting using Lorentzian line shapes. The numerical values enclosed in parentheses are isomer shifts δ relative to ^{57}Co source at 4.2 K [91]. The δ, quadrupole splitting ΔE_Q and full width at half maximum Γ are given in mm s^{-1}. All samples are numbered in the same scheme as shown in table 6.1.

	Sample	δ	ΔE_Q	Γ	Relative area
1	at RT	0.410 ± 0.002 (0.308)	0.574 ± 0.003	0.41 ± 0.00	1.0
		0.525 ± 0.001 (0.290)	0.652 ± 0.001	0.60 ± 0.00	0.5
	(Singlet)	0.485 ± 0.005 (0.250)	–	2.56 ± 0.05	0.5
2		–	–	–	–
3		–	–	–	–
4	(Doublet 2)	1.184 ± 0.002 (0.949)	3.392 ± 0.003	0.26 ± 0.00	0.8
5	(Doublet 1)	0.540 ± 0.005 (0.305)	1.040 ± 0.009	0.30 ± 0.01	0.5
	(Doublet 2)	1.182 ± 0.007 (0.947)	3.287 ± 0.013	0.31 ± 0.02	0.4
6	(Doublet 1)	0.256 ± 0.028 (0.021)	0.897 ± 0.053	0.37 ± 0.07	0.2
	(Doublet 2)	1.185 ± 0.003 (0.950)	3.372 ± 0.007	0.28 ± 0.01	0.7
7	(Doublet 2)	1.208 ± 0.002 (0.973)	3.217 ± 0.005	0.27 ± 0.01	0.8
8	(Doublet 1)	0.524 ± 0.005 (0.289)	1.008 ± 0.009	0.36 ± 0.02	0.4
	(Doublet 2)	1.187 ± 0.003 (0.952)	3.091 ± 0.006	0.35 ± 0.01	0.5
9	(Doublet 1)	0.539 ± 0.002 (0.304)	1.052 ± 0.004	0.24 ± 0.01	0.5
	(Doublet 2)	1.197 ± 0.005 (0.962)	3.203 ± 0.011	0.32 ± 0.02	0.3
	(Doublet 3)	1.268 ± 0.021 (1.033)	1.405 ± 0.042	0.45 ± 0.05	0.1

From fig. 6.4 (top), the separation between the outer lines is ~16.6 mm s^{-1}, which is equivalent to a hyperfine magnetic field of 51.7 T. According to formula (6.1), for the ground state of the nucleus, i.e. taking $g_\mathrm{g} = 0.0906/(1/2)$ one obtains $\tau_\mathrm{L} = 1.4 \times 10^{-8}$ s (for the excited nuclear state $\tau_\mathrm{L} = 2.5 \times 10^{-8}$ s).

Moreover, there are three different Larmor precession times corresponding to the different transitions between the excited and ground state of the nucleus [92]. The three transitions that are allowed by magnetic dipole transitions (M1) are $\pm 3/2 \leftrightarrow \pm 1/2$ (outer lines), $\pm 1/2 \leftrightarrow \pm 1/2$ and $\pm 1/2 \leftrightarrow \mp 1/2$ (innermost lines). These three sets of transitions make six lines, i.e. the hyperfine pattern as seen in fig. 3.4 of chapter 3. According to formula (6.1), we see that the separation between the spectral lines is inversely proportional to τ_L. The separation of the outer lines ($\pm 3/2 \leftrightarrow \pm 1/2$ transition of a magnetic hyperfine pattern) is larger, hence, has a smaller τ_L when compared to the separation of the inner and innermost lines. In other words, the inner lines will collapse at a smaller relaxation frequency (i.e. large τ_L) than the outer lines causing the inner lines of the sextet to broaden and disappear before the outer ones [89]. Therefore, the spectrum shown in fig. 6.4 suffers from paramagnetic relaxation and $\tau_\mathrm{e} \approx \tau_\mathrm{L}$ (electronic relaxation time is in the order of nuclear Larmor precession time). On adding acetic acid, these features are more pronounced and even the outer lines are no more visible.

From the above discussion based on relaxation phenomena we can conclude that paramagnetic relaxation dominates in the Fe(III) ions (in fig. 6.4), that are present in the mixture. For this reason, due to paramagnetic relaxation processes in samples 2 and 3 we suggest that when adding solvent, which is pyridine and/or acetic acid, to the catalyst precursor shows that the solvent enters the ligand sphere of the Fe and alters the electronic structure including the Fe−Fe spin coupling in the trimer and is therefore a first hint of breaking into monomers, which will later be confirmed by NIS and density functional theory (DFT) calculations. For details, see chapter 7. Hence, it is suggested that the trinuclear iron catalyst breaks up into monomers when dissolved in a mixture of pyridine and acetic acid, and that these monomers are responsible for the initial step for the carbon-hydrogen activation of the Gif reaction. We suggest that this possible monomer is the intermediate HS Fe(III) species.

The spectrum of the trinuclear iron compound in a mixture of pyridine, acetic acid and zinc under inert atmosphere (sample 4) is shown in fig. 6.5 (top). The spectrum (active catalyst under inert gas) displays a doublet at $\delta = 1.184$ mm s^{-1} and $\Delta E_\mathrm{Q} = 3.392$ mm s^{-1}, which is typical for HS Fe(II) ($S = 2$) species. The Fe/Be doublet shown in some figures is due to a small amount (10–20%) of iron present in the beryllium window of the detector. The isomer shift, quadrupole splitting and line width for this doublet are fixed in the fitting routine and are not shown in table 6.2 for clarity. The relative area of this doublet is ~0.1 except for sample 4 where it is ~0.2.

Another frozen sample, sample 5, was prepared after flushing the solution of trinuclear catalyst in a mixture of pyridine, acetic acid and zinc with oxygen gas for a few

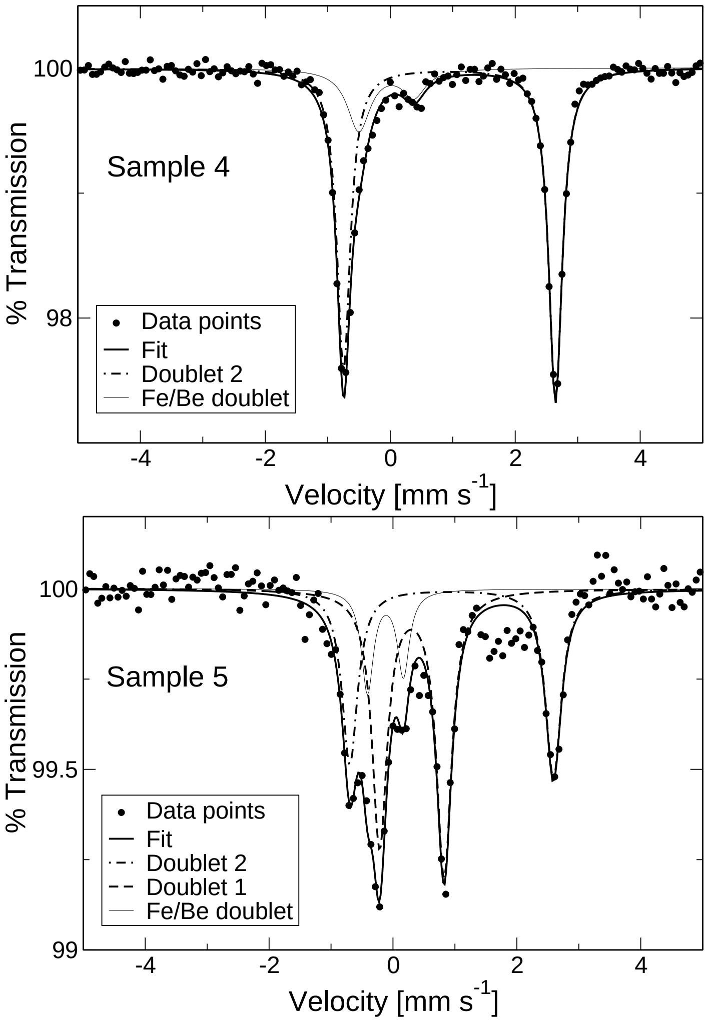

Figure 6.5: Mössbauer spectrum of the active catalyst, i.e. the iron catalyst in a mixture of pyridine, acetic acid and zinc under inert (sample 4) and open atmosphere (sample 5) at 4.2 K.

minutes. The spectrum shown in fig. 6.5 (bottom) displays two quadrupole doublets. The Mössbauer parameters of one doublet are almost the same as in sample 4, see the parameters of doublet 2 of samples 4 and 5 in table 6.2. Hence it is very clear that both samples 4 and 5 contain the same Fe(II) HS ($S = 2$) species. But in addition to this doublet, a new doublet at $\delta = 0.540$ mm s^{-1} and $\Delta E_\mathrm{Q} = 1.040$ mm s^{-1} is formed. These parameters are consistent with a typical Fe(III) HS electronic configuration. The isomer shift is almost the same as found for the trinuclear iron compound, but the quadrupole splitting differs a lot. For details compare ΔE_Q of the doublet in sample 1 with the doublet 1 in sample 5. The reason might be that the iron catalyst

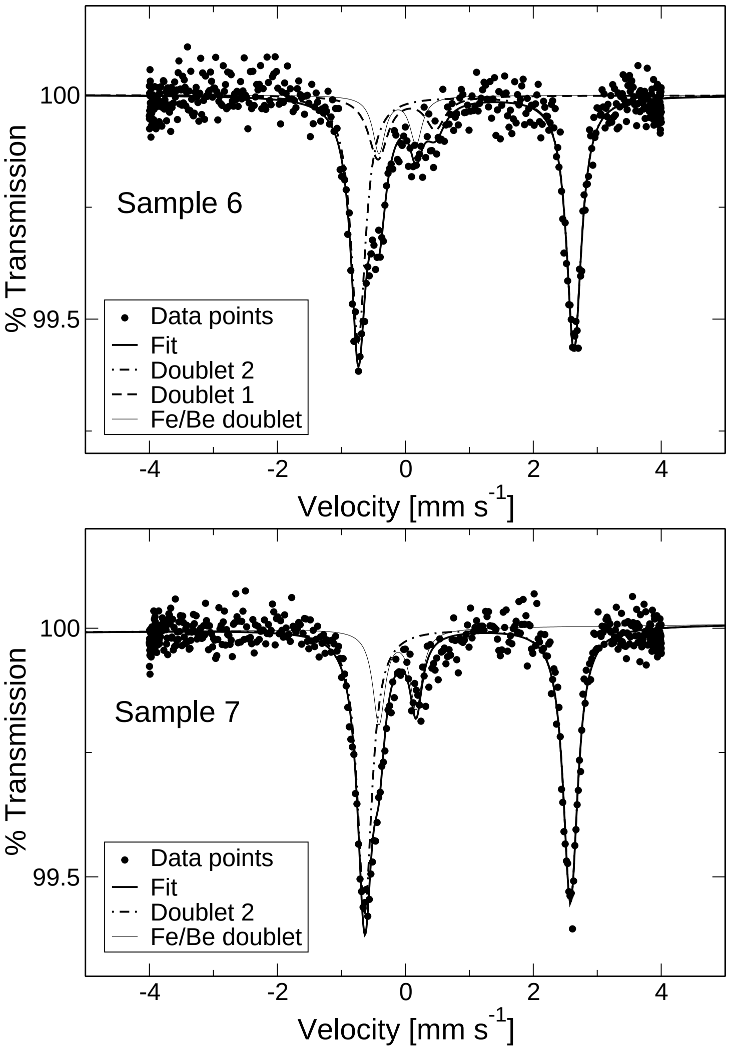

Figure 6.6: Mössbauer spectrum of the active catalyst with cyclohexene prepared under inert atmosphere (sample 6) and reaction after 1 min (sample 7) at 4.2 K. The doublet 1 in sample 6 is almost buried in noise and has large fit error (standard deviation) for all Mössbauer parameters and therefore this feature is not significant for our analysis.

is partially distorted, i.e. the octahedral coordination of the iron atom in the trinuclear iron compound is slightly distorted from octahedral symmetry. However, the species HS Fe(II) is not completely reduced to the newly formed Fe(III) species with the larger ΔE_Q. The area of the doublet 1, i.e. Fe(III), contributes 50% to the whole spectral area (assuming identical f_LM factor) and therefore it slightly dominates over the Fe(II) species.

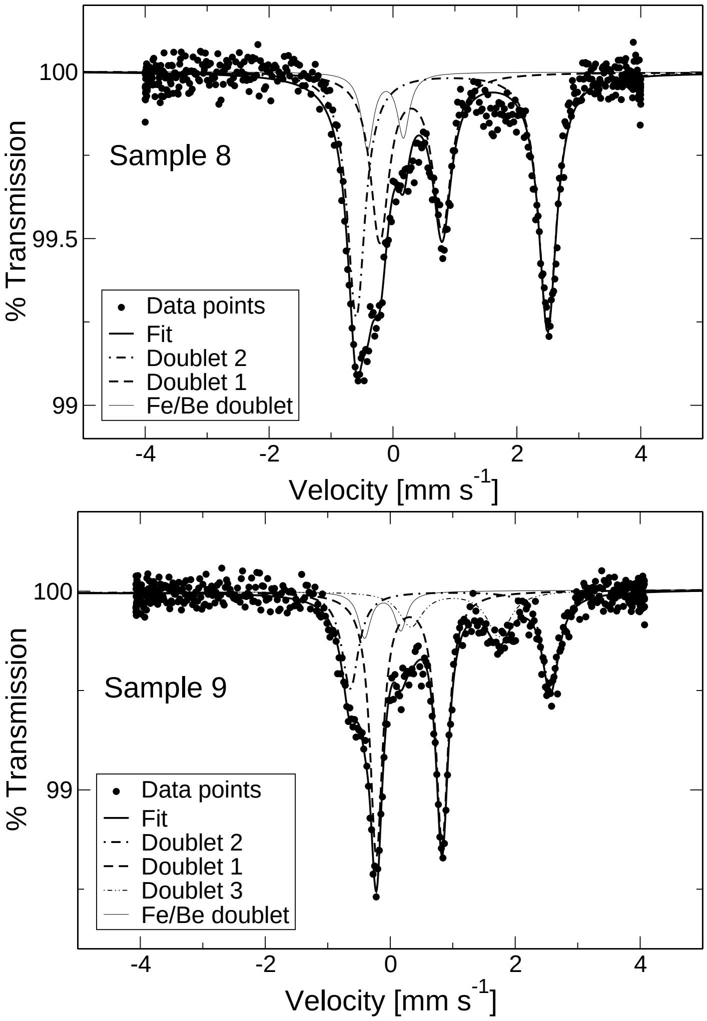

Figure 6.7: Mössbauer spectrum of the reaction after 5 min (sample 8) and after 30 min (sample 9) at 4.2 K.

In order to find the influence of the substrate (cyclohexene) before the start of the Gif reaction, a sample is prepared with all Gif reagents under inert atmosphere (sample 6). This sample, which is just before the start of the reaction, i.e. before flushing oxygen gas can be thought of a Gif reaction at zero time. The spectrum of this sample is shown in fig. 6.6 (top), which exhibits almost the same Fe(II) Mössbauer parameters as found in the sample 4 under inert gas, for details compare the parameters of doublet 2 in sample 4 with sample 6 in table 6.2.

The Mössbauer spectra of the Gif reaction mixture shown in fig. 6.1 were measured at various time intervals: 1, 5 and 30 min. These three are shown in figs. 6.6 (bottom)

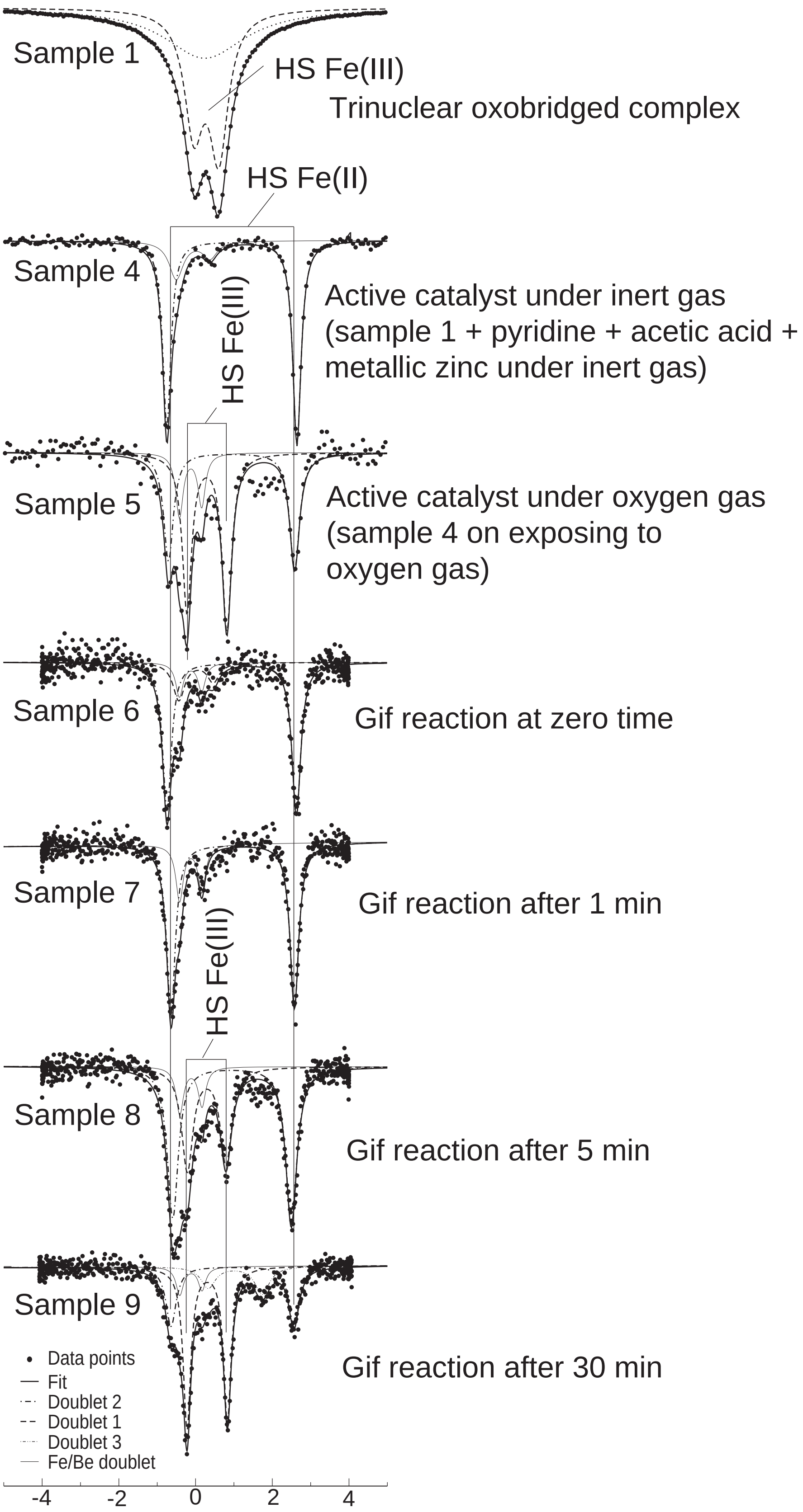

Figure 6.8: Overview of Mössbauer spectra of samples 1 and 4–9.

and 6.7. The spectrum after 1 min shows the presence of HS Fe(II), with similar Mössbauer parameters to that of Fe(II) present in all other samples (doublet 2 of samples 4, 5, 6, 7, 8 and 9, see fig. 6.8). After 5 min, due to oxidation Fe(III) was formed (refer to fig. 6.7, top), as indicated by this inner doublet 1 in addition to the HS Fe(II). The quadrupole splitting of the doublet 1 in sample 8 is larger than that of the iron catalyst and identical to the one obtained on merely flushing with oxygen (sample 5). After 30 min, the intensity of the HS Fe(III) doublet is more pronounced than after 5 min, but still some Fe(II) species is present, see fig. 6.7 (bottom). Before the start of the Gif reaction, the spectrum of sample 6 displays only one significant quadrupole doublet, which is typical for HS Fe(II) ($S = 2$) species. The same species is present in samples 4 and 5. In addition to this doublet, sample 5, which is frozen after exposing to oxygen, displays the presence of HS Fe(III) ($S = 5/2$) species, which is also present in reaction samples (samples 8 and 9), see fig. 6.8. Therefore, this HS Fe(II) ($S = 2$) is the active catalyst that initiates the carbon-hydrogen activation of the Gif reaction. In samples 4 and 6 there is only one significant doublet due to active catalyst. Samples 5, 8 and 9 contain both the active catalyst as well the newly formed HS Fe(III) ($S = 5/2$) species. Moreover, investigation by NIS on samples 4 and 6 shows almost identical spectral features which will be discussed in the next chapter.

6.5 Conclusions

The Gif reaction of a trinuclear oxobridged iron compound is studied by means of Mössbauer spectroscopy. The results show that the iron catalyst breaks up into monomers when pyridine is added to it. Moreover, a complex spectrum is observed when the iron catalyst is dissolved in pyridine and/or acetic acid is added. The monomers (i.e. intermediate HS Fe(III)) formed in samples 3 and 4 have been investigated in detail by means of NIS and DFT calculations and will be discussed in the next chapter. Mössbauer spectroscopy analysis of the samples 4 (active catalyst) and 6 (Gif reaction at zero time) show similar spectral features revealing that the Fe is Fe(II) with HS state. This Fe(II) monomer species is responsible for the carbon-hydrogen activation of Gif oxidation. The oxidation and spin state obtained from Mössbauer spectroscopy will be used for the DFT calculations, which serves as a comparison for the experimental NIS and to predict the molecular structure of the species.

Chapter 7

Gif reaction of a Fe complex as studied by NIS and DFT

7.1 Introduction

In this chapter nuclear inelastic scattering (NIS) studies of the Gif reaction will be presented. The information about oxidation and spin-spate of the iron atom of the catalyst under different Gif-type conditions from Mössbauer analysis will serve as a starting point for the density functional theory (DFT) calculations. These calculations facilitate the interpretation of the NIS spectra. The aim is to identify possible molecular structures of the intermediates and active catalyst that might be responsible for the initial carbon-hydrogen activation of the Gif reaction. The vibrational bands, force constants and mode composition factors of some relevant iron vibrations are obtained from NIS. Normal mode analysis based on DFT calculations were employed for the assignment of bands of the NIS spectra. The vibrational root mean square deviation (rmsd) of the iron atoms from each mode obtained from DFT computation are also presented. This provides a better understanding of the molecular structures of reaction intermediates.

7.2 Sample preparation

All samples were prepared in the same manner as described in chapter 6. The same sample numbering scheme as shown in table 6.1 of chapter 6 is used throughout this chapter. However, in order to acquire a good spectrum with high count rate in less time, the starting material anhydrous iron nitrate $Fe(NO_3)_3$ for the preparation of the trinuclear catalyst (and all other solution samples) was prepared from iron powder which was enriched to 95.4% in ^{57}Fe. The isotope was purchased from Advanced Materials Technologies Ltd. and used as received.

7.3 Measurement details

All solution samples were prepared at the nuclear resonance beamline ID18 of the European Synchrotron Radiation Facility (ESRF), Grenoble, France. Air sensitive samples were prepared inside a glove bag filled with an inert gas, either helium or nitrogen, and quickly frozen in liquid nitrogen. All measurements were done at 20 K. The frozen sample is mounted onto the cryostat coldfinger, which is precooled and maintained at ∼20 K. Moreover, during the mounting of air sensitive samples, nitrogen gas was continously blown over the sample holder and coldfinger so as to avoid exposure of the frozen solution sample to the open atmosphere. For more details about sample mounting and holders we refer to section 4.4 of chapter 4. NIS spectra were recorded between ~ -15 and $+100$ meV in 0.25 meV steps. Each scan required ∼35 min, and 7–15 scans were needed for each sample. All scans obtained from each sample were added before extracting the vibrational density of states (VDOS) from NIS data. Data evaluation, i.e. adding of NIS spectra, normalization and subtraction of the elastic peak and VDOS extraction were carried out using the Fortran code DOS V2.1 [60].

7.4 DFT and normal mode analysis

The geometry optimization and subsequent fundamental vibrational frequency calculations were performed using the Guassian 03 package [65]. All the molecular structures were built up with the program MOLDEN [78] and for displaying the plot program ORTEP-III [93] was used. The DFT-B3LYP level of theory was used in all calculations [61, 62]. Dunning's correlation-consistent polarized-valence double-ζ basis set was used for all atoms except Fe [66]. For the metal Fe atoms, the core electron wavefunctions were replaced by the scalar relativistic Stuttgart/Dresden effective core potential, which was combined with the corresponding basis set for the

Fe valence shells as described in reference [67]. The VDOS of ^{57}Fe was then simulated from the quantum mechanically calculated vibrational frequencies of each mode and normal coordinates of each atom. This procedure is the same as in section 5.4 of chapter 5.

7.5 Force constant analysis

The ^{57}Fe VDOS derived from the NIS energy spectrum can be used to obtain the mean stiffness of the iron environment. The stiffness is the force constant for the vibrational displacement of the ^{57}Fe nucleus in the direction of the X-ray beam, with other nuclei fixed at their equilibrium positions. Therefore the lengths of the bonds between the iron and its nearest neighbours are correlated to the force constant. The nearest neighbouring nucleus or ligands of the Mössbauer nucleus have a primary influence on the stiffness and therefore probe the local structure. The stiffness is inversely related to the Fe−ligand bond lengths. The force constant of the Fe−ligand bond can be obtained from the following relation [35, 38]:

$$\text{Force constant} = \frac{m_{\text{Fe}}}{\hbar^2} \int E^2\, g(E)\, \mathrm{d}E, \tag{7.1}$$

where m_{Fe} is the mass of the iron nucleus. For ^{57}Fe $m_{\text{Fe}} = 9.454 \times 10^{-26}$ kg. $\hbar = h/(2\pi)$ and E is the wavenumber or vibrational energy (1 meV$=$ 8.066 cm^{-1}). By performing appropriate unit conversion one obtains $m_{\text{Fe}}/\hbar^2 = 3.354 \times 10^{-3}$ N m^{-1} cm^2. In eq. (7.1), E should be in cm^{-1}. If E is in meV then $m_{\text{Fe}}/\hbar^2 = 0.218$ N m^{-1} meV^{-2}. After the conversion of the VDOS specturm to the force constant spectrum using eq. (7.1), one can find the force constant of a particular mode of vibration of the Fe displacement by just finding the area of a peak that is reponsible for that vibration. In the present work we have used the peak fitting program [94] for finding the area, position, width and height. All peaks were assumed to be Lorentzian profiles with all fitting variables, peak position, height and full width at half maximum are allowed free to vary in the fitting routine.

7.6 Results and discussion

7.6.1 Core of the trinuclear structure

The nonheme trinuclear oxobridged iron complex, which is already introduced in the previous chapter (see fig. 6.1 and section 6.4.1 of chapter 6), does not crystallize, therefore, structural characterization cannot be carried out by X-ray diffraction. It was shown by X-ray absorption spectroscopy (XAS), that this complex contains a Fe_3O core structure with the Fe atom octahedrally coordinated to six oxygen atoms [83]. However, the sixth coordination at the Fe center could also be a chlorine atom as found in elemental analysis [83]. Moreover, with different ligand (alkyl chain, n) lengths of the trinuclear iron compound there is no significant change in the XAS spectra. The core of the trinuclear iron complex contains three iron atoms, and each iron atom is bonded to the central oxygen ($O_{\mu\text{-oxo}}$) atom. Thus the three Fe atoms form an equilateral triangle with an oxygen atom in the centroid. Because of the complex structure of the trinuclear catalyst, only the core, i.e. the truncated central

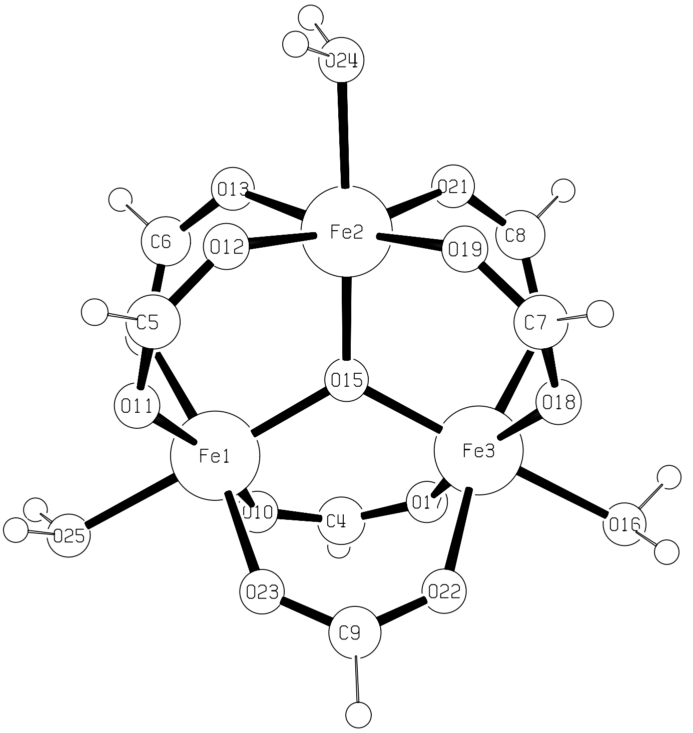

Figure 7.1: DFT optimized structure of the core $[(Fe_3O)(OOCH)_6(H_2O)_3]^+$ of the trinuclear iron complex. Atoms that are not labelled are hydrogen.

fragment, can be modelled well using DFT methods. In the calculation, the spin-state S for each Fe atom is taken as 5/2 with a total multiplicity of the fragment/core structure of 16 and a charge of +1. The optimized structure is shown in fig. 7.1 and its VDOS in fig. 7.2 (bottom). Before assigning the iron vibrational modes a few essential details have to be considered.

The fraction of kinetic energy associated with the motion of ^{57}Fe in a mode j is called mode composition factor e_j^2. Without rigorous calculation the contribution due to intermolecular lattice vibration can be determined by e_j^2. The mode composition factor for each acoustic mode (there are three acoustic modes in a given crystal: two transverse and one longitudinal) associated with the ^{57}Fe is given by [95, 96]:

$$e_{\mathrm{ac}}^2 = \frac{n_{\mathrm{f}}\, m_{\mathrm{Fe}}}{M_{\mathrm{tot}}}, \tag{7.2}$$

where n_{f} is the number of Mössbauer nuclei present in the molecule, m_{Fe} is the mass of ^{57}Fe and M_{tot}(=1166.47 u for alkyl chain length $n = 2$ and 1281.92 u for $n = 3$) is the total mass of the molecule. The expression (7.2) also applies to the translational vibrational modes of a molecule of total mass M_{tot} [97].

According to eq. (7.2), the mode composition factor for $n = 2$ is 14.6% and the integral over the VDOS reaches this e_j^2 value at 100 cm^{-1}. Therefore the region from 0 to 100 cm^{-1} can be attributed to lattice modes. For the trinuclear complex with alkyl chain length $n = 3$, e_j^2 is 13.3% and the lattice modes extends up to 86 cm^{-1}. In particular, the peak at ∼38 cm^{-1} should be attributed to lattice modes in both complexes ($n = 3$ and 2). Since the DFT calculations were performed on single molecules, the intermolecular (acoustic, translational and rotational) or lattice modes are not reproduced. Hence, the features below ∼100 cm^{-1} in the calculated spectrum shown in fig. 7.2 (bottom) are essentially, not the intermolecular vibrational modes.

The highest possible mode composition factor e_{max}^2 for a given molecule is given by [95, 96]:

$$e_{\mathrm{max}}^2 = \frac{M_{\mathrm{tot}} - m_{\mathrm{Fe}}}{M_{\mathrm{tot}}}. \tag{7.3}$$

According to (7.3), e_{max}^2 for the trinuclear compound with $n = 2$ is 0.951 and with $n = 3$ is 0.956. For randomly oriented samples the mode composition factor for a particular peak, which originates from intramolecular optical modes (Einstein modes), associated with ^{57}Fe can be determined from the peak area according to the relation:

$$e_j^2 = 3 \int g(E)\, \mathrm{d}E \quad \text{and} \quad \sum_{j=1}^{3N} e_j^2 = 3. \tag{7.4}$$

It should be noted that the sum of all e_j^2 over N atoms in the molecule and over $3N$ modes (includes zero frequency, i.e. rotation and translation) of the molecule is equal to one and three, respectively. The area of $g(E)$ is normalized to one. Although the experimental VDOS of both complexes displays similar spectral features, the peak at 337 cm^{-1} is less pronounced in the complex with the smaller alkyl spacer ($n = 2$) compared to the complex with the longer alkyl spacer ($n = 3$). The peak at 246 cm^{-1} in the complex with $n = 2$ as seen at the right shoulder of the highest peak is not seen in the complex with $n = 3$ (see fig. 7.2).

Table 7.1: Summary of NIS on trinuclear iron complex ($n = 2$) and DFT calculation for $[(Fe_3O)(OOCH)_6(H_2O)_3]^+$. Only the normal modes with significant iron vibrational displacement are listed in the fourth column. The mode composition factor e_j^2 and the force constant (FC) of Fe−ligand bond are calculated according to (7.4) and (7.1), respectively.

Experimental wavenumber [cm^{-1}]	FC from NIS [N m^{-1}]	e_j^2	Calculated wavenumber [cm^{-1}]	rmsd^c [Å]	Mode description according to fig. B.1 (D_{3h})
38	—	0.38	—	—	lattice modes
141	4.2	0.83	142.5	0.19	E'' (ν_9) (or E_u (ν_7)^a)
			151.1	0.32	E' (ν_2)
			152.9	0.38	E' (ν_2)
208	37.7	0.76	192.5	0.39	E' (ν_5)
			195.9	0.33	E' (ν_2)
			198.0	0.64	A_2' (ν_7) (or E_u (ν_7)^a)
			206.5	0.23	E' (ν_3)
			210.5	0.23	E' (ν_3)
			217.6	0.05	A_2'' (ν_4)
246	14.4	0.19	230.9	0.36	A_1' (ν_1)

continued on next page. . .

Table 7.1 continued from previous page

Experimental wavenumber [cm^{-1}]	FC from NIS [N m^{-1}]	e_j^2	Calculated wavenumber [cm^{-1}]	rmsd^c [Å]	Mode description according to fig. B.1 (D_{3h})
308	38.8	0.35	296.0	0.09	E' (ν_2)
			297.3	0.08	E' (ν_2)
			301.9	0.10	E' (ν_5)
			303.5	0.14	E' (ν_5)
			314.3	0.12	A_1' (ν_1)
337	19.8	0.18	331.0	0.18	A_1' (ν_1)
			341.3	0.32	A_2' (ν_7) (or E_u (ν_7)^a)
			351.4	0.35	E'' (ν_8) (or E_u (ν_6)^a)
			352.0	0.29	E'' (ν_8) (or E_u (ν_6)^a)
			355.7	0.24	E' (ν_6)
			360.5	0.39	E'' (ν_8) (or E_u (ν_6)^a)
391	79.1	0.45	383.9	0.28	E' (ν_3)
			394.5	0.39	A_1' (ν_1)
			400.1	0.44	A_1' (ν_3)
			410.6	0.45	A_2'' (ν_4)
447	27.3	0.10	449.2	0.04	E' (ν_6)
538	3.3	0.01	Since these peaks are broadened and not well-resolved, we are not able to assign these bands extensively. The calculated peaks 468.1 (ν_6), 480.5 (ν_6), 565.6^b (ν_5) and 577.5^b (ν_6) correspond to the E' mode; 592.9 and 597.7 to E'' (ν_8); and 607.7 to A_2'' (ν_4).		
596	44.0	0.13			

[a] Numbered according to D_{4h} symmetry, i.e. considering the three FeO_4 units. For details, see fig. B.2 and table B.1 of appendix B.

[b] These wavenumbers involve a relatively large $O_{\mu\text{-oxo}}$ displacement than Fe.

[c] Sum of the rmsd of the three Fe atoms obtained from calculation.

The force constants calculated from the experimental VDOS are somewhat different from the ones computed using DFT. In NIS the force constant gives the mean

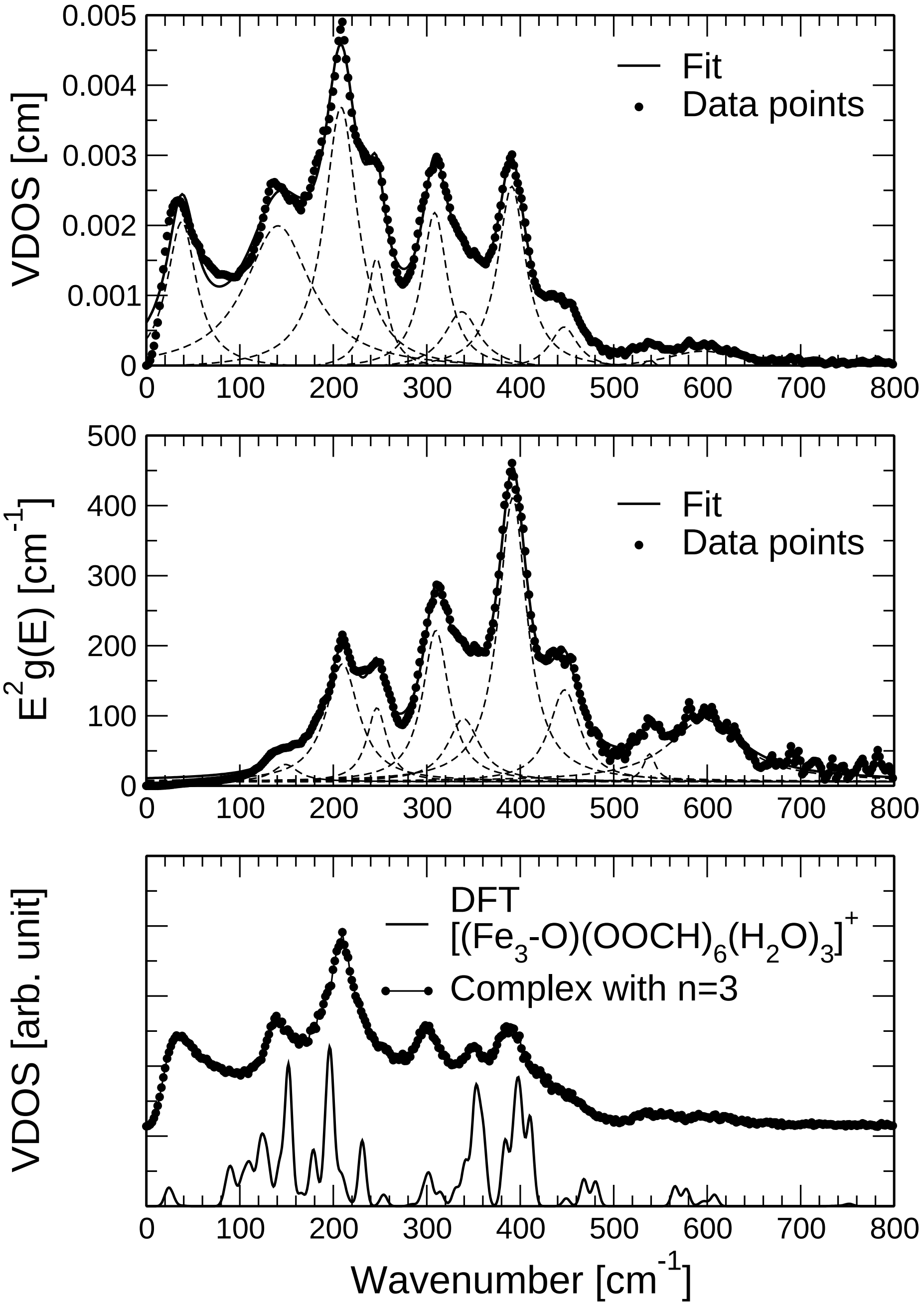

Figure 7.2: Experimental ^{57}Fe VDOS of trinuclear complex with $n = 2$ (top), VDOS respresented in terms of the integrand $E^2 g(E)$ of the mean Fe−ligand bond stiffness using eq. (7.1) (center), and DFT calculated VDOS of the core of the trinuclear iron compound (shown in fig. 7.1) together with the experimental VDOS of another trinuclear complex with $n = 3$ (bottom). The dashed curves represent the results of a fit of the VDOS to a series of Lorentzian peaks. The experimental VDOS in the bottom panel is offset for clarity of representation.

force needed for the iron atom to return to its equilibrium position after a unit displacement in a particular iron vibrational mode [95]. In DFT computations all bonds between all atoms in a given molecule are considered. All motions of all atoms in a particular mode form an average configuration in which all bonds contribute to the force constant. But in NIS the force constant is primarily the iron (or iron together with a fragment) vibrational displacement with respect to another atom (or fragment). Therefore in table 7.1, the force constants computed by DFT calculation are not given.

In the low-frequency region, the experimental VDOS (peak at 38 cm^{-1}) is due to lattice modes. In this region, the DFT (of single molecule) spectra are usually dominated by symmetric and asymmetric modes of vibration of the six $[\mathrm{OOCH}]^-$ units. These kind of vibrations are generally known as framework, librational or cluster torsional modes. Therefore, the DFT predicted wavenumbers for this region are not listed in table 7.1.

The DFT calculated VDOS is qualitatively matching with the experimental VDOS of both complexes. From this it seems that the increase in ligand length does not considerably affect the VDOS of the truncated fragment and the ligands, i.e. the carboxyl and alkyl groups do not strongly influence the VDOS of the core. The results of peak assignments based on experimental and DFT computed vibrational frequencies are summarized in table 7.1. The VDOS of $^{57}\mathrm{Fe}$ in the trinuclear iron ($n = 2$) catalyst is shown in fig. 7.2 (top).

Band assignments

Due to the complications in analysing the full trinuclear complex, we describe the core structure as three planar D_{4h} symmetry units interacting under a D_{3h} unit [98, 99] and the correlations between the two symmetries are given in table B.1 of appendix B. The complex contains three planar $\mathrm{FeO_4}$ units, having D_{4h} symmetry and lying perpendicular to the Fe−O bonds of the $\mathrm{Fe_3O}$ unit. The central $\mathrm{Fe_3O}$ unit forms a D_{3h} symmetry unit. Most of the iron vibrational bands are assigned by considering only the local D_{3h} symmetry of the $\mathrm{Fe_3O}$ unit.

The experimental VDOS shows broadened peaks. There are four major peaks at 141, 208, 308 and 391 cm^{-1}. DFT predicts multiple contributions to these unresolved experimental features. For the 141 cm^{-1} peak, the line width of which is 85.7 cm^{-1}, the three DFT calculated peaks appear at 142.5, 151.1 and 152.9 cm^{-1}. The DFT calculated band at 142.5 cm^{-1} closely matches the experimental value, but the sum of the rmsd of all iron atoms (0.19 Å) in this mode is less when compared to the other two bands. The largest rmsd is observed for the band at 152.9 cm^{-1}. In NIS the peak with maximum height has the largest rmsd, and the peak area is directly proportional to e_j^2. In other words, e_j^2 is proportional to the contribution of mode j to the rmsd of Fe. Therefore the contribution to the experimentally observed band at 141 cm^{-1} is larger from the 152.9 cm^{-1} band as compared to the other two bands.

The line width of the highest peak at 208 cm^{-1} is 42.9 cm^{-1}, which is far greater than the experimental resolution of 8.9 cm^{-1} (1.1 meV). In this region DFT predicts six vibrational bands, see table 7.1 and fig. 7.1. All these six theoretical vibrational peaks contribute to the band at 208 cm^{-1}. However, based on the DFT calculation, the maximum rmsd is observed for the band at 198.0 cm^{-1}, which is an A_2' vibration. Hence the maximum contribution to the experimentally determined band at 208 cm^{-1} is due to A_2'. The mode A_2' of the $\mathrm{Fe_3O}$ unit in D_{3h} symmetry can be correlated to the E_u mode of the $\mathrm{FeO_4}$ unit in D_{4h} symmetry (see correlation table B.1 of appendix B). Johnson et al. [98] have observed a corresponding band in complexes similar to ours, at a comparable wavenumber (200 cm^{-1}). Based on a local D_{3h} symmetry Johnson et al. assigned the 200 cm^{-1} band to A_2', A_2'', E' and E'' modes and in our case all these modes are found in the DFT computation.

The line width of the band at 308 cm^{-1} is 33.4 cm^{-1}. In this spectral region, DFT predicts five modes, most of them are of E' type. The mode closest to this experimental feature is at 303.5 cm^{-1}, which is an E' vibration as suggested by DFT. Moreover, the rmsd of the band at 303.5 cm^{-1} is 0.14 Å, which is larger than that of other DFT predicted bands in this region.

The force constant of the 391 cm^{-1} band is 79.1 $\mathrm{N\,m}^{-1}$, which is the largest of all the experimentally determined values. By considering the rmsd, the maximum contribution to this band is due to an A_2'' vibration as predicted by the DFT calculated band at 410.6 cm^{-1} (rmsd 0.45 Å).

In the high-frequency region, most of the iron modes have a very small iron rmsd (less than 0.1 Å) except the bands at 565.6 and 577.5 cm^{-1} where the vibrational modes are accompanied with a large vibrational displacement of the central oxygen atom $\mathrm{O}_{\mu\text{-oxo}}$. Around 600 cm^{-1}, some tiny peaks are observed which are clearly visible in the $E^2g(E)$ spectrum shown in fig. 7.2 (center) and can be compared to the calculated VDOS (fig. 7.2, bottom). But since the experimental VDOS in this region is broadened and cannot be resolved by fitting routines we used only one broadened Lorentzian peak (peak position 596 cm^{-1}) just for the sake of proper fitting so as to get meaningful parameters for the other peaks.

Comparison of complexes with n=2 and 3

The well-resolved shoulder at 246 cm^{-1} in the complex with $n = 2$ is assigned to the symmetric stretching mode A_1', which is predicted by DFT at 230.9 cm^{-1}. This feature is not seen in the trinuclear complex with a longer alkyl spacer ($n = 3$) as shown in fig. 7.2 (bottom). From this observation it seems that the longer alkyl spacer may influence the symmetrical stretch of the Fe_3O unit and probably hinders the A_1' vibration. The other possible reason could also be the most dominating band at 208 cm^{-1} the A_2' mode of which is favourable for higher alkyl spacer complexes and has a tendency to suppress A_1' in larger ligand complexes.

In the experimental VDOS the band at 337 cm^{-1} is dominated by several rotational vibrations as predicted by the DFT calculation. These different rotational vibrations (A_2' and E'') can be correlated to the genuine E_u modes of three FeO_4 units in D_{4h} symmetry (see table B.1 of appendix B). This band is not resolved in this complex but in the complex with the larger ligand, it is resolved.

7.6.2 Normal mode and force constant analysis of monomer 1

We have already shown in the previous chapter that Mössbauer spectroscopy results give hints that the trinuclear catalyst breaks up into monomers when it is dissolved in pyridine and/or acetic acid. Complex spectra with complicated spectral line shapes are observed, see fig. 6.4 of chapter 6.

In catalysis, it is known that reduced Fe metal ions (Fe(II)) are ideally suited as catalysts for oxidation reactions (with molecular oxygen) as they readily react with molecular oxygen to give monomers, which act as oxidants, such as iron-superoxo ($\mathrm{Fe(III)}{-}\mathrm{O}_2^-$), iron-peroxo ($\mathrm{Fe(III)}{-}\mathrm{O}_2^{2-}$) or high-valent iron-oxo (Fe(IV)=O and Fe(V)=O) species [1]. According to [100, 101] the active catalytic part of the possible intermediate for the catalysis of naphthalene dioxygenase is an iron monomer with side-on binding of two oxygen atoms. However, Rhode et al. [102] in the same issue revealed that the possible intermediate species is Fe(IV)=O in some nonheme

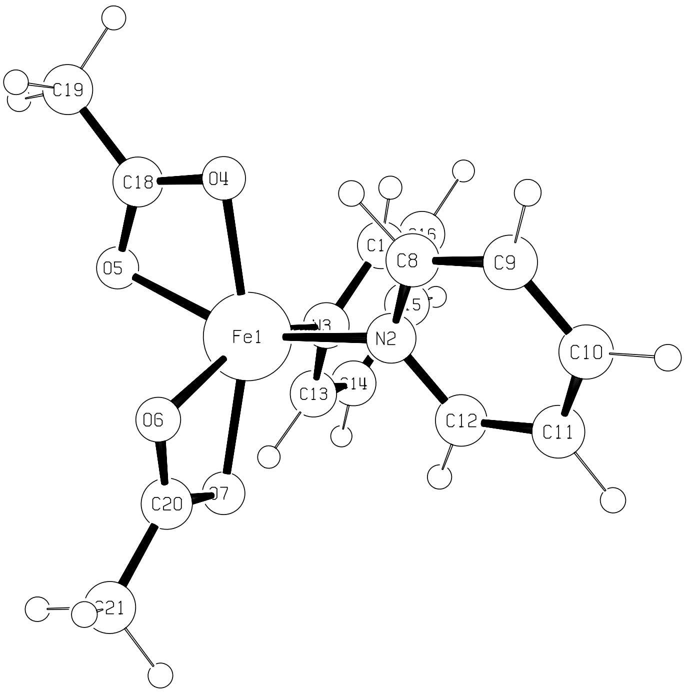

Figure 7.3: Structure of a possible monomer $[Fe(C_5H_5N)_2(O_2CCH_3)_2)]^+$, i.e. sample 3, based on DFT calculations. Atoms that are not labelled are hydrogen.

iron systems. A unified mechanistic scheme for dioxygen activating iron enzymes, cytochrome P450, methane monooxygenase and Rieske (2Fe−2S) dioxygenase, can be found in [103].

Based on the survey of various Fe intermediates that catalyze nonheme enzymes using molecular oxygen, it was observed that the majority of them are monomers either with end-on or side-on binding of oxygen atoms [100]. The remaining coordination sites of iron are bonded to ligands. The iron atom is in the Fe(III) high-spin (HS) state. According to literatures [102, 103] (and references therein) the active intermediate seems to be a high valent iron bonded to a terminal oxygen atom. For the Gif system studied in this thesis, none of the DFT simulated VDOS of the reported structures coincide with the experimentally observed VDOS. After optimizing the structure of several monomers using DFT methods, only the structure shown in fig. 7.3 gave convincing results. This structure is somewhat similar (not identical) to the intermediate found in Rieske dioxygenases [2, 100], and close to a structure as reported in [104]. The DFT optimized structure of the possible monomer

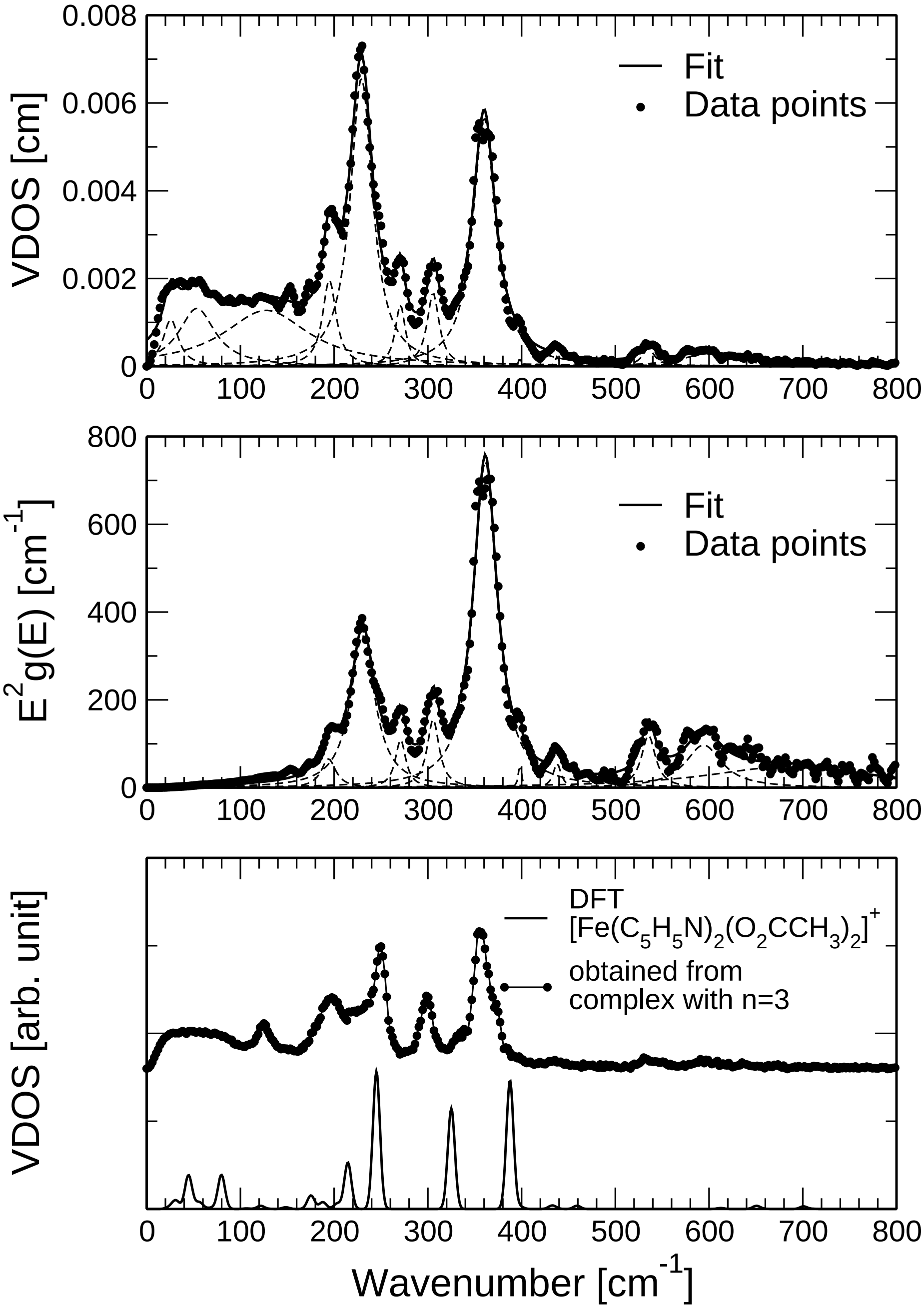

Figure 7.4: Experimental ^{57}Fe VDOS of sample 3 prepared from complex with $n = 2$ (top), VDOS represented in terms of the integrand $E^2 g(E)$ of the mean Fe–ligand bond stiffness using eq. (7.1) (center), and DFT calculated VDOS of the possible monomer (shown in fig. 7.3) together with the experimental VDOS of sample 3 prepared from the complex with $n = 3$ (bottom). The dashed curves represent the results of a fit of the VDOS to a series of Lorentzian peaks. The experimental VDOS in the bottom panel is offset for clarity of representation.

$[Fe(C_5H_5N)_2(O_2CCH_3)_2]^+$ is shown in fig. 7.3 and the VDOS simulated from the DFT calculation is shown in fig. 7.4 (bottom). The Mössbauer spectra of samples 2 and 3 show paramagnetic relaxation which is usually found in HS Fe(III) compounds, hence in the DFT calculation the spin state of iron was taken as HS ($S = 5/2$) with total charge of the molecule as +1 and multiplicity of 6. The experimental VDOS of the sample 2 shown in fig. 7.5, although broadened, displays somewhat similar spectral features when compared with that of sample 3 as shown in fig. 7.4 (top). As the VDOS of sample 3 is well-resolved compared to sample 2, only the results corresponding to sample 3 will be discussed further.

The experimental VDOS shown in fig. 7.4 (top), is in agreement with the theoretically computed VDOS as shown in the bottom panel. On comparing the experimental VDOS of sample 3 prepared from a complex with alkyl spacer of $n = 2$ and $n = 3$, we see that the tiny peak at 271 cm^{-1} is absent in the sample, which is prepared from the complex with large alkyl spacer $n = 3$. Moreover, sample 3 prepared from complexes with $n = 3$, 4 and 5 all exhibit similar spectral features (not shown).

First we discuss the assignment of the lattice modes. The lattice modes according to relation (7.2) are 17.09%(=56.94/333.22) of the total VDOS and the integral area reaches this area at 112 cm^{-1}. Therefore the bands at 26 and 54 cm^{-1} which lie in the region up to 112 cm^{-1} can be assigned to lattice modes. However from fig. 7.4 (top) we see that the molecular modes do not proceed immediately after the lattice modes. Therefore this region may be associated with rotational modes (lattice optical modes) with a relatively small rmsd of the Fe atom. Furthermore, a well defined lattice optical mode is observed by the presence of the tiny peak at ∼155 cm^{-1} (since this peak is relatively small, it is not considered in the fitting routine). This peak is slightly enhanced in the complex with a larger alkyl spacer and shifted to ∼123 cm^{-1}, see fig. 7.4 (bottom).

For this monomer the experimentally resolved strongest VDOS bands are at 229, 306 and 360 cm^{-1} as seen in fig. 7.4. These three features are matched by the three strongest bands of the DFT predicted VDOS. A summary of assignments is given in table 7.2. The deviation of the calculated wavenumbers is less than 7.7% with respect to the observed ones, except for the band at 195 cm^{-1} it is 10.1%. By comparison of the experimental VDOS with DFT simulated VDOS the band at 195 cm^{-1} is assigned to in-plane symmetrical stretch of N−Fe−N. The vibrational band at 229 cm^{-1} in the experimental VDOS is the highest of any other band. As mentioned earlier the

Table 7.2: Assignments and summary of some NIS-based and DFT-calculated wavenumbers for sample 3. The mode composition factor e_j^2 and force constant (FC) of the Fe−ligand bond calculated according to (7.4) and (7.1), respectively. Details of the fitting procedure are described in the text, see section 7.5.

Experimental wavenumber [cm^{-1}]	FC from NIS [$N\ m^{-1}$]	e_j^2	Calculated wavenumber [cm^{-1}]	rmsd[a] [Å]	Mode description according to fig. B.4
26, 54, 127	—	—	—	—	lattice modes
195	6.6	0.16	214.7	0.17	sym. stretch N−Fe−N (ν_1)
229	57.7	0.90	245.1	0.37	asym. stretch N−Fe−N (ν_2)
271	7.9	0.09	—	—	—
306	12.8	0.12	325.0	0.30	sym. stretch N−Fe−N (ν_1)
360	119.3	0.79	387.6	0.34	described in text (ν_5)
398	1.1	0.14	398.4	0.02	asym. stretch O−Fe−O
438	3.0	0.01	431.7	0.03	rocking N−Fe−N (ν_4)
			435.6	0.02	scissoring N−Fe−N (ν_3)

[a] root mean square displacement of the Fe atom obtained from calculation.

strongest band has the highest rmsd of the Fe atom. According to DFT calculation, this band is assigned to the in-plane asymmetrical stretching of N−Fe−N with a rmsd of 0.37 Å, which is the highest of all rmsd as predicted by DFT. The shoulder-like peak at 271 cm^{-1} is observed only in the sample prepared from complex with $n = 2$ and not seen in the sample prepared from the complex with alkyl spacer of $n = 3$. Moreover, DFT predicts no iron vibrational bands in this region. The band at 306 cm^{-1} is assigned to the symmetrical stretching mode of N−Fe−N as predicted by DFT. This vibration is similar to the mode as observed in 214.7 cm^{-1}, but the two pyridine ligands are almost fixed. The third highest band is seen at 360 cm^{-1} and can be compared to 387.6 cm^{-1} as predicted by DFT. This peak is assigned to the out-of-plane (plane formed by Fe and two N atoms) vibration of the Fe atom. This vibration is also coupled to the asymmetrical stretching of the Fe with respect to two acetate anions, i.e. CH_3COO^-, as shown in fig. B.4 (ν_5) of appendix B. The

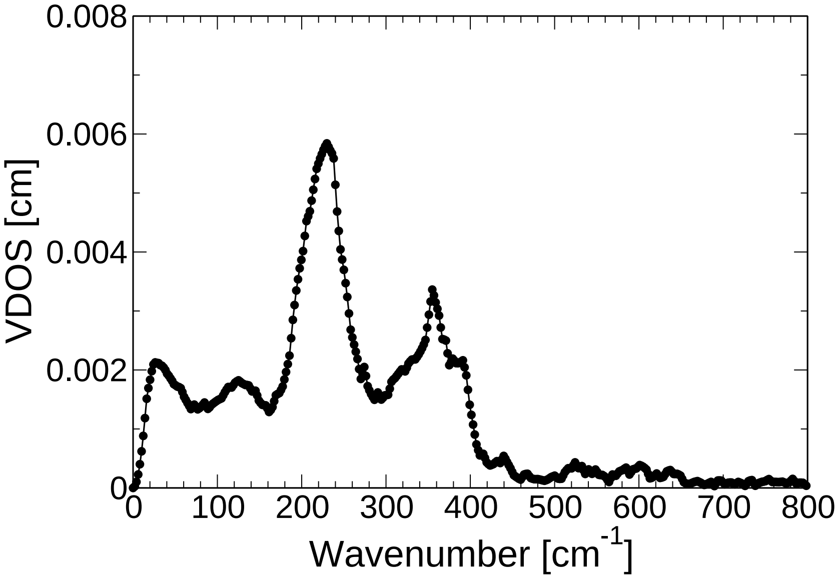

Figure 7.5: Experimental ^{57}Fe VDOS of trinuclear complex ($n = 2$) in pyridine (sample 2) at 20 K.

tiny shoulder at 398 cm^{-1} the force constant of which is 1.1 N m^{-1} is assigned to the asymmetric stretching vibration of O−Fe−O. This band involves a very small vibrational displacement of 0.02 Å of the Fe atom. The small peak at 438 cm^{-1} in the high-frequency region of the experimental VDOS consists of two peaks according to the DFT calculation. The theoretical peak at 431.7 cm^{-1} is assigned to the rocking bend of N−Fe−N and the band at 435.6 cm^{-1} to scissoring the in-plane bend of N−Fe−N. For these bands the fact that the force contant is inversely proportional to the rmsd, is overruled because of small e_j^2. The high-frequency bands are not assigned extensively, although the calculated peaks in the region 600–720 cm^{-1} can be compared with the poorly resolved peaks in the experimental VDOS in the region 500–720 cm^{-1}.

7.6.3 Normal mode and force constant analysis of monomer 2

Monomer 2 (sample 4 in table 6.1 of chapter 6) is prepared by dissolving the trinuclear iron compound in a mixture of pyridine, acetic acid and metallic zinc in an inert atmosphere. On adding cyclohexene to sample 4 (i.e. sample 6) under inert atmosphere there is no significant change in the VDOS. However the three high-frequency bands between 520 and 700 cm^{-1} disappeared, see fig. 7.8. Sample 4 prepared from higher carbon chain length exhibits the same spectral feature, i.e. sample 4 prepared from complex with $n = 2$, 3 and 4 displays almost the same VDOS. Sample 6 (Gif reaction at zero time) also shows the same VDOS as that of sample 4, hence, this monomer should be a species chemically similar to the active catalyst. Although the VDOS of sample 4 prepared from the complex with $n = 2$ is same as that of sample 4 prepared from the complex with alkyl spacer $n = 3$, we discuss the latter due to its well resolved peaks.

Singh et al. [104] have reported crystal structures of some intermediates formed in a Gif reaction of iron complexes (similar to our trinuclear complexes). For our work, we built up one of those reported structures using Molden [78] and used it for calculation. While building the molecule the four pyridine units are tilted by ∼45° to the plane FeN_4 and form a propeller-like geometry. The bond lengths are of default values as provided by Molden [78]. By DFT structure optimizing, only three pyridine rings are arranged in a propeller-like geometry around the FeN_4 unit, while the other

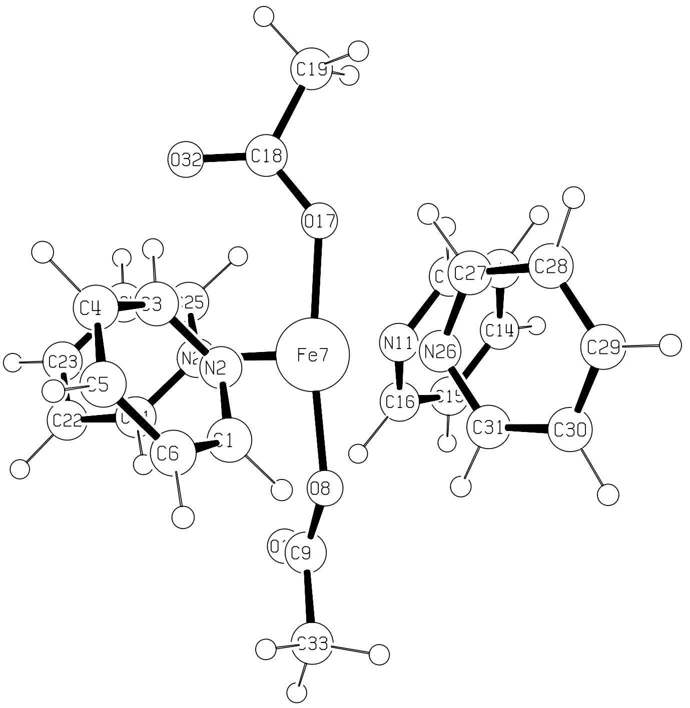

Figure 7.6: Structure of a possible active catalyst $Fe^{2+}(C_5H_5N)_4(O_2CCH_3)_2$, i.e. sample 4, based on DFT calculations (spin state 2; multiplicity 5). Atoms that are not labelled are hydrogen.

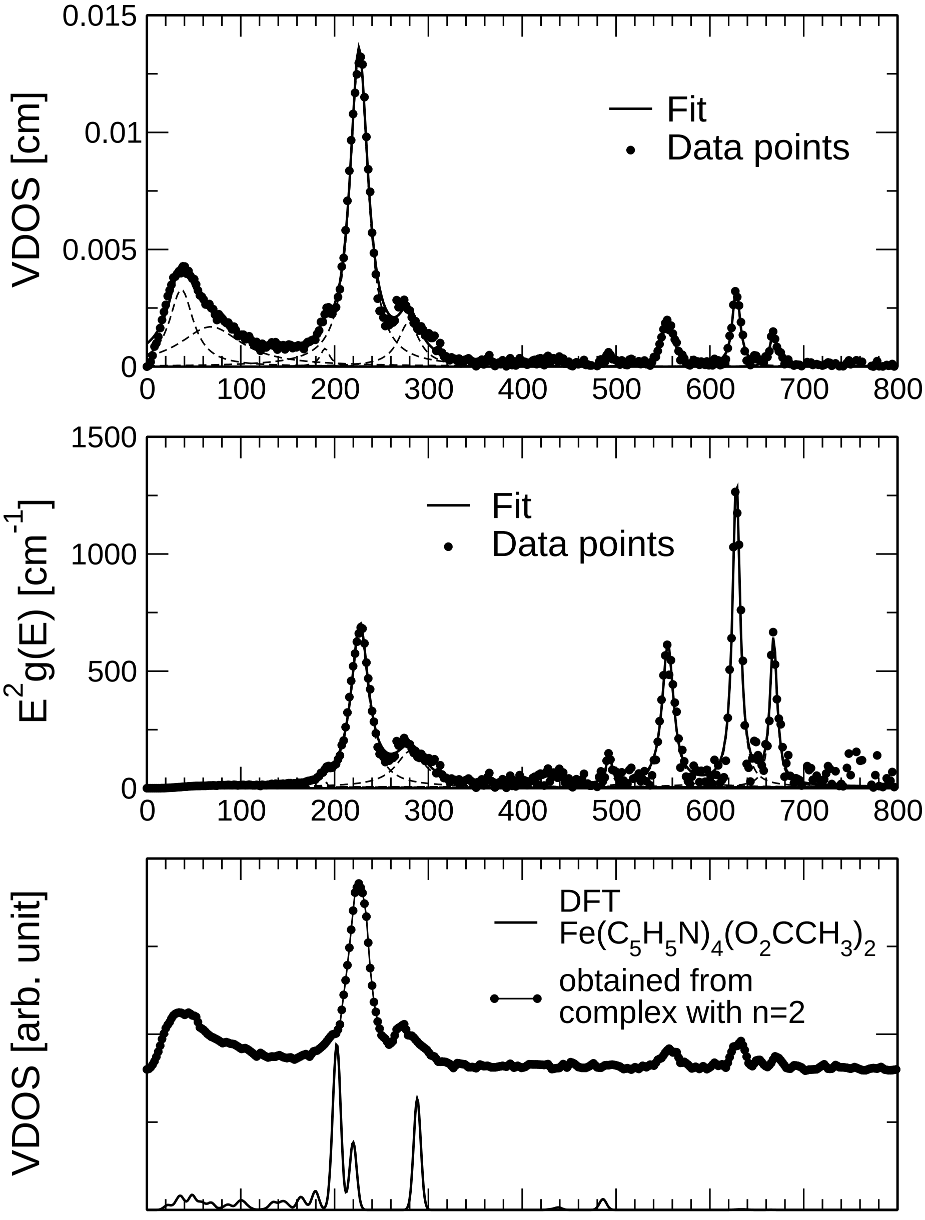

Figure 7.7: Experimental ^{57}Fe VDOS of sample 4 prepared from complex with $n = 3$ (top), VDOS respresented in terms of the integrand $E^2\, g(E)$ of the mean Fe−ligand bond stiffness using eq. (7.1) (center), and DFT calculated VDOS of the possible monomer (shown in fig. 7.6) together with the experimental VDOS of sample 4 prepared from the complex with $n = 2$ (bottom). The dashed curves represent the results of a fit of the VDOS to a series of Lorentzian peaks. The experimental VDOS in the bottom panel is offset for clarity of representation.

Table 7.3: Summary and assignments of some NIS-based and DFT-calculated wavenumbers for sample 4. The mode composition factor e_j^2 and force constant (FC) of the Fe−ligand bond calculated according to (7.4) and (7.1), respectively. Details of the fitting procedure are described in the text, see section 7.5.

Experimental wavenumber [cm^{-1}]	FC from NIS [N m^{-1}]	e_j^2	Calculated wavenumber [cm^{-1}]	rmsd[a] [Å]	Mode description according to figs. B.2 and B.3
37, 68	—	—	—	—	lattice modes
190	0.3	0.05	179.5	0.10	A_{2u} (ν_3)
226	80.0	1.46	199.7	0.22	E_u ($\nu_8 + \nu_{13}$)
			203.5	0.41	E_u ($\nu_8 + \nu_{13}$)
			219.8	0.23	E_u ($\nu_8 + \nu_{13}$)
279	31.6	0.25	288.1	0.29	A_{2u} (ν_{11})
429	8.6	0.03	430.3	0.01	A_{2u} (ν_3)
			437.8	0.02	E_u (ν_8)
			439.1	0.02	E_u (ν_8)
493	4.8	0.02	486.0	0.06	A_{2u} (ν_{11})
555	46.9	0.13	According to DFT these peaks involves relatively very small (0.01 Å) rmsd of Fe atom mostly of Fe−N stretch coupled to vibrations of pyridine ligands. Therefore, these peaks are not assigned rigorously.		
628	66.8	0.15			
668	29.3	0.06			

[a] root mean square displacement of the Fe atom obtained from calculation.

pyridine ring (which has N26 in fig. 7.6) is inclined ~45° to the other three pyridine rings. The theoretical VDOS is shown in fig. 7.7 (bottom).

For simplicity, the band assignments are made on the basis of D_{4h} symmetry considering the local tetragonal FeN_4O_2 unit, which gives 15 normal modes of vibration. These normal modes of vibration belong to $2A_{1g}$, $2A_{2u}$, $3E_u$, B_{1g}, B_{2g}, E_g

and B_{2u} symmetry modes [105, 106]*. In fig. B.2 of appendix B nine of the fifteen fundamental normal modes of vibration for D_{4h} are shown and the remaining six modes are given in fig. B.3.

Experimental and calculated wavenumbers of the iron vibrational modes of sample 4 are given in table 7.3. First we start with assigning the low-energy modes. For the molecule shown in fig. 7.6, e^2_{ac} according to formula (7.2) is $0.12 (= 56.97/491.42)$ and the integral area of VDOS reaches this value at 48 cm^{-1}. Therefore the region up to 48 cm^{-1} should be attributed to lattice modes. In fig. 7.7 (top), we notice that the lattice modes seem to extend up to 100 cm^{-1}. Hence, the region 48–∼100 cm^{-1} can be attributed to optical lattice modes or librational modes associated with relatively small rmsd of the Fe atom.

The tiny band at 190 cm^{-1} seen as a shoulder is assigned to A_{2u} as predicted by DFT at 179.5 cm^{-1}. The highest band in the experimental VDOS is found at 226 cm^{-1} and has a mode composition factor of 1.46. This is more than the maximum value of 0.88 as obtained by eq. (7.3). Therefore, this mode consists of several degenerate modes. The DFT predicted modes are all of E_u type consisting of a mixture of O−Fe−O- and N−Fe−N-bends.

The next pronounced peak is found at 279 cm^{-1}. This band is assigned to A_{2u} (ν_{11}) (sometimes called umbrella vibration [106]) by comparison with DFT simulated VDOS in which it is predicted at 288.1 cm^{-1}. The tiny band at 429 cm^{-1} consists of three bands, two E_u and one A_{2u} modes, as predicted by DFT computation and each of these band seems to have a relatively small rmsd (less than ∼0.2 Å). The band at 493 cm^{-1} is assigned to the A_{2u} mode and has only 0.06 Å of Fe rmsd as predicted by DFT. The high-frequency peaks are well-resolved in the experimental VDOS. But the DFT calculated peaks show weak features in this region and all the bands have very small (0.01 Å) Fe vibrational rmsd. In this region the DFT calculated peaks are at 631.3, 631.5 and 633.5 cm^{-1} and are all E_u stretch modes.

Sample 6 displays spectral features similar to sample 4, but the high-frequency bands (above ∼520 cm^{-1}) are absent as shown in fig. 7.8. Therefore, all the experimentally calculated wavenumbers, force constants and mode composition factors shown in table 7.3 should be approximately valid for the experimental VDOS of sample 6 as well.

---

*In some books and research articles B_{2u} is often labelled as B_{1u} because of the choice of coordinate system which was considered, for example see [107].

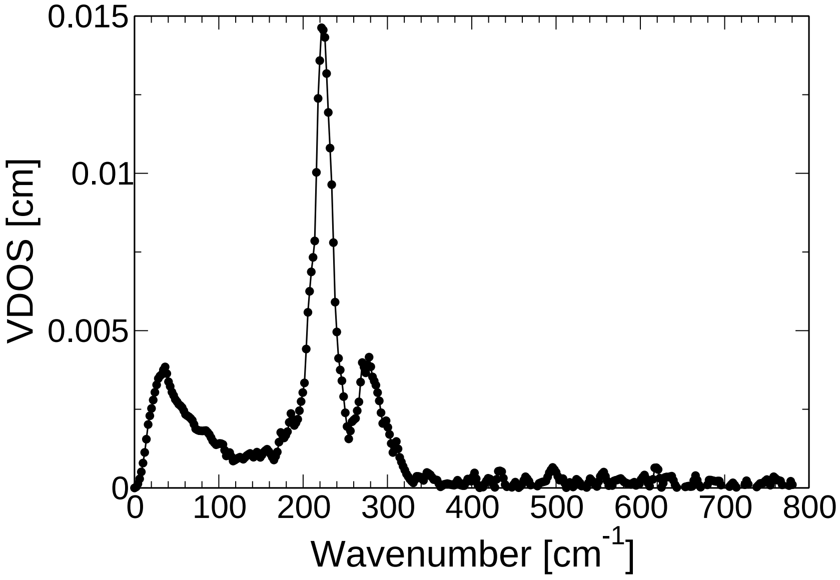

Figure 7.8: Experimental ^{57}Fe VDOS of trinuclear complex ($n = 2$) in a mixture of pyridine, acetic acid, metallic zinc and cyclohexene under inter atmosphere (sample 6, Gif reaction at zero time) at 20 K.

7.7 Conclusions

The iron vibrational dynamics of trinuclear oxobridged iron complexes is studied by means of NIS. Band assignments were made on the basis of normal mode analysis using DFT methods. A comparison between two complexes with variable alkyl chain spacer length is also presented. In addition, the Gif reaction of a trinuclear oxobridged iron complex (alkyl length, $n = 2$) is studied. Studies on the frozen solution of trinuclear complex in a mixture of pyridine and acetic acid, reveal that the trinuclear iron complex breaks up into monomers. In this monomer, the Fe atom is coordinated to two pyridine groups and two acetate groups. The two acetate ligands are bonded bidentally to the Fe atom. Band assignments were also done for this monomer.

The active catalyst, i.e. the iron compound dissolved in a mixture of pyridine, acetic acid and metallic zinc, resembles a monomer where the Fe atom is coordinated to four pyridine groups, forming a planar FeN_4 unit. The other two Fe sites are coordinated to two acetate groups via its oxygen atom approximately perpendicular to the plane of FeN_4. The NIS spectrum of this active catalyst is analyzed using the normal mode analysis based on DFT methods. The proposed structures of the different monomers are completely based on NIS and DFT methods, thereby proving that these methods can be useful for systems where structural determination using X-ray diffraction is not possible.

Chapter 8

Vibrational dynamics of a trinuclear Fe catalyst

8.1 Introduction

Polynuclear iron complexes occur broadly in nature and their study is important for many functions in mineralogy and biophysics. These complexes are well known for their novel properties and serve as a model for metalloproteins. The iron centers (active sites) of such metalloproteins perform various biological functions, such as iron storage (ferritin), oxidations of organic compounds using molecular oxygen (methane monooxygenase), transport and storage of dioxygen (hemerythrin). It is known that the metal triangle unit of the trinuclear oxobridged complex forms a smallest building block of the ferritin core [108]. Moreover, electron transfer processes in some trinuclear iron clusters have been throughly studied [109]. The electron transfer reactivity of ligands is often controlled by metal ions of the cluster [110], hence, the vibrational spectrum of the metal ions may provide insight into such a processes. Acquiring the vibrational spectrum of these complexes, especially below $\sim$500 cm^{-1} where most of the iron vibrations appear, is still a challenging task. A detailed assignment of vibrational bands is often nontrivial by the semiempirical force field approach [111, 112]. In this chapter, a trinuclear oxobridged iron complex will be studied by Mössbauer spectroscopy, nuclear inelastic scattering (NIS) and Raman spectroscopy. Vibrational bands are assigned by normal mode analysis based on quantum mechanical calculations using the density functional theory (DFT).

8.2 Sample preparation

The trinuclear complex is prepared by the reaction of the deprotonated ligand with iron(III) perchlorate, $Fe(ClO_4)_3$ [85]. On precipitation, the complex crystallizes out as red crystals. The molecular structure obtained from X-ray crystallographic analysis at room temperature (RT) is shown in fig. 8.1. The complex contains strongly disordered solvent water molecules (not shown in fig. 8.1). The reaction is the same as shown in fig. 6.1 (top) of chapter 6, but, instead of $Fe(NO_3)_3$, $Fe(ClO_4)_3$ was used for preparation. For more details on the synthesis of this complex see [83, 85].

8.3 Experiment and normal mode analysis

NIS experiments were performed at the nuclear resonance beamline ID18 of the European Synchrotron Radiation Facility (ESRF) in Grenoble, with an energy bandwidth of 1.1 meV($= 8.9$ cm^{-1}). The unenriched crystalline sample is scanned at 3 s per point with a total of 36 scans. Each scan consists of 500 data points. In order to minimize multiphonon contributions measurements were performed at cryogenic temperature. According to a detailed balance calculation in the spectral features

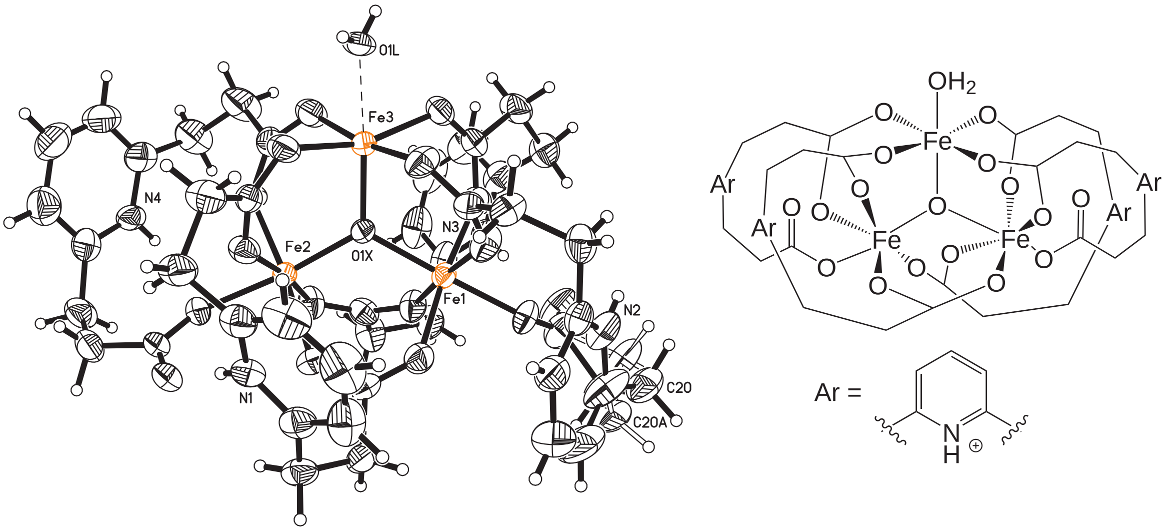

Figure 8.1: Molecular structure (left) and simplified bond structure (right) of the trinuclear complex [83]. Selected interatomic distances (Å): Fe1−Fe2 3.36, Fe2−Fe3 3.37, Fe1−Fe3 3.44, Fe1−O=Fe3−O 1.99 and Fe2−O 1.89. The perchlorate anion is not shown.

between 1.5–5.5 meV, the sample temperature was determined to be 26.5 K. Data analysis was carried out using the Fortran code DOS V2.1 [60]. A ^{57}Fe transmission Mössbauer spectrum was measured at RT using a conventional constant-acceleration spectrometer equipped with a gas proportional counter and a ^{57}Co/Rh source. This spectrum was measured using the spectrometer as discussed in chapter 3.

Raman measurements were carried out at RT using a Horiba Jobin Yvon confocal Raman spectrometer HR-800. This spectrometer is equipped with a 614 nm He-Ne laser that operates at 20 mW. A CCD camera has been used to measure the backscattered Raman signal of the complex. The laser is linearly polarized. In order to get a good signal to noise ratio of the Raman spectra, the dimension of the confocal hole and the entrance slit were fixed for all measurements at 300 and 200 μm, respectively. The objective of the microscope Olympus was a 50× with a numerical aperture of 0.45 which is able to focus on the sample in a spot around 8 μm. A total of two scans were performed on the sample and one is presented in this chapter.

Normal mode analysis was carried out using the Gaussian 03 package with the B3LYP hybrid functional. In the spin unrestricted calculation, the spin state of each Fe was taken as $S = 5/2$ with a total multiplicity of the cluster of $16 (= 2S_{\text{tot}} + 1)$. The total charge of the molecule was taken to be +3. For further details of optimization, frequency calculations and basis sets, see section 7.4 of chapter 7.

8.4 Results and discussion

8.4.1 NIS and DFT analysis

The core structure can be well described as a central planar Fe_3O unit with three planar FeO_4 units perpendicular to the Fe−O-bonds of the Fe_3O. Each of the Fe atoms is coordinated octahedrally by six O atoms, four of them are provided by the carboxylic acid groups of the ligand, the fifth O is the common central ion of the Fe_3O unit. For two of the Fe centers the sixth O is also provided by carboxylic ligand groups, but for the third Fe the sixth position is occupied by a H_2O molecule. This renders one of the three Fe centers slightly different from the other two.

The Mössbauer spectrum of the complex at RT shown in fig. 8.2 consists of an asymmetric broadened quadrupole doublet indicating the existence of two quadrupole doublets. Initial attempts to fit with two quadrupole doublets with isomer shift δ,

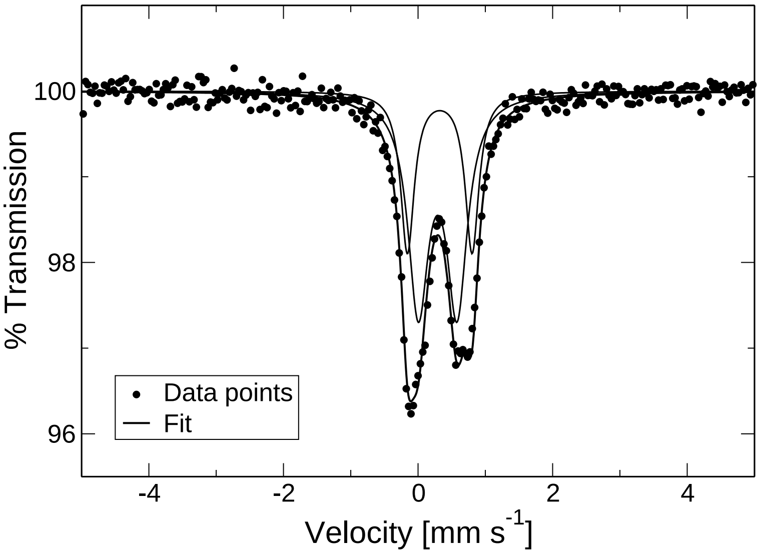

Figure 8.2: Mössbauer spectrum of the trinuclear iron complex at RT [115].

quadrupole splitting ΔE_Q, line width Γ and area ratios as free variables gave an area ratio far from the theoretically expected value of $2:1$ [113]. Hence we fixed the area ratio as $2:1$ (area ratio of inner doublet to outer doublet). A good fit is shown in fig. 8.2 and Mössbauer parameters in table 8.1.

The Mössbauer parameters are consistent with Fe(III) high-spin (HS) ($S = 5/2$) with O- and N-donor ligands [114]. At 80 K, δ increases slightly, which is due to the second-order Doppler effect. The outer doublet, which has a lower weight by area is attributed to the single Fe, which is coordinated to a H_2O molecule. The other two Fe sites, which are equivalent by coordination, can then be collectively attributed to the inner doublet with large area. While the doublet structure is in agreement with the expectation for inequivalent Fe sites and the isomer shift is typical for Fe(III), the asymmetry is an immediate consequence of the inequivalence of the three Fe centers.

In contrast to the Mössbauer studies, which revealed the spin state of the individual iron atom in this complex to be $S = 5/2$, magnetic and electron paramagnetic resonance (EPR) measurements on the same complex as reported by Rabe et al. [83] revealed that the spin state of the coupled Fe_3O cluster seems to have a spin $S = 1/2$ doublet ground state. The magnetic susceptibility data show moderate antiferromagnetic coupling yielding a $S = 1/2$ doublet ground state with 1.6% of a $S = 5/2$ paramagnetic impurity [83]. The spin concentration calculations based on

Table 8.1: Mössbauer parameters for trinuclear complex.

	Doublets	δ^a [mm s^{-1}]	ΔE_Q [mm s^{-1}]	Γ [mm s^{-1}]	Area [%]
At RT	Inner	0.40 ± 0.01	0.58 ± 0.01	0.37 ± 0.03	67 (fixed)
	Outer	0.43 ± 0.01	0.96 ± 0.01	0.25 ± 0.03	33 (fixed)
At 80 K^b	Inner	0.51 ± 0.01	0.60 ± 0.03	0.41 ± 0.02	64
	Outer	0.54 ± 0.01	1.03 ± 0.03	0.32 ± 0.02	36

^{a}Relative to α-Fe foil at RT.
^{b}80 K Mössbauer parameters are from [83].

EPR measurements in the temperature range 4–25 K, favours the doublet ground state [83]. The interatomic distances between the iron atoms are larger than 3 Å, hence, the antiferromagnetic coupling occurs primarily via superexchange mechanism through bridging ligands [116]. At a very low temperature, the metal triangle Fe_3O is significantly distorted from its equilateral geometry and forms an isosceles triangle [86]. Furthermore, on increasing the temperature from 4 to 25 K, the intensities of the EPR peaks decrease and are slightly broadened, which confirms that the isosceles geometry approaches an equilateral Fe_3O.

The ^{57}Fe vibrational density of states (VDOS) extracted from the NIS spectrum of the trinuclear complex, together with the DFT calculated VDOS, is shown in fig. 8.3. The experimental VDOS is reasonably fitted using 24 Lorentzian profiles, allowing the line width, peak position and height of all Lorentzian functions to vary freely. The mode composition factor e_j^2 of each vibrational mode is determined from the area of each peak according to eq. (7.4). The NIS and DFT-predicted wavenumbers are listed in table 8.2. Using eq. (7.2), the acoustic mode composition factor e_{ac}^2 is 0.12 (molecular mass from crystal data is 1438.80 u) and the integral area of the VDOS $g(E)$ reaches this value at $\sim$101 cm^{-1}. Hence, the spectral region up to 101 cm^{-1} should be assigned to acoustic vibrations. Particularly, the peaks at 30 and 52 cm^{-1} are attributed to acoustic modes. However, in this region a tiny band at 85 cm^{-1} is seen which could be due to librational modes. The DFT calculations were performed on a single molecule, therefore, in this region the peaks originate from librational or framework vibrational modes mostly from ligands. According to eq. (7.3) the

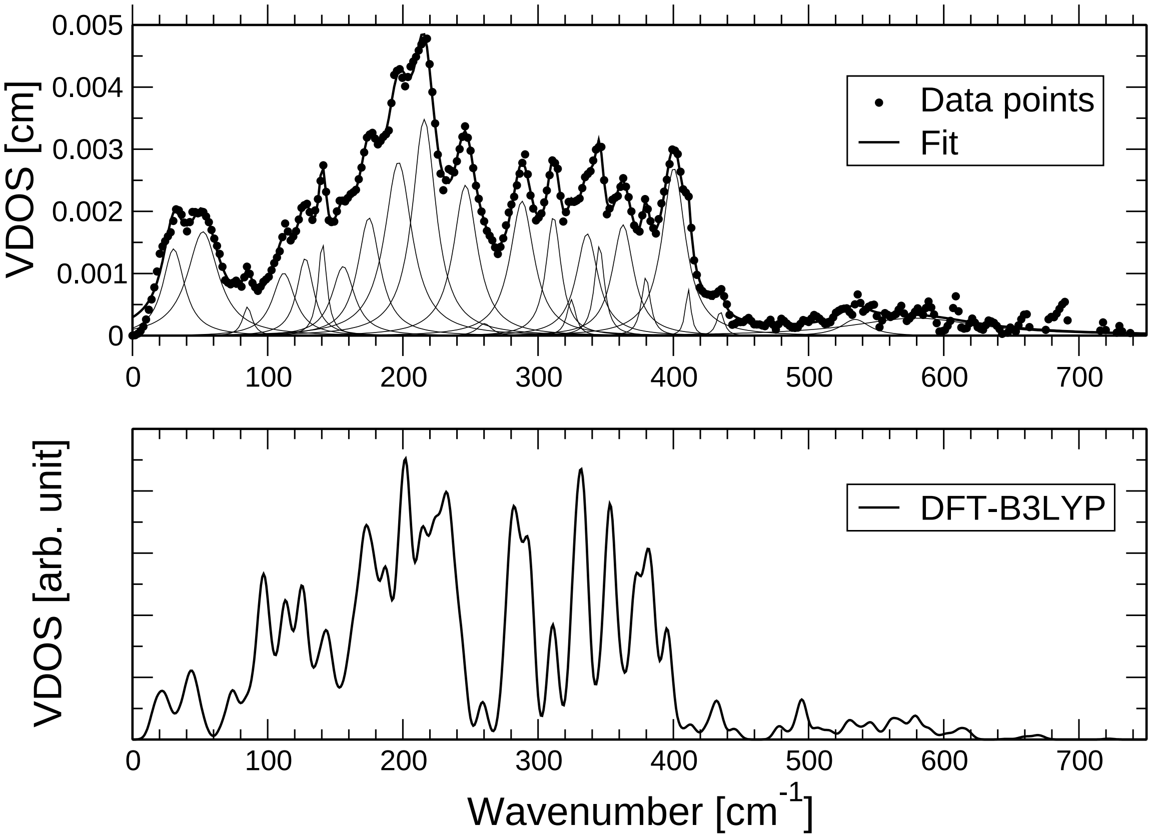

Figure 8.3: Experimental ^{57}Fe VDOS of the trinuclear iron complex at 20 K. The thin curves represent the results of a fit of the VDOS to a series of Lorentzian peaks. The DFT calculated VDOS for an isolated ion (bottom).

maximum possible mode composition factor e^2_{max} for this molecule is 0.96, which is almost equal to that of the two complexes studied in chapter 7.

In table 8.2, the summary of all the experimentally resolved iron vibrational wavenumbers, together with DFT predicted ones, is given. Only the vibrational wavenumbers that have significant iron displacement are given in the DFT predicted wavenumbers. For simplicity, the vibrational band assignments and mode description in table 8.2 were done on considering only the Fe_3O cluster which is in a local D_{3h} symmetry. As it was already shown in chapter 7, DFT predicts several modes for each experimentally resolved peak. Since most of the assignment of iron vibrational modes are tabulated, some relevant modes will be discussed further.

Table 8.2: Summary of NIS and calculated vibrational wavenumbers of trinuclear iron complex.

NIS [cm^{-1}]	e_j^2	DFT [cm^{-1}]	rmsd^a [Å]	Mode description according to fig. B.1
30	0.13	—	—	lattice modes
52	0.22			
85	0.02	83.5	0.14	librational modes
		89.7	0.12	
112	0.10	110.6	0.14	E', E'' ($\nu_6+\nu_9$)
		113.5	0.11	E' (ν_2)
		114.0	0.21	E' ν_2
128	0.09	123.4	0.12	A_2' (ν_7)
		125.7	0.15	E'' (ν_9)
		126.7	0.19	E' (ν_2)
140	0.05	137.2	0.12	E' (ν_6)
		142.1	0.12	E' (ν_5)
		144.0	0.12	E', E'' ($\nu_3+\nu_9$)
		146.4	0.09	E' (ν_3)
156	0.11	152.7	0.10	E' (ν_3)
		155.9	0.05	E' (ν_2)
		158.5	0.07	A_2'' (ν_4)
		160.3	0.08	E' (ν_2)
		163.5	0.11	E' (ν_2)
175	0.18	165.7	0.16	E' (ν_2)
		171.1	0.21	E'' (ν_9)
		172.9	0.16	E' (ν_2)
		177.9	0.18	E' (ν_2)
		179.4	0.16	E'' (ν_8)
		185.6	0.21	A_2' (ν_7)
197	0.32	188.3	0.28	A_2' (ν_7)
		197.0	0.29	A_2' (ν_7)

continued on next page...

Table 8.2 continued from previous page

NIS [cm^{-1}]	e_j^2	DFT [cm^{-1}]	rmsd^a [Å]	Mode description according to fig. B.1
		202.0	0.19	A_2' (ν_7)
		203.2	0.39	A_2' (ν_7)
216	0.35	210.8	0.26	A_2' (ν_7)
		213.7	0.18	E' (ν_2)
		216.2	0.27	E' (ν_2)
		222.0	0.20	E'' (ν_9)
		223.7	0.26	E' (ν_2)
		228.9	0.20	E', E'' ($\nu_8+\nu_2$)
246	0.25	232.3	0.19	E', E'' ($\nu_3+\nu_9$)
		234.5	0.23	E' (ν_2)
		238.8	0.17	E' (ν_2)
		243.9	0.18	A_1' (ν_1)
260	0.01	258.9	0.10	A_1' (ν_1)
288	0.22	279.8	0.22	E', E'' ($\nu_9+\nu_3$)
		282.6	0.16	E' (ν_5)
		286.3	0.21	E', E'' ($\nu_2+\nu_9$)
		289.7	0.10	A_2'' (ν_4)
		291.8	0.15	A_2'' (ν_4)
		294.1	0.22	E' (ν_2)
311	0.12	310.1	0.16	E' (ν_2)
		312.9	0.09	E' (ν_5)
325	0.02	326.1	0.19	E' (ν_2)
		331.1	0.25	E' (ν_6)
336	0.15	335.3	0.24	A_1' (ν_1)
345	0.06	346.3	0.14	A_2'' (ν_4)
		352.0	0.23	A_2'' (ν_4)
		354.7	0.24	A_2'' (ν_4)
363	0.16	362.0	0.15	A_2'', E' ($\nu_4+\nu_5$)
		371.8	0.26	E' (ν_3)

continued on next page…

Table 8.2 continued from previous page

NIS [cm^{-1}]	e_j^2	DFT [cm^{-1}]	rmsd^a [Å]	Mode description according to fig. B.1
380	0.04	378.8	0.15	A_2'', E' $(\nu_6 + \nu_4)$
		381.6	0.13	E' (ν_2)
		384.6	0.17	E' (ν_4)
400	0.27	395.4	0.18	E' (ν_2)
		403.6	0.04	E' (ν_3)
411	0.02	412.8	0.05	E' (ν_3)
435	0.01	433.7	0.05	E' (ν_3)
534	0.03	530.6	0.06	E' (ν_3), Fe3$-$O$_{\mu\text{-oxo}}$ stretch
		530.8	0.04	E' (ν_2)
		537.6	0.04	E' (ν_3), Fe3$-$O$_{\mu\text{-oxo}}$ stretch
579	0.16	This region suffers from poor statistics, hence not assigned.		

^{a} Sum of the root mean square displacements of the three Fe atoms obtained from calculation.

The highest peak in the experimental VDOS is seen at ~200 cm^{-1}, which consists of two bands, 197 and 216 cm^{-1}. The band at 197 cm^{-1} consists of four A_2' (ν_7) modes of vibration as suggested by DFT, see table 8.2. Since in NIS the highest peak has the largest Fe vibrational displacement, the DFT predicted band at 203.2 cm^{-1} has the largest (rmsd of 0.39 Å) of all the calculated displacements. The other bands also have the largest rmsd next to 203.2 cm^{-1} band. The next highest band at 216 cm^{-1} consists of six vibrational modes as shown by DFT and five of them are of a doubly degenerate E' type. The remaining one is of A_2', which has also significant rmsd on comparing with the others for the band at 216 cm^{-1}. In this region according to DFT prediction, the band at 228.9 cm^{-1} consists of coupled modes, E' as well as E''.

A symmetric stretch (i.e. A_1') is observed for the experimentally resolved band at 246 cm^{-1}. This band is also identified in the Raman spectrum, for details see fig. 8.4 and section 8.4.2. In this region, according to DFT the majority of the modes seem to be of E' type. This is in contrast to the previously reported value of 148 cm^{-1} [98].

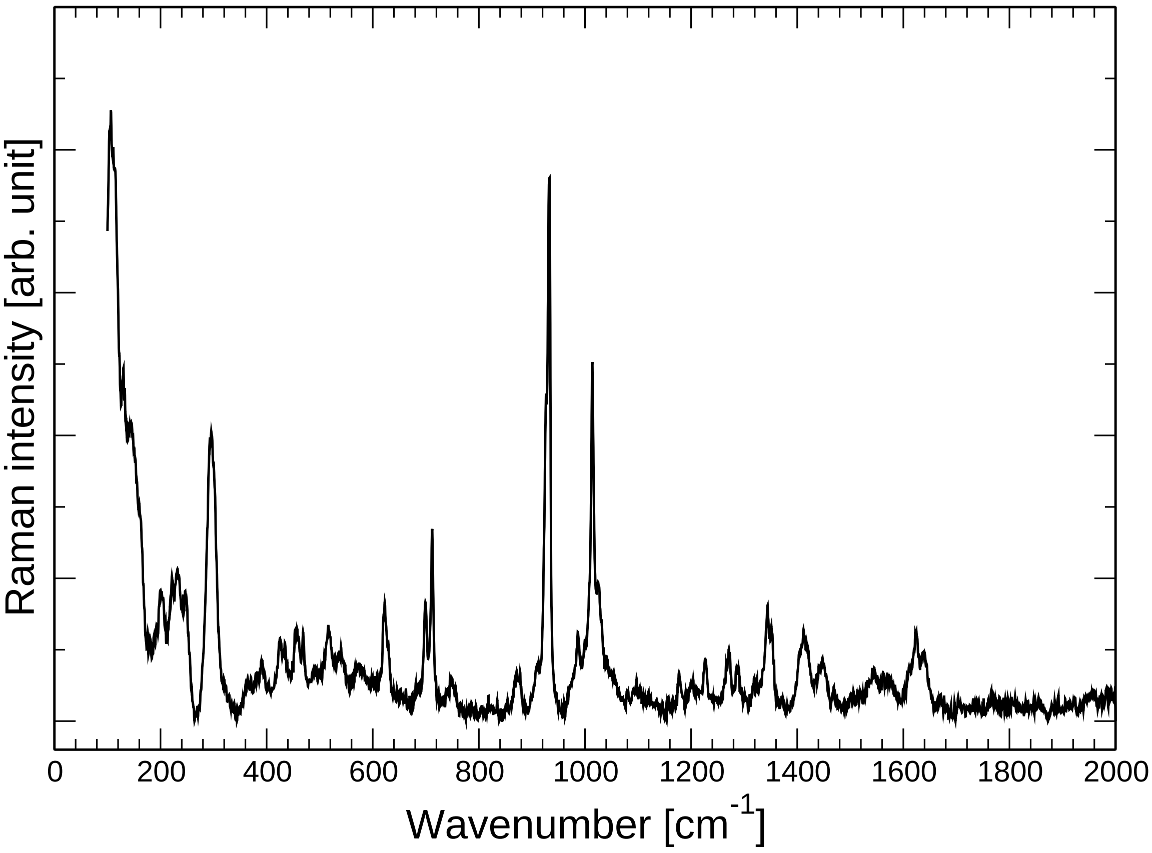

Figure 8.4: Raman spectrum of the trinuclear iron complex at RT.

One possible reason may be a different spin state with larger force constant in our complex so that excitation of the stretching mode A_1' occurs at higher frequency, as the larger ligand mass would tend to the opposite effect. However, in [98], on considering the correlation between D_{3h} and three D_{4h} symmetries the authors have observed the A_1' mode of vibrations in the range 296–346 cm^{-1} in similar complexes like ours.

A tiny band in the experimental VDOS is seen at 260 cm^{-1} accounting for the shoulder of the band at 246 cm^{-1}. A similar feature at 258.9 cm^{-1} with a rmsd of 0.10 Å is seen in the DFT computed VDOS, therefore, the band at 260 cm^{-1} is assigned to A_1'. The next A_1' mode with a somewhat larger rmsd (0.24 Å) is seen at 335.3 cm^{-1}, which is assigned to the experimentally observed band at 336 cm^{-1}.

The band at 345 cm^{-1}, according to DFT, consists of three A_2'' modes of vibration. As the A_2'' mode is Raman inactive, there is no peak around 345 cm^{-1}, see fig. 8.4. Furthermore, on considering the correlation between the three FeO$_4$ units in a D_{4h}

Table 8.3: Summary of some NIS, Raman and calculated vibrational wavenumbers of trinuclear iron complex.

Raman [cm^{-1}]	NIS [cm^{-1}]	DFT [cm^{-1}]	Mode description^a
130	128	126.7	E' (ν_2)
144	140	144.0	E', E'' ($\nu_3+\nu_9$)
222	216	222.0	E'' (ν_9)
232	—	232.3	E', E'' ($\nu_3+\nu_9$)
246	246	243.9	A_1' (ν_1)
296	—	294.1	E' (ν_2)
391	400	395.4	E' (ν_2)
699, 712	—	706.4, 715.1, 716.4	in-plane deformation of pyridine
930	—	941.6, 941.7, 942.7	twisting of CH in pyridine
1014	—	1012.3	in-plane deformation of pyridine
1347	—	1348.9, 1349.8	C−C stretch of alkyl spacer
1624	—	1625.3	A_1 (bend) species of H_2O in C_{2v}

[a] According to fig. B.1 of appendix B, otherwise specified.

symmetry and Fe_3O in a D_{3h} symmetry, the A_2'' of D_{3h} gives E_u of D_{4h} (table B.1 of appendix B). This E_u mode of vibration is also Raman inactive.

In the high-frequency region above ∼400 cm^{-1}, all modes seem to consist of E' vibrations. In addition, the iron displacements are feeble with rmsd less than 0.10 Å as expected. For the band at 534 cm^{-1} DFT predicts three modes, and out of these three modes two modes seem to have a large $O_{\mu\text{-oxo}}$ vibrational displacement.

8.4.2 Raman analysis

The Raman spectrum of the trinuclear iron complex is shown in fig. 8.4. Because of the highly complex structure of the molecule considered, it is tedious to assign all the peaks observed in the spectrum using the optical selection rule of Raman shifts. Therefore some of the normal modes of vibration of the observed band are assigned using DFT. Some vibrational wavenumbers obtained from Raman and NIS together with DFT predicted ones are given in table 8.3. In NIS, the band at 246 cm^{-1} was assigned to A_1'. As this mode is Raman active, a similar band at 246 cm^{-1} is also observed in the Raman spectrum and confirms the assignment.

By direct comparison of the Raman spectrum with DFT, the strong band at 296 cm^{-1} is assigned to E'. This band is also seen in other trinuclear complexes (iron and chromium) as reported in [98, 117]. These authors have considered the correlation of the vibrational modes of the three planar FeO_4 (D_{4h}) units interacting under the central FeO_3 (D_{3h}) unit, assigned this band to A_{1g} of the D_{4h} symmetry. It should be noted that the A_{1g} mode can be related to E' and A_1' (see correlation table B.1 of appendix B). In our case, this band is found to be E' mode. Furthermore, in [98] a band at 302 cm^{-1} is assigned to A_{1g} mode of the three FeO_4 units. The vibrations associated with the ligands and pyridine rings appear in the high-energy region as expected. Some of them are identified using DFT and listed in table 8.3.

8.5 Conclusions

Vibrational dynamics of a novel trinuclear oxobridged iron complex is studied by NIS and Raman spectroscopy. Some of the bands have been assigned using DFT. Mössbauer spectroscopy at RT as well as at 80 K reveals that the individual spins of the Fe atoms are HS with $S = 5/2$ with an oxidation state of +3. Furthermore, according to EPR and magnetic studies at less than 25 K reveal that there is slight antiferromatnetic coupling between the three iron leading to a ground state doublet ($S = 1/2$) which is due to the fact that at very low temperatures, the equilateral triangular Fe_3O unit distorts to an isosceles triangle which means that the three coupling constants of three Fe atoms reduces to two coupling constants because of antiferromagnetic interaction.

Chapter 9

Summary and outlook

Iron is one of the most common elements on earth and is found in nearly all living organisms. It is known for its important biological role and ideally suited for catalyzing many reactions that use molecular oxygen. Iron containing proteins and enzymes are responsible for mediating redox reactions, electron transport and dioxygen transport/storage and nitrogen fixation. In many heme- and nonheme-based metalloenzymes which contain metal centers as iron, the oxidation of organic substances occurs in the presence of molecular oxygen. The understanding of how these oxidation reactions proceed, including the intermediates formed in the selective oxidation, is currently a major challenge. Furthermore, the vibrational dynamics of iron in the catalyst itself plays an important role in revealing the reactivity of active sites that may mediate oxidation.

This dissertation is focussed on the investigation of structural and vibrational properties of some trinuclear oxobridged iron complexes and their catalytic intermediates formed under Gif-type conditions. The time dependence of the Gif reaction was also analyzed. It should be noted that reaction intermediates cannot necessarily be crystallized in our case, and the species which can be crystallized may not form a part of the catalytic cycle. Therefore a site-selective spectroscopic technique which monitors the active metal center is needed. The main experimental tools used were ^{57}Fe transmission Mössbauer spectroscopy and synchrotron-based nuclear inelastic scattering (NIS). All liquid samples that are sensitive to air were prepared under inert atmosphere, quickly frozen in liquid nitrogen and measured at 4.2 K for Mössbauer measurements and at $\sim$20 or 70 K for NIS experiments. Some powder samples were also measured at room temperature (RT). To analyze the NIS data, normal mode analysis based on quantum mechanical calculations using density functional theory (DFT) was done. Since NIS is rarely applied to the investigation of homogenous reactions catalyzed by transition-metal complexes, we first studied the Michael reaction as a test case. The intermediate formed in the Michael reaction is a monomer iron complex with two acetylacetonate groups bonded bidentally to the iron atom. The other two iron sites are coordinated to water molecules and the whole monomer structure appears to form a facial stereochemistry arrangement.

Besides the research work presented in this thesis, instrumentation details of a RT ^{57}Fe transmission Mössbauer spectrometer were also discussed. This instrumentation is based on the experience which was acquired while constructing the spectrometer during this dissertation. In this part the calibration and safety aspects of the spectrometer, with an in-depth analysis of count rates and resolution of the measured spectra were discussed.

Mössbauer spectroscopy reveals that the iron atoms in the trinuclear oxobridged iron complexes are high-spin (HS) ($S = 5/2$) Fe(III) ions. The complex breaks up into the monomers when it is dissolved in pyridine, and the spectrum displays a complex broadened pattern due to slow paramagnetic relaxation. This broadening is even more pronounced on adding acetic acid. For the active catalyst (under inert gas), i.e. the complex dissolved in a mixture of pyridine, acetic acid and metallic zinc, the spectrum displays a prominent doublet, which is consistent with a HS Fe(II) species. On exposing the active catalyst to molecular oxygen, a new HS Fe(III) species is formed together with the HS Fe(II) doublet. This newly formed Fe(III) species shows a larger quadrupole splitting than that of the complex. The Gif reaction at zero time shows similar spectral parameters as that of the active catalyst under inert gas. After 1 min of the Gif reaction, there is no significant change from that at zero time. The spectrum of the Gif reaction after 5 min displays two doublets, which confirms the presence of both Fe(II) and Fe(III) species. The Mössbauer parameters of this Fe(III) species are almost the same as those of the active catalyst exposed to molecular oxygen. After 30 min, the intensity of this Fe(III) doublet is more pronounced.

NIS investigations were performed on trinuclear iron catalysts and their frozen solutions in a similar order as in the Mössbauer experiments, but the starting material anhydrous ferrous nitrate is enriched in ^{57}Fe. All samples were discussed in terms of ^{57}Fe vibrational density of states (VDOS) and force constants extracted from the NIS spectra. In NIS, two oxobridged iron complexes with different lengths of the carbon chain were compared. Moreover, the DFT calculated VDOS of the core of the trinuclear complex qualitatively matches the experimental VDOS of both the complexes. From the observation of NIS and DFT, the VDOS of the core is not affected by varying the length of the alkyl chain. The experimental VDOS of the intermediate (monomer 1, complex dissolved in pyridine) is in agreement with the DFT predicted VDOS of a simple model complex. This analysis reveals that in this monomer iron is bidentally bonded to two acetate groups and the other iron sites are coordinated to two pyridine ligands. On adding acetic acid, the NIS spectrum is broadened but shows somewhat similar features as the monomer 1. The NIS spectrum of the active catalyst (monomer 2, complex dissolved in a mixture of pyridine, acetic acid and metallic zinc) under inert gas is in good agreement with the DFT predicted VDOS of a model complex. The molecular structure of the active catalyst is in accord with a structure similar to ours reported in the literature [104]. To get a deeper understanding, force constant analysis of the iron in the monomer was also done. NIS on the Gif reaction at zero time shows a similar spectrum as that of the active catalyst under inert gas. From this we conclude that the species found in the active catalyst and the Gif reaction at zero time seems to be responsible for the initial activation of the carbon-hydrogen bond of the substrate.

A complete analysis of the ^{57}Fe vibrational dynamics of a novel crystalline trinuclear oxobridged iron compound is obtained by NIS. Mössbauer spectroscopy shows that two of the three iron sites were in similar coordination as shown in an X-ray crystallographic structure determination. The oxidation and spin state determined by Mössbauer spectroscopy was used for the normal mode analysis based on DFT for assigning some vibrational bands obtained from NIS and Raman spectroscopy.

The work presented in this dissertation gives a better understanding of the Gif oxidation and the intermediates formed in such reaction. In this reaction, monitoring the changes around the active metal center is of crucial importance. Therefore, an experimental tool that tracks only the iron atom is needed, and the results obtained from such a tool would offer an advantage over those obtained with non-selective experimental methods. NIS is such a technique that senses only the vibrational dynamics of the iron atom. Although NIS is not yet used extensively in the field of homogeneous catalysis, it offers a good possibility to follow the catalytic active center of the chemical reactions and to understand the molecular structure of the intermediate species. Iron compounds are nowadays widely investigated by NIS (which can also be applied to compounds containing tin, europium, samarium, dysprosium, and others). For the Gif system considered in this dissertation, the catalytic intermediate is slightly different from the structure reported in [104] where the Gif system is similar to ours. The structure of the active catalyst is almost the same as in [104], but the orientation of one pyridine ring is slightly different. To interpret the NIS data, quantum mechanical calculations based on DFT method were applied. Despite the advantages, NIS has its own limitations: isotopic enrichment is required to obtain a NIS spectrum in short time (∼4 h) and one needs a highly sophisticated experimental setup. At present, NIS is rountenly performed only at three places such as ESRF in France, Advanced Photon Source (APS) at Argonne National Laboratory in USA, and Super Photon Ring-8 Gev (SPring-8) in Japan. Therefore, obtaining beamtime is very difficult. Some other places to our knowledge are the Photon Factory (KEK) in Japan, and HASYLAB in Germany.

Finally, the investigation of Gif oxidation of organic substrates in the presence of molecular oxygen using transition metals is increasingly interesting in the light of potential industrial applications. Besides the investigation of the intermediates of the Gif oxidation using iron complexes, the vibrational dynamics of the iron (generally occurring below 500 cm^{-1}) is important for understanding electron transfer processes. The research efforts/results presented in this dissertation will add knowledge in predicting intermediates, and obtaining the complete vibrational dynamics of a specific atom, i.e. of Mössbauer nuclei in more complex compounds and therefore provide a insight in selective oxidation as well as catalytic reaction processes.

Chapter 10

Zusammenfassung und Ausblick

Eisen ist eines der verbreitetsten Elemente auf der Erde und in nahezu allen lebenden Organismen zu finden. Eisen ist für seine wichtige biologische Rolle bekannt und wird zudem gerne als Katalysator bei vielen Reaktionen, vornehmlich mit molekularem Sauerstoff eingesetzt. Eisen enthaltende Proteine und Enzyme spielen eine wesentliche Rolle in Redox-Reaktionen, bei Elektronentransport, Sauerstofftransport, Speicherung und Stickstofffixierung. In vielen häm- und nichthämbasierten Metalloenzymen welche Eisen als Zentralatom enthalten, ist eine Oxidation von organischen Substanzen in Anwesenheit von molekularem Sauerstoff möglich. Das Verständnis dieser Reaktionen, vor allem die Aufklärung der Intermediate der selektiven Oxidation, stellt immer noch eine große Herausforderung dar. Die Schwingungsdynamik des Eisens im Katalysator spielt eine wichtige Rolle in der Aktivierung der zu oxidierenden Spezies.

Diese Arbeit ist auf die Untersuchung der strukturellen und Schwingungs-Eigenschaften einiger trinuklearer sauerstoffüberbrückten Eisenkomplexe und deren katalytischen Zwischenspezies, gebildet unter Gif-Typ Reaktionen, fokussiert. Die Zeitabhängigkeit der Gif Reaktion wurde ebenfalls analysiert. Ein Nachteil der Untersuchung stellte die Tatsache dar, dass nicht alle Intermediate kristallisiert werden konnten bzw. teilweise nur Spezies kristallisiert werden konnten, die nicht unbedingt an dem katalytischen Zyklus beteiligt waren. Deswegen war eine spektroskopische Untersuchungsmethode gefragt, welche das aktive Metallzentrum ‚überwacht‘. Hier bieten sich die ^{57}Fe Mößbauerspektroskopie und die auf Synchrotronstrahlung basierende nukleare inelastische Streuung (NIS) an. Alle luftempfindlichen, flüssigen Proben wurden unter Inertgasatmosphäre hergestellt, rapide mit flüssigem Stickstoff gekühlt und bei 4.2 K Mößbauermessungen bzw. bei ∼20 oder 70 K NIS Experimenten unterzogen. Einige Pulverproben wurden zusätzlich bei Raumtemperatur (RT) untersucht. Die Daten der NIS Messungen wurden basierend auf quanten mechanischen Rechnungen nach der Dichtefunktionaltheorie (DFT) analysiert. Da die NIS-Methode selten zur Untersuchung von homogenen Reaktionen, katalysiert durch Übergangsmetallkomplexe verwendet wird, wurde als erstes eine Michael-Reaktion zum Test der Methode verwendet. Das Intermediat einer Michael-Reaktion ist ein monomerer Eisenkomplex mit zwei zweizähnigen an Eisen gebundenen Acetyeacetonat-Gruppen. Zwei weitere Koordinationsstellen sind durch Wassermoleküle belegt. Das gesamte Monomer zeigt eine faciale Sterochemie.

Neben den experimentellen Untersuchungen werden in dieser Arbeit messtechnische Details eines RT ^{57}Fe Transmissions-Mößbauerspektrometers diskutiert. Der Aufbau des Spektrometers war ebenfalls Teil dieser Arbeit. Neben der ausführlichen Beschreibung der Datenanalyse werden experimentelle Details wie Kalibrierung, Sicherheitsaspekte im Umgang mit dem Spektrometer sowie die Auflösung der Spektren in der Arbeit diskutiert.

Die Mößbauerspektroskopie macht sich zu Nutze, dass die Eisen Atome im dreikernigen sauerstoffüberbrückten Eisenkomplex als high-spin (HS) ($S = 5/2$) Fe(III) Ionen vorliegen. Der mehrkernige Komplex zerfällt in Pyridin gelöst zum einkernigen, monomeren und das Spektrum zeigt ein breites Muster, verursacht durch eine langsame paramagnetische Relaxation. Diese Verbreiterung wird stärker sobald Essigsäure hinzugefügt wird. Für den aktivierten Katalysator (unter Schutzgas), also den Komplex aufgelöst in einer Mischung aus Pyridin, Essigsäure und metallischem Zink, zeigt das Spektrum ein deutliches Dublett, welches einer HS Fe(II) Spezies entspricht. Wird der Katalysator nun molekularem Sauerstoff ausgesetzt, so erscheint eine neue HS Fe(III) Spezies, neben dem HS Fe(II) Dublett. Diese neue Fe(III) Spezies zeigt eine größere Quadrupol-Aufspaltung als der ursprüngliche Komplex. Die Gif-Reaktion zeigt zum Zeitpunkt Null ähnliche spektroskopische Charakteristika wie der aktivierte Komplex in Schutzgasatmosphäre. Eine Minute nach dem Start der Gif-Reaktion ist kein signifikanter Unterschied zu sehen. Das Spektrum nach 5 Minuten Gif-Reaktion zeigt zwei Dubletts, welche die Anwesenheit von Fe(II) und Fe(III) bestätigt. Die Mößbauer Parameter der Fe(III) Spezies sind nahezu dieselben wie die nach der Aussetzung des Komplexes an molekularen Sauerstoff. Nach 30 Minuten ist die Intensität des Fe(III) Dubletts wesentlich ausgeprägter.

NIS Untersuchungen wurden an dreikernigen Eisenkomplexen und deren eingefrorenen Lösungen analog zu den Mößbauer Experimenten durchgeführt, allerdings wurde die Ausgangssubstanz (wasserfreies Eisennitrat) mit ^{57}Fe angereichert. Alle Ergebnisse werden in Bezug gesetzt zur Schwingungszustandsdichte des ^{57}Fe (VDOS) und zu Kraftkonstanten die aus den NIS Spektren extrahiert wurden. Mit NIS wurden zwei Sauerstoffüberbrückte Eisenkomplexe mit unterschiedlicher Kohlenstoffkette verglichen. Die mit der DFT Methode berechneten Zustandsdichten der Kerne der trinuklearen Komplexe stimmen qualitativ mit den experimentell bestimmten Zustandsdichten überein. Aus den Beobachtungen der NIS Messungen und den DFT Rechnungen kann die Schlussfolgerung gezogen werden, dass die Zustandsdichte der Kerne unabhängig von der Länge der Alkylkette ist. Die experimentelle VDOS des Intermediats (Monomer 1, Komplex aufgelöst in Pyridin) stimmt mit den DFT Rechnungen für einen einfachen Modellkomplex überein. Die Datenanalyse zeigt, dass in diesem Monomer das Eisen zweizähnig an zwei Acetat-Gruppen gebunden ist, während zwei weitere Koordinationsplätze von zwei Pyridinmolekülen eingenommen werden. Wird Essigsäure hinzugefügt, so wird das NIS Spektrum breiter, zeigt aber ähnliche Merkmale wie das Monomer 1. Das NIS Spektrum des aktivierten Katalysators (Monomer 2, Komplex gelöst in einer Mischung aus Pyridin, Essigsäure und Zink) unter Schutzgas stimmt sehr gut mit dem Modell auf welchem die DFT Rechnungen basieren überein. Die molekulare Struktur des aktivierten Komplexes stimmt außerdem mit einer in der Literatur beschriebenen überein [104]. Zum besseren Verständnis wurde eine Kraftkonstantenanalyse im Monomeren durchgeführt. Da das NIS Spektrum der Gif-Reaktion beim Start (Zeitpunkt $t = 0$) ähnlich zu dem des aktivierten Komplex unter Schutzgas ist, kann daraus geschlossen werden, dass die Spezies des aktivierten Komplexes und die der Gif-Reaktion zum Zeitpunkt Null verantwortlich ist für die ursprüngliche Aktivierung der Kohlenstoff-Wasserstoff-Bindung des Substrats.

Eine komplette Analyse der Vibrationsdynamik des ^{57}Fe eines weiteren dreikernigen Sauerstoffüberbrückten Eisenkomplexes wurde aus NIS Experimenten erhalten. Die Mößbauerspektroskopie zeigt, dass zwei der drei Eisenkerne sehr ähnlich koordiniert sind. Dies wird auch durch Röntgendiffraktionsmessungen bestätigt. Die Oxidationsstufen und der Spinzustand, bestimmt durch Mößbauerexperimente, wurden in DFT Rechnungen verwendet um einige der Schwingungsbanden der NIS und Ramanuntersuchungen zuzuordnen.

Diese Arbeit leistet einen Beitrag zum besseren Verständnis der Gif-Oxidation und speziell der in der Reaktion involvierten Zwischenstufen. Um diese Reaktion zu durchleuchten, müssen die Veränderungen am aktiven Metallzentrum untersucht werden. Hier bieten sich die NIS-Technik und die Mößbauerspektroskopie als besonders empfindliche Methoden an. Mit NIS kann dabei die Schwingungsdynamik des Eisenatoms visualisiert werden. Auf dem Gebiet der homogenen Katalyse ist NIS eine relativ wenig eingesetzte Methode, obwohl NIS gute Möglichkeiten bietet, das katalytische Zentrum während einer Reaktion zu verfolgen. Bei dem hier in der Arbeit untersuchten Gif-System unterscheidet sich das katalytisch aktive Zwischenprodukt leicht von der in der Literatur beschriebenen Struktur [104]. Der Unterschied liegt in einer anderen Orientierung einer der Pyridinringe. Um die NIS Daten zu interpretieren wurden quanten mechanische Rechnungen, basierend auf der DFT durchgeführt. Neben den Vorteilen, die NIS bietet, gibt es auch zwei Nachteile: für Messungen in einem vernünftigen Zeitrahmen (∼4 Stunden) ist eine Isotopenanreicherung notwendig und der experimentelle Aufbau ist recht aufwendig. Hinzu kommt, dass die Meßzeit an den zurzeit für NIS Experimente in Frage kommenden drei Quellen (ESRF in Frankreich, Advanced Photon Source (APS) in Argonne National Lab und Super Photon Ring-8 GeV (SPring-8) in Japan) sehr beliebt und somit schwierig zu ergattern ist.

Das Verständnis der Gif-Oxidation von organischen Substanzen in Anwesenheit von molekularem Sauerstoff unter Verwendung von Übergangsmetallen als Katalysator ist von zunehmendem Interesse für industrielle Anwendungen. Neben der Untersuchung der Zwischenprodukte der Gif-Oxidation mit Eisenkomplexen kann die Schwingungsdynamik des Eisens (im Allgemeinen unterhalb von 500 cm^{-1}) dazu dienen, Elektronentransferprozesse zu verstehen. Die Ergebnisse dieser Arbeit sind hilfreich bei der Vorhersage von Reaktionszwischenprodukten, vornehmlich in Redox-Reaktionen mit molekularem Sauerstoff. Die gesamte Schwingungsdynamik eines spezifischen, Mößbauer aktiven Atoms in einem komplexen System konnte analysiert werden und zur Interpretation des oxidativen Prozesses verwendet werden. Mößbauer- und NIS-Spektroskopie bieten gemeinsam mit theoretischen Rechnungen eine gute Möglichkeit, katalytische Reaktionen zu untersuchen.

APPENDICES

Appendix A

^{57}Fe Mössbauer constants

- Half lifetime of $^{57}_{27}$Co $T_{1/2} = 271.8$ days
- Half lifetime of $^{57}_{26}$Fe $\tau_{1/2} = 98.3 \times 10^{-9}$ s
- Mean lifetime of $^{57}_{26}$Fe $\tau = \tau_{1/2}/\ln 2 = 141.8 \times 10^{-9}$ s
- Natural abundance of ^{57}Fe = 2.1%
- Energy of Mössbauer transision $E_\gamma = 14.412497$ keV
- Mass of ^{57}Fe nucleus $M = 56.9353987$ u
- Excited state $I = 3/2$ nuclear g-factor of ^{57}Fe $g_\mathrm{e} = -0.15532/(3/2)$
- Ground state $I = 1/2$ nuclear g-factor of ^{57}Fe $g_\mathrm{g} = 0.090604/(1/2)$
- Wave length, λ

$$\lambda = \frac{hc}{E_\gamma} \tag{A.1}$$

$$= \frac{4.13566733 \times 10^{-15}\ \mathrm{eV\ s} \cdot 299792458\ \mathrm{m\ s^{-1}}}{14412.497\ \mathrm{eV}} = 86.0255\ \mathrm{pm} \tag{A.2}$$

- eV and mm s^{-1} equivalence

$$E_\mathrm{D} = \frac{v E_\gamma}{c} \tag{A.3}$$

For $v = 1$ mm s^{-1}, $E_\mathrm{D} = 4.8075 \times 10^{-8}$ eV $\Longrightarrow$ 1 mm s^{-1} $= 48.075$ neV.

- Recoil energy, E_{R}

$$E_{\mathrm{R}} = \frac{(\hbar k)^2}{2M} = \frac{E_\gamma^2}{2Mc^2} \tag{A.4}$$

$$= \frac{(14412.497\ \mathrm{eV})^2}{2 \cdot \left(\frac{56.9353987}{10^3 \cdot 6.02214179 \times 10^{23}}\ \mathrm{kg}\right) \cdot (299792458\ \mathrm{m\ s^{-1}})^2} \tag{A.5}$$

$$= 1.22229 \times 10^{16}\ \mathrm{eV^2\ J^{-1}} = 1.9583\ \mathrm{meV} \tag{A.6}$$

J = kg m^2 s^{-2}; 1 eV = 1.602176487×10^{-19} J

- Natural line width, Γ_{nat}

$$\Gamma = \frac{\hbar}{\tau} = \frac{6.58211899 \times 10^{-16}\ \mathrm{eV\ s}}{141.8169 \times 10^{-9}\ \mathrm{s}} = 4.6413\ \mathrm{neV} = 0.09654\ \mathrm{mm\ s^{-1}} \tag{A.7}$$

Appendix B

Normal modes of D_{3h} and D_{4h} symmetries

Table B.1: Correlation between the normal modes of vibration of three planar D_{4h} (FeO_4 group) interacting under D_{3h} (Fe_3O group) symmetry [98].

D_{4h}	D_{3h}
A_{1g}	A_1' E'
B_{1g}	A_1' E'
A_{2u}	A_1' E'
B_{2g}	A_1'' E''
B_{2u}	A_1' E'
E_u	A_2' A_2'' E' E''

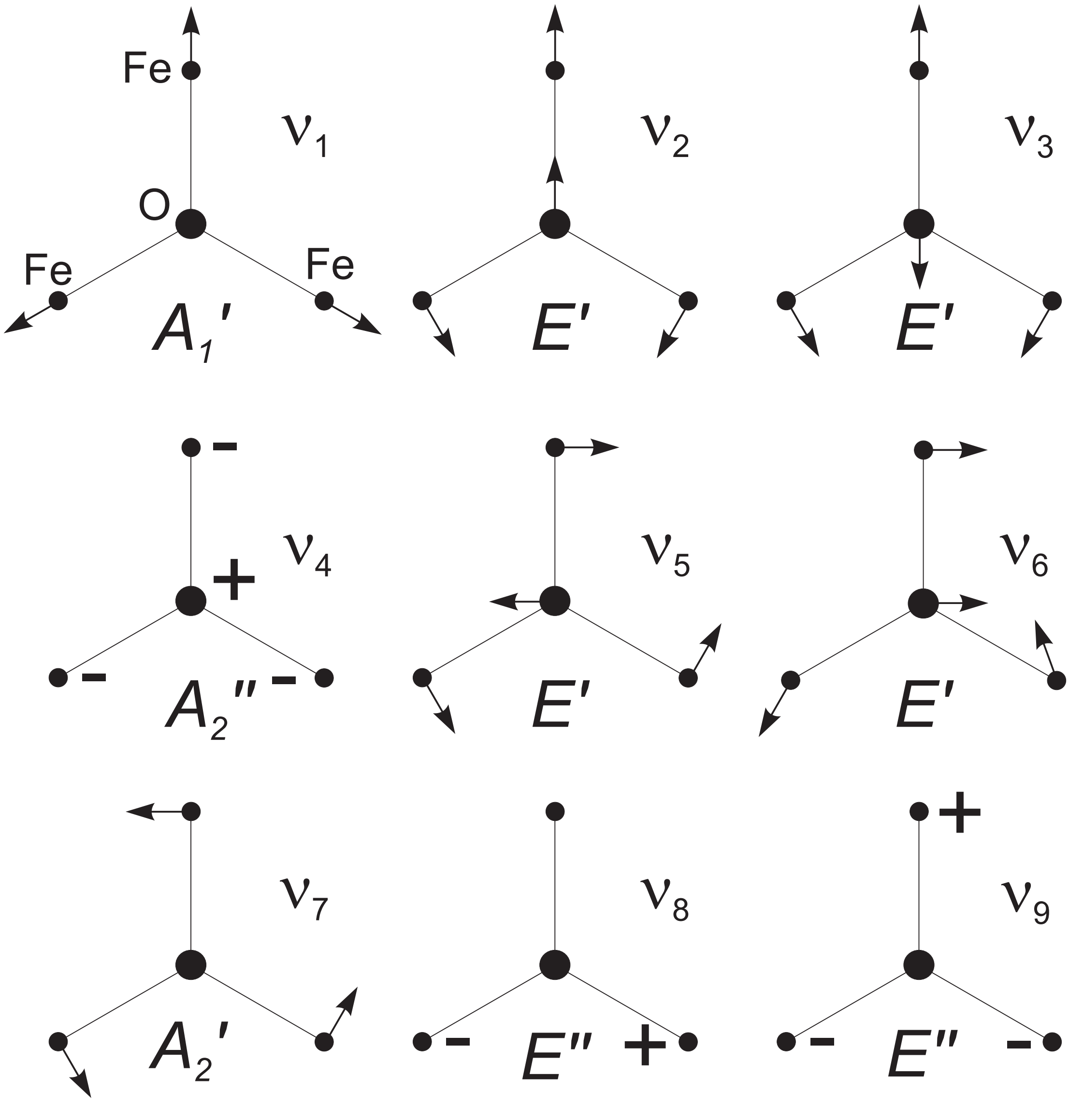

Figure B.1: Normal modes of vibration for a D_{3h} symmetry [118]. Modes shown in the first and center row are genuine molecular vibrations and the modes shown in bottom are rotational vibrations. The modes ν_2 and ν_3 are doubly degenerate and their respective partners are ν_5 and ν_6. The three translational modes are not shown. The atoms marked as " + " and " − " represents out-of-plane motions.

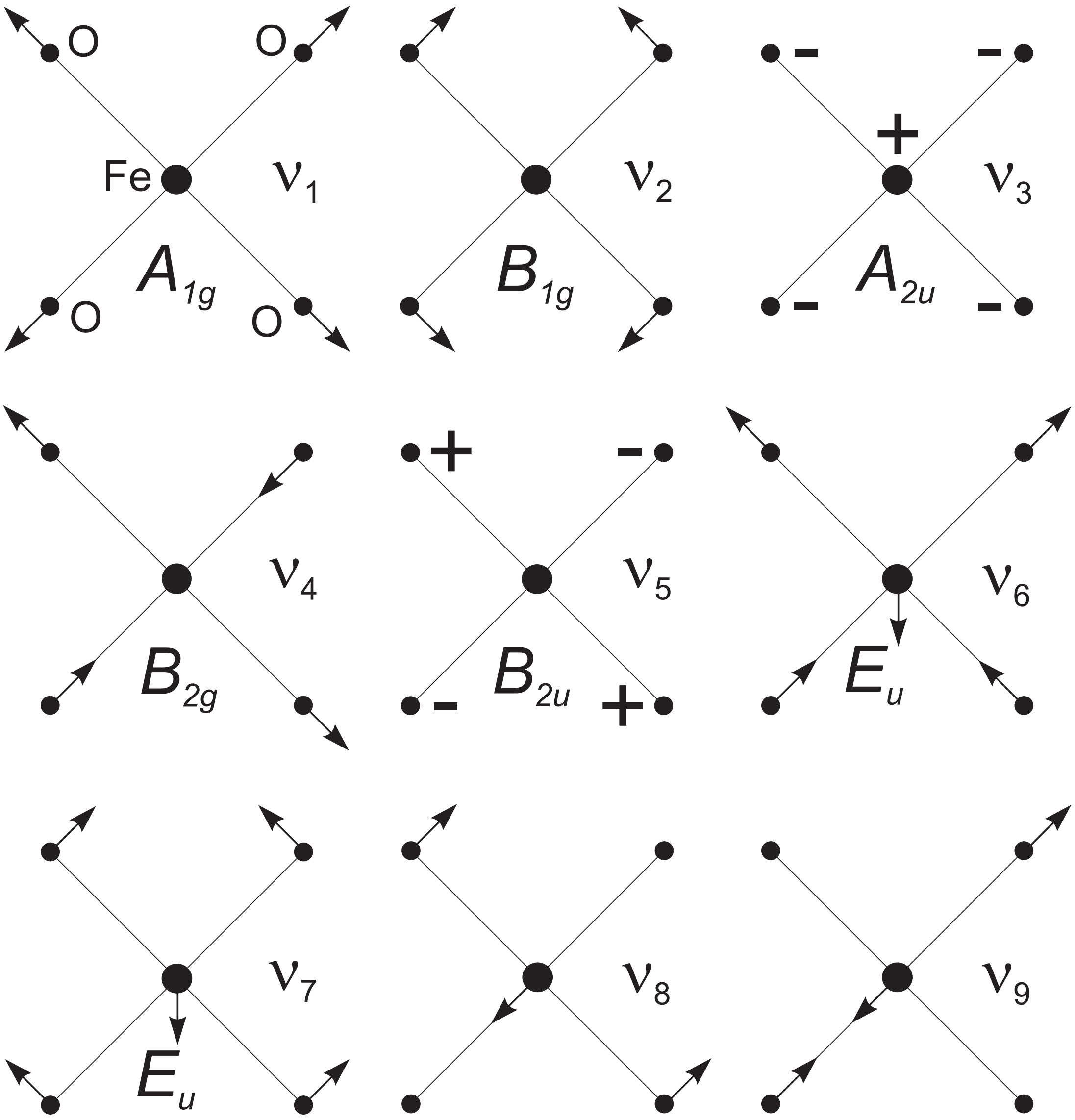
O
O
Fe
ν1
A1g
O
O
ν2
B1g
-
-
+
ν3
A2u
-
-
ν4
B2g
+
-
ν5
-
B2u
+
ν6
Eu
ν7
Eu
ν8
ν9

Figure B.2: Normal modes of vibration for a D_{4h} symmetry [75, 119]. The modes ν_6 and ν_7 are doubly degenerate and their respective partners are ν_9 and ν_8. The three translational and rotational modes are not shown. The atoms marked as " + " and " − " represents out-of-plane motions.

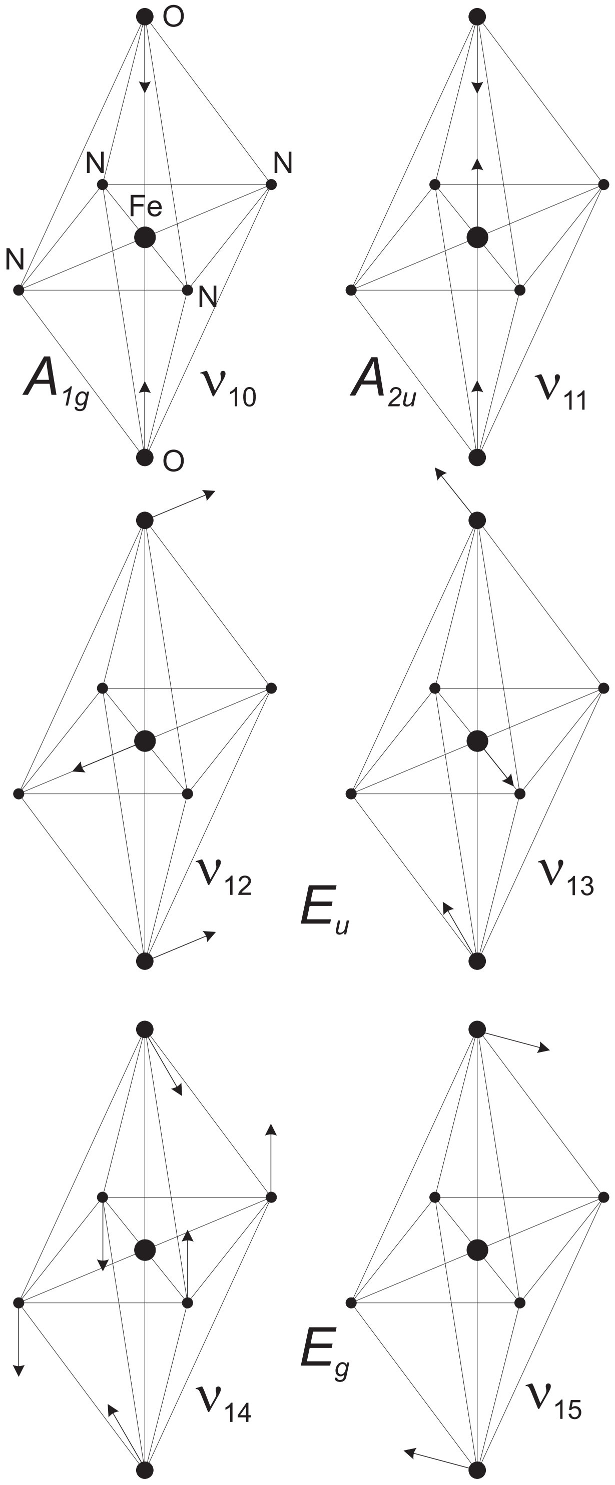
O
N
N
Fe
N
N
O
A1g
ν10
A2u
ν11
ν12
Eu
ν13
ν14
Eg
ν15

Figure B.3: Normal modes of vibration for a D_{4h} symmetry of a trans FeN_4O_2 molecule. The E_u modes displayed here are O-Fe-O bend type. The remaining nine modes are shown in fig. B.2 where the FeO_4 unit should be thought of FeN_4.

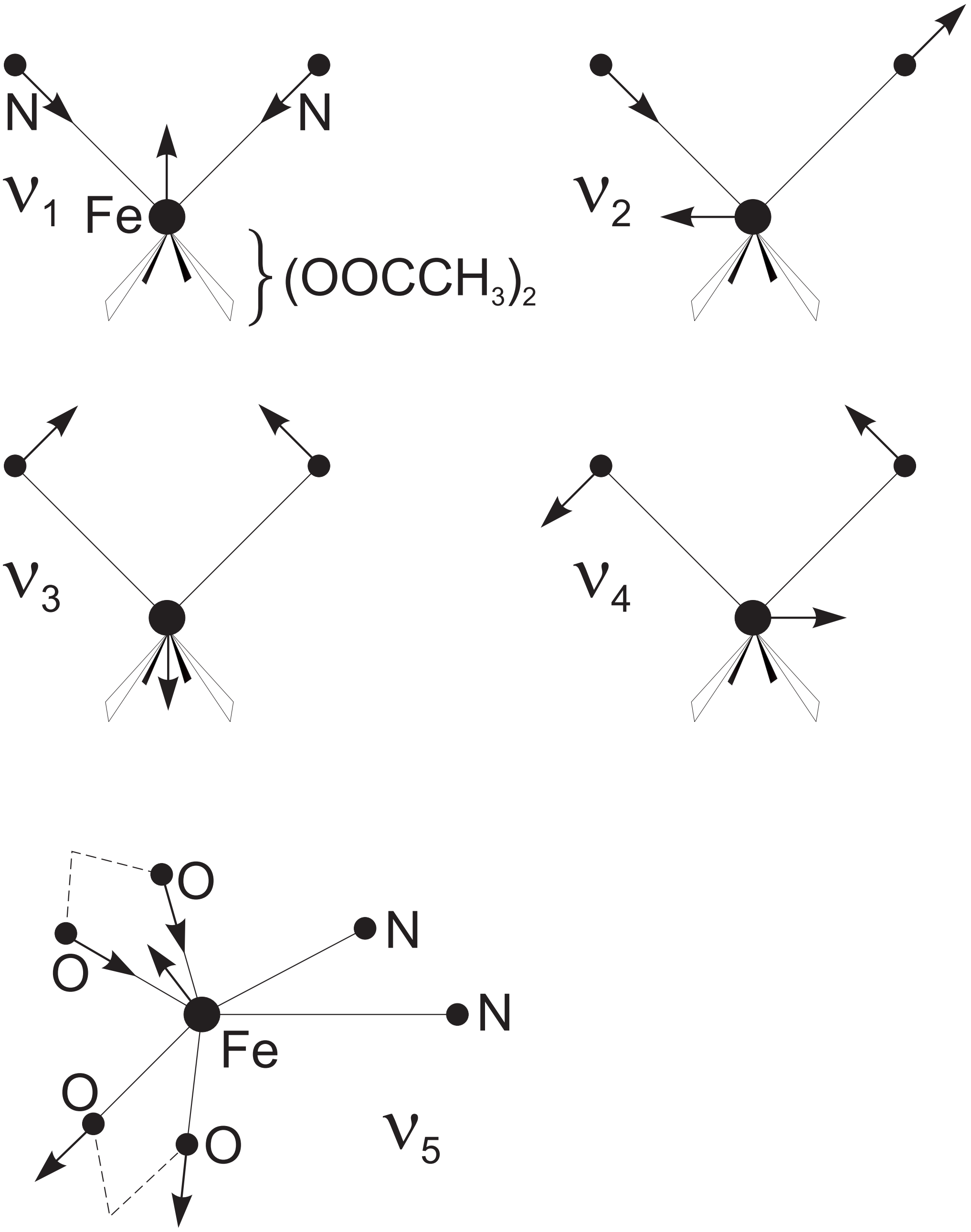
N
N
ν1
Fe
(OOCCH3)2
ν2
ν3
ν4
O
N
O
N
Fe
O
O
ν5

Figure B.4: Some iron vibrational modes of the molecule shown in fig. 7.3.

List of Figures

2.1 Schematic representation of the nuclear resonance transition between excited E_{e} and ground E_{g} states in two isolated nuclei. The ground state has $\Delta E = 0$ and the full width at half maximum of the spectral transition line is Γ_{nat}. The two Lorentzian lines (emission and absorption) are separated by $2E_{\mathrm{R}} \approx 10^6\Gamma_{\mathrm{nat}}$. 7

2.2 The nuclear decay scheme for ${}^{57}_{27}\mathrm{Co}$–${}^{57}_{26}\mathrm{Fe}$ and various backscattering processes that can follow resonant absorption of an incident γ-photon, modified from [8]. Approximately 12.3% (=(10.7+1.6)/99.8, γ and EC are the gamma and electron capture emission probabilities, respectively, per 100 disintegrations) of the deexcitations from the 136.5 keV state that occurs directly to the ground state. The remaining 87.7% (=(85.5+2.0)/99.8) decay occurs via the 14.4 keV level to the ground state. Of the 14.4 keV transitions, only 10.5% (=9.2/(9.2+78.6)) result in emission of a γ-ray, whereas the remaining 89.5% result in transfer of the transition energy to an atomic electron causing conversion electron emission, which leads to K-α_1 and K-α_2 X-ray emission. Values of EC and γ are taken from [9]. 9

2.3 The nuclear levels are shifted without changing the degeneracy due to a finite electron density at the nucleus. Isomer shift δ is the difference in the shifts of nuclear levels of absorber and source, i.e. $\delta = (E_{\mathrm{A}} - E_{\mathrm{S}}) = (\Delta E_{\mathrm{e}} - \Delta E_{\mathrm{g}})_{\mathrm{A}} - (\Delta E_{\mathrm{e}} - \Delta E_{\mathrm{g}})_{\mathrm{S}}$. The schematic Mössbauer spectrum shown on the right displays a positive δ. 15

2.4 The nuclear excited state I_e is split into two substates $|3/2, \pm 3/2\rangle$ and $|3/2, \pm 1/2\rangle$ (magnitude of splitting is equal for both states) by quadrupole interaction energy. The schematic Mössbauer spectrum with two peaks corresponding to two substate transitions along with negative δ is shown on the right. 17

3.1 Schematic of a transmission Mössbauer spectrometer. The energy of the γ-ray is tuned by moving the source relative to the sample. The collimator $d/(2L)$ ratio is 0.07 (for other relevant information see section 3.4). Although the diameter ϕ of the detector window is 25 mm, only ϕ of 7.12 mm is visible to the source, therefore the effective radius of the detector window is $r_\mathrm{eff} = 3.56$ mm. 20

3.2 PHS of ^{57}Co source and the experimental count rate for the 14.4 keV peak is 2502 counts s^{-1} (=area/time). The peak's lower and upper limit which is indicated as vertical bars corresponds to 125–220 mV. The peak parameters in the plot are obtained by fitting the peak between 102 and 180 channel with a Gaussian function. The detector resolution for the peak is FWHM/position=16.8%. The broad peak corresponds to ∼21 keV, which is the K-α X-ray emission from the source matrix, i.e. rhodium. 23

3.3 Front view of the Mössbauer spectrometer with safety shutter moved outside the γ-ray axis. The sample is placed via the top door. The front door is removed for taking the photo. 25

3.4 Pure magnetic hyperfine (i.e. $H \neq 0$ and $V_{zz} = 0$) structure of ^{57}Fe. For $\epsilon = 0$, all the excited substates are equidistant, whereas in the case when both interactions ($H \neq 0$ and $V_{zz} \neq 0$) are present, the excited substates are shifted by $4\epsilon = eQV_{zz} = (p_6 - p_5) - (p_2 - p_1)$. If $V_{zz} < 0$, the substates $|+3/2\rangle$ and $|-3/2\rangle$ are lowered and the other two substates are raised. On the right the Mössbauer spectrum of the α-Fe foil at RT is shown. The experimental count rate excluding the Mössbauer effect is 908 counts s^{-1} (=baseline×512/time). This spectrum was measured immediately after measuring the PHS and fixing the range for the 14.4 keV peak as shown in fig. 3.2. 27

4.1 Emission of synchrotron radiation from a accelerated electron moving radially for nonrelativistic (top left) and relativistic velocities (top right), $1/\gamma = 8.46 \times 10^{-5}$ rad is the opening angle of the radiation cone. Schematic of an undulator (bottom) that forces the electrons on a sinusoidal trajectory. λ_u and g are the adjustable parameters of the undulator for controlling the beam (figures taken from [23]). 33

4.2 Top: schematic sketch of a NIS setup. Bottom: As an example, the NIS spectrum (right) recorded by detector-1 and instrumental function recorded by detector-2 (left) of a trinuclear complex shown in fig. 6.1. Note the phonon annihilation part in the NIS spectrum is close to zero. 35

4.3 Synopsis of the time evolution of the scattered intensity of a material that contains the resonant nucleus after excitation by a synchrotron pulse. 36

4.4 Left: liquid sample holder with a small hole $\phi = 1.5$ mm for injecting the sample liquid; middle: powder sample holder pre-glued on two sides with a kapton foil before loading the powders; right: holder for mounting solid sample in the form of a 8 mm disc. 38

5.1 Reaction scheme of the Fe(III)-catalyzed Michael reaction. 46

5.2 Proposed reaction mechanism of the Fe(III)-catalyzed Michael reaction [55]. 47

5.3 Comparison of Raman and NIS spectra for solid $[N(CH_3)_4][FeCl_4]$. The Raman data were obtained at RT and the NIS at 70 K. 51

5.4 Experimental (at 20 K) and DFT predicted VDOS of solid $Fe(acac)_3$. 52

5.5 Experimental VDOS of the three solid reference compounds $Fe(acac)_3$, $FeCl_3 \cdot 6H_2O$ and $[N(CH_3)_4][FeCl_4]$, together with the spectrum of $FeCl_3 \cdot 6H_2O$ in CPEH at 70 K. The upper curves are offset for clarity. 52

5.6 Experimental VDOS of a frozen solution of $FeCl_3 \cdot 6H_2O$ in CPEH at 20 K and the theoretical VDOS of $Fe_2Cl_7{}^-$ (B3LYP). 53

5.7 Complexes treated by DFT calculations. The geometries optimized using the BP86 functional are shown; however, the geometries as obtained by B3LYP are almost identical. 54

5.8 Experimental VDOS of the frozen reaction mixture of $FeCl_3 \cdot 6H_2O$ in CPEH and the DFT calculations of the species depicted in fig. 5.7. The upper curve is offset for clarity of representation. 54

6.1 Top: Preparation of trinuclear iron complex ($n = 2$). Bottom: Catalytic oxidation of cyclohexene under Gif type conditions. The Gif mixture is the mixture of pyridine, acetic acid and zinc. 58

6.2 Schematic drawing of a teflon sample holder used for low-temperature Mössbauer measurements. The sample liquid is taken in a syringe and transferred to the bottom part (right). Then the top part (left) is inserted onto the bottom part before freezing. The top part, which also avoids the movement of the frozen liquid after freezing, has a microhole so as to facilitate the escape of air while inserting. The top part shown here contains a small cut for better understanding of geometry, however, in real sample holders there is no such cut. 59

6.3 Mössbauer spectrum of the trinuclear iron catalyst at RT (top) and 4.2 K (bottom). 62

6.4 Mössbauer spectrum of catalyst in pyridine (sample 2) and in a mixture of pyridine and acetic acid (sample 3) at 4.2 K. 63

6.5 Mössbauer spectrum of the active catalyst, i.e. the iron catalyst in a mixture of pyridine, acetic acid and zinc under inert (sample 4) and open atmosphere (sample 5) at 4.2 K. 67

6.6 Mössbauer spectrum of the active catalyst with cyclohexene prepared under inert atmosphere (sample 6) and reaction after 1 min (sample 7) at 4.2 K. The doublet 1 in sample 6 is almost buried in noise and has large fit error (standard deviation) for all Mössbauer parameters and therefore this feature is not significant for our analysis. 68

6.7 Mössbauer spectrum of the reaction after 5 min (sample 8) and after 30 min (sample 9) at 4.2 K. 69

6.8 Overview of Mössbauer spectra of samples 1 and 4–9. 70

7.1 DFT optimized structure of the core $[(Fe_3O)(OOCH)_6(H_2O)_3]^+$ of the trinuclear iron complex. Atoms that are not labelled are hydrogen. . . 76

7.2 Experimental ^{57}Fe VDOS of trinuclear complex with $n = 2$ (top), VDOS respresented in terms of the integrand $E^2 g(E)$ of the mean Fe−ligand bond stiffness using eq. (7.1) (center), and DFT calculated VDOS of the core of the trinuclear iron compound (shown in fig. 7.1) together with the experimental VDOS of another trinuclear complex with $n = 3$ (bottom). The dashed curves represent the results of a fit of the VDOS to a series of Lorentzian peaks. The experimental VDOS in the bottom panel is offset for clarity of representation. 80

7.3 Structure of a possible monomer $[Fe(C_5H_5N)_2(O_2CCH_3)_2)]^+$, i.e. sample 3, based on DFT calculations. Atoms that are not labelled are hydrogen. 84

7.4 Experimental ^{57}Fe VDOS of sample 3 prepared from complex with $n = 2$ (top), VDOS represented in terms of the integrand $E^2 g(E)$ of the mean Fe−ligand bond stiffness using eq. (7.1) (center), and DFT calculated VDOS of the possible monomer (shown in fig. 7.3) together with the experimental VDOS of sample 3 prepared from the complex with $n = 3$ (bottom). The dashed curves represent the results of a fit of the VDOS to a series of Lorentzian peaks. The experimental VDOS in the bottom panel is offset for clarity of representation. 85

7.5 Experimental ^{57}Fe VDOS of trinuclear complex ($n = 2$) in pyridine (sample 2) at 20 K. 88

7.6 Structure of a possible active catalyst $Fe^{2+}(C_5H_5N)_4(O_2CCH_3)_2$, i.e. sample 4, based on DFT calculations (spin state 2; multiplicity 5). Atoms that are not labelled are hydrogen. 89

7.7 Experimental ^{57}Fe VDOS of sample 4 prepared from complex with $n = 3$ (top), VDOS respresented in terms of the integrand $E^2 g(E)$ of the mean Fe−ligand bond stiffness using eq. (7.1) (center), and DFT calculated VDOS of the possible monomer (shown in fig. 7.6) together with the experimental VDOS of sample 4 prepared from the complex with $n = 2$ (bottom). The dashed curves represent the results of a fit of the VDOS to a series of Lorentzian peaks. The experimental VDOS in the bottom panel is offset for clarity of representation. 90

7.8 Experimental ^{57}Fe VDOS of trinuclear complex ($n = 2$) in a mixture of pyridine, acetic acid, metallic zinc and cyclohexene under inter atmosphere (sample 6, Gif reaction at zero time) at 20 K. 93

8.1 Molecular structure (left) and simplified bond structure (right) of the trinuclear complex [83]. Selected interatomic distances (Å): Fe1−Fe2 3.36, Fe2−Fe3 3.37, Fe1−Fe3 3.44, Fe1−O=Fe3−O 1.99 and Fe2−O 1.89. The perchlorate anion is not shown. 96
8.2 Mössbauer spectrum of the trinuclear iron complex at RT [115]. . . . 98
8.3 Experimental ^{57}Fe VDOS of the trinuclear iron complex at 20 K. The thin curves represent the results of a fit of the VDOS to a series of Lorentzian peaks. The DFT calculated VDOS for an isolated ion (bottom). 100
8.4 Raman spectrum of the trinuclear iron complex at RT. 104

B.1 Normal modes of vibration for a D_{3h} symmetry [118]. Modes shown in the first and center row are genuine molecular vibrations and the modes shown in bottom are rotational vibrations. The modes ν_2 and ν_3 are doubly degenerate and their respective partners are ν_5 and ν_6. The three translational modes are not shown. The atoms marked as " + " and " − " represents out-of-plane motions. 120
B.2 Normal modes of vibration for a D_{4h} symmetry [75, 119]. The modes ν_6 and ν_7 are doubly degenerate and their respective partners are ν_9 and ν_8. The three translational and rotational modes are not shown. The atoms marked as " + " and " − " represents out-of-plane motions. 121
B.3 Normal modes of vibration for a D_{4h} symmetry of a trans FeN_4O_2 molecule. The E_u modes displayed here are O-Fe-O bend type. The remaining nine modes are shown in fig. B.2 where the FeO_4 unit should be thought of FeN_4. 122
B.4 Some iron vibrational modes of the molecule shown in fig. 7.3. 123

List of Tables

3.1 Geometry of the Mössbauer spectrometer and source properties. . . . 26

4.1 Comparison between a third-generation undulator synchrotron source and a commercially available ^{57}Co Mössbauer source with 10 mCi activity (values taken from [26]). The “ ph ” stands for photons. . . . 32

5.1 Experimental vibrational wavenumbers obtained from NIS ($[N(CH_3)_4][FeCl_4]$), Raman ($[Et_4N][FeCl_4]$) and Fe−Cl bond length from X-ray diffraction (XRD) ($[(CH_3)_4N][FeCl_4]$), together with various theoretically predicted data for anion $[FeCl_4]^-$. 50

6.1 Sample numbering and preparation scheme. 60

6.2 Mössbauer parameters of all samples at 4.2 K unless specified obtained from fitting using Lorentzian line shapes. The numerical values enclosed in parentheses are isomer shifts δ relative to ^{57}Co source at 4.2 K [91]. The δ, quadrupole splitting ΔE_Q and full width at half maximum Γ are given in mm s^{-1}. All samples are numbered in the same scheme as shown in table 6.1. 65

7.1 Summary of NIS on trinuclear iron complex ($n = 2$) and DFT calculation for $[(Fe_3O)(OOCH)_6(H_2O)_3]^+$. Only the normal modes with significant iron vibrational displacement are listed in the fourth column. The mode composition factor e_j^2 and the force constant (FC) of Fe−ligand bond are calculated according to (7.4) and (7.1), respectively. 78

7.2 Assignments and summary of some NIS-based and DFT-calculated wavenumbers for sample 3. The mode composition factor e_j^2 and force constant (FC) of the Fe−ligand bond calculated according to (7.4) and (7.1), respectively. Details of the fitting procedure are described in the text, see section 7.5. 87
7.3 Summary and assignments of some NIS-based and DFT-calculated wavenumbers for sample 4. The mode composition factor e_j^2 and force constant (FC) of the Fe−ligand bond calculated according to (7.4) and (7.1), respectively. Details of the fitting procedure are described in the text, see section 7.5. 91

8.1 Mössbauer parameters for trinuclear complex. 99
8.2 Summary of NIS and calculated vibrational wavenumbers of trinuclear iron complex. 101
8.3 Summary of some NIS, Raman and calculated vibrational wavenumbers of trinuclear iron complex. 105

B.1 Correlation between the normal modes of vibration of three planar D_{4h} (FeO_4 group) interacting under D_{3h} (Fe_3O group) symmetry [98]. . . 119

Bibliography

[1] J. A. Kovacs, Science **299**, 1024 (2003).

[2] L. Que, Jr. and W. B. Tolman, Nature **455**, 333 (2008).

[3] M. Högbom and P. Nordlund, FEBS Lett. **567**, 179 (2004).

[4] V. Schünemann and H. Winkler, Rep. Prog. Phys. **63**, 263 (2000).

[5] S. J. Lippard and J. M. Berg, *Principles of Bioinorganic Chemistry*, University Science Books, Mill Valley, California, 1994.

[6] G. Klingelhöfer, B. Bernhardt, J. Foh, U. Bonnes, D. Rodionov, P. A. de Souza, Ch. Schröder, R. Gellert, S. Kane, P. Gütlich, and E. Kankeleit, Hyperfine Interact. **144/145**, 371 (2002).

[7] R. L. Mössbauer, Z. Phys. **151**, 124 (1958).

[8] E. De Grave, R. E. Vandenberghe, and C. Dauwe, Hyperfine Interact. **161**, 147 (2005).

[9] M.-M. Bé, V. Chisté, C. Dulieu, E. Browne, V. Chechev, N. Kuzmenko, R. Helmer, A. Nichols, E. Schönfeld, and R. Dersch, *Monographie BIPM-5, Table of Radionuclides*, Vol. 1, Internet: http://www.nucleide.org, 2004.

[10] V. Weisskopf and E. Wigner, Z. Phys. **63**, 54 (1930).

[11] T. E. Cranshaw, J. Phys. E: Sci. Instrum. **7**, 122 (1974).

[12] T.-M. Lin and R. S. Preston, Comparison of Techniques for Folding and Unfolding Mössbauer Spectra for Data Analysis, In *Mössbauer Effect Methodology*, Edited by I. J. Gruverman, C. W. Seidel, and D. K. Dieterly, Vol. 9, pp. 205–224, Plenum Press, New York, 1974.

[13] P. Gütlich, R. Link, and A. Trautwein, *Mössbauer Spectroscopy and Transition Metal Chemistry*, Springer-Verlag, Berlin, 1978.

[14] G. K. Shenoy, J. M. Friedt, H. Maletta, and S. L. Ruby, Curve Fitting and the Transmission Integral: Warnings and Suggestions, In *Mössbauer Effect Methodology*, Edited by I. J. Gruverman, C. W. Seidel, and D. K. Dieterly, Vol. 9, pp. 277–305, Plenum Press, New York, 1974.

[15] P. Gütlich, Mössbauer Spectroscopy in Chemistry, In *Mössbauer Spectroscopy*, Edited by U. Gonser, Vol. 5 of *Topics in Applied Physics*, Springer-Verlag, Berlin, 1975.

[16] A. Vértes, L. Korecz, and K. Burger, *Mössbauer Spectroscopy*, pp. 36–40, Elsevier Scientific Publishing Company, Amsterdam, 1979.

[17] A. Abragam, *The Principles of Nuclear Magnetism*, Chapter: Electron-Nuclear Interactions, Oxford University Press, London, 1961.

[18] R. L. Collins, J. Chem. Phys. **42**, 1072 (1965).

[19] F. Aramu and V. Maxia, Nucl. Instrum. Methods **80**, 35 (1970).

[20] U. van Bürck, personal communication.

[21] M. J. Berger, J. H. Hubbell, S. M. Seltzer, J. Chang, J. S. Coursey, R. Sukumar, D. S. Zucker, and K. Olsen, XCOM: Photon Cross Sections Database, Internet: http://physics.nist.gov/PhysRefData/Xcom/Text/XCOM.html.

[22] G. Pedrazzi, S. Vaccari, and E. Papotti, Health Phys. **91**, 163 (2006).

[23] R. Röhlsberger, *Nuclear Condensed Matter Physics with Synchrotron Radiation*, Vol. 208 of *Springer Tracts in Modern Physics*, Springer-Verlag, Berlin, 2004.

[24] K. S. Singwi and A. Sjölander, Phys. Rev. **120**, 1093 (1960).

[25] W. M. Visscher, Ann. Phys. **9**, 194 (1960).

[26] W. Sturhahn, E. E. Alp, T. S. Toellner, P. Hession, M. Hu, and J. Sutter, Hyperfine Interact. **113**, 47 (1998).

[27] F. R. Elder, A. M. Gurewitsch, R. V. Langmuir, and H. C. Pollock, Phys. Rev. **71**, 829 (1947).

[28] F. R. Elder, A. M. Gurewitsch, R. V. Langmuir, and H. C. Pollock, J. App. Phys. **18**, 810 (1947).

[29] S. L. Ruby, J. Phys. Colloques **35**, 209 (1974).

[30] E. Gerdau, R. Rüffer, H. Winkler, W. Tolksdorf, C. P. Klages, and J. P. Hannon, Phys. Rev. Lett. **54**, 835 (1985).

[31] M. Seto, Y. Yoda, S. Kikuta, X. W. Zhang, and M. Ando, Phys. Rev. Lett. **74**, 3828 (1995).

[32] W. Sturhahn, T. S. Toellner, E. E. Alp, X. Zhang, M. Ando, Y. Yoda, S. Kikuta, M. Seto, C. W. Kimball, and B. Dabrowski, Phys. Rev. Lett. **74**, 3832 (1995).

[33] A. I. Chumakov, R. Rüffer, H. Grünsteudel, H. F. Grünsteudel, G. Grübel, J. Metge, O. Leupold, and H. A. Goodwin, Europhys. Lett. **30**, 427 (1995).

[34] R. Rüffer and A. I. Chumakov, Hyperfine Interact. **97/98**, 589 (1996).

[35] A. I. Chumakov and W. Sturhahn, Hyperfine Interact. **123/124**, 781 (1999).

[36] A. Q. R. Baron, Hyperfine Interact. **125**, 29 (2000).

[37] A. I. Chumakov, R. Rüffer, A. Q. R. Baron, H. Grünsteudel, H. F. Grünsteudel, and V. G. Kohn, Phys. Rev. B **56**, 10758 (1997).

[38] V. G. Kohn, A. I. Chumakov, and R. Rüffer, Phys. Rev. B **58**, 8437 (1998).

[39] W. Marshall and S. W. Lovesey, *Theory of Thermal Neutron Scattering*, Oxford University Press, Oxford, 1971.

[40] A. Chumakov and R. Rüffer, Hyperfine Interact. **113**, 59 (1998).

[41] H. J. Lipkin, Ann. Phys. **9**, 332 (1960).

[42] A. I. Chumakov, R. Rüffer, A. Q. R. Baron, H. Grünsteudel, and H. F. Grünsteudel, Phys. Rev. B **54**, R9596 (1996).

[43] W. Sturhahn and A. Chumakov, Hyperfine Interact. **123/124**, 809 (1999).

[44] A. I. Chumakov, personal communication.

[45] X. Zhang, Y. Yoda, M. Seto, Y. Maeda, M. Ando, and S. Kikuta, Jpn. J. Appl. Phys. **34**, L330 (1995).

[46] Gy. Vankó, L. Bottyán, D. L. Nagy, E. Szilágyi, and A. Vértes, J. Radioanal. Nucl. Chem. **246**, 97 (2000).

[47] J. T. Sage, S. M. Durbin, W. Sturhahn, D. C. Wharton, P. M. Champion, P. Hession, J. Sutter, and E. E. Alp, Phys. Rev. Lett. **86**, 4966 (2001).

[48] B. M. Leu, N. J. Silvernail, M. Z. Zgierski, G. R. A. Wyllie, M. K. Ellison, W. R. Scheidt, J. Zhao, W. Sturhahn, E. E. Alp, and J. T. Sage, Biophys. J. **92**, 3764 (2007).

[49] B. M. Leu, T. H. Ching, J. Zhao, W. Sturhahn, E. E. Alp, and J. T. Sage, J. Phys. Chem. B **113**, 2193 (2009).

[50] K. L. Adams, S. Tsoi, J. Yan, S. M. Durbin, A. K. Ramdas, W. A. Cramer, W. Sturhahn, E. E. Alp, and C. Schulz, J. Phys. Chem. B **110**, 530 (2006).

[51] Y. Guo, H. Wang, Y. Xiao, S. Vogt, R. K. Thauer, S. Shima, P. I. Volkers, T. B. Rauchfuss, V. Pelmenschikov, D. A. Case, E. E. Alp, W. Sturhahn, Y. Yoda, and S. P. Cramer, Inorg. Chem. **47**, 3969 (2008).

[52] S. J. George, R. Y. Igarashi, Y. Xiao, J. A. Hernandez, M. Demuez, D. Zhao, Y. Yoda, P. W. Ludden, L. M. Rubio, and S. P. Cramer, J. Am. Chem. Soc. **130**, 5673 (2008).

[53] V. S. Oganesyan, J. E. Barclay, S. M. Hardy, D. J. Evans, C. J. Pickett, and U. A. Jayasooriya, Chem. Commun., 214, (2004).

[54] J. Christoffers, Synlett **2001**, 723 (2001).

[55] S. Pelzer, Th. Kauf, C. van Wüllen, and J. Christoffers, J. Organomet. Chem. **684**, 308 (2003).

[56] J. Christoffers, Michael Addition, In *Encylopedia of Catalysis*, Edited by I. T. Horváth, Vol. 5, pp. 99–118, John Wiley & Sons, Inc., New Jersey, 2003.

[57] M. Bauer, Th. Kauf, J. Christoffers, and H. Bertagnolli, Phys. Chem. Chem. Phys. **7**, 2664 (2005).

[58] C. Trage, D. Schröder, and H. Schwarz, Chem. Eur. J. **11**, 619 (2005).

[59] Th. Kauf, *Funktionalisierung von β-Dicarbonylverbindungen mit Eisen- und Cer-Katalysatoren*, Dissertation, Universität Stuttgart, 2006.

[60] V. G. Kohn and A. I. Chumakov, Hyperfine Interact. **125**, 205 (2000).

[61] C. Lee, W. Yang, and R. G. Par, Phys. Rev. B **37**, 785 (1988).

[62] A. D. Becke, J. Chem. Phys. **98**, 5648 (1993).

[63] A. D. Becke, Phys. Rev. A **38**, 3098 (1988).

[64] J. P. Perdew, Phys. Rev. B **33**, 8822 (1986).

[65] M. J. Frisch, G. W. Trucks, H. B. Schlegel, G. E. Scuseria, M. A. Robb, J. R. Cheeseman, J. A. Montgomery, Jr., T. Vreven, K. N. Kudin, J. C. Burant, J. M. Millam, S. S. Iyengar, J. Tomasi, V. Barone, B. Mennucci, M. Cossi, G. Scalmani, N. Rega, G. A. Petersson, H. Nakatsuji, M. Hada, M. Ehara, K. Toyota, R. Fukuda, J. Hasegawa, M. Ishida, T. Nakajima, Y. Honda, O. Kitao, H. Nakai, M. Klene, X. Li, J. E. Knox, H. P. Hratchian, J. B. Cross, V. Bakken, C. Adamo, J. Jaramillo, R. Gomperts, R. E. Stratmann, O. Yazyev, A. J. Austin, R. Cammi, C. Pomelli, J. W. Ochterski, P. Y. Ayala, K. Morokuma, G. A. Voth, P. Salvador, J. J. Dannenberg, V. G. Zakrzewski, S. Dapprich, A. D. Daniels, M. C. Strain, O. Farkas, D. K. Malick, A. D. Rabuck, K. Raghavachari, J. B. Foresman, J. V. Ortiz, Q. Cui, A. G. Baboul, S. Clifford, J. Cioslowski, B. B. Stefanov, G. Liu, A. Liashenko, P. Piskorz, I. Komaromi, R. L. Martin, D. J. Fox, T. Keith, M. A. Al-Laham, C. Y. Peng, A. Nanayakkara, M. Challacombe, P. M. W. Gill, B. Johnson, W. Chen, M. W. Wong, C. Gonzalez, and J. A. Pople, *Gaussian 03*, Revision E.01, Gaussian, Inc., Wallingford CT, 2004.

[66] T. H. Dunning, Jr., J. Chem. Phys. **90**, 1007 (1989).

[67] M. Dolg, U. Wedig, H. Stoll, and H. Preuss, J. Chem. Phys. **86**, 866 (1987).

[68] A. Schäfer, H. Horn, and R. Ahlrichs, J. Chem. Phys. **97**, 2571 (1992).

[69] H. Paulsen, H. Winkler, A. X. Trautwein, H. Grünsteudel, V. Rusanov, and H. Toftlund, Phys. Rev. B **59**, 975 (1999).

[70] T. Asthalter, Z. Phys. Chem. **220**, 979 (2006).

[71] M. C. Smith, Y. Xiao, H. Wang, S. J. George, D. Coucouvanis, M. Koutmos, W. Sturhahn, E. E. Alp, J. Zhao, and S. P. Cramer, Inorg. Chem. **44**, 5562 (2005).

[72] D. Wyrzykowski, R. Kruszyński, J. Kłak, J. Mroziński, and Z. Warnke, Inorg. Chim. Acta **361**, 262 (2008).

[73] J. S. Avery, C. D. Burbridge, and D. M. L. Goodgame, Spectrochim. Acta **24A**, 1721 (1968).

[74] M. S. Sitze, E. R. Schreiter, E. V. Patterson, and R. G. Freeman, Inorg. Chem. **40**, 2298 (2001).

[75] K. Nakamoto, *Infrared and Raman Spectra of Inorganic and Coordination Compounds*, John Wiley & Sons, Inc., New York, third edition, 1978.

[76] M. Mikami, I. Nakagawa, and T. Shimanouchi, Spectrochim. Acta **23A**, 1037 (1967).

[77] K. Nakamoto, C. Udovich, and J. Takemoto, J. Am. Chem. Soc. **92**, 3973 (1970).

[78] G. Schaftenaar and J. H. Noordik, J. Comput.-Aided Mol. Des. **14**, 123 (2000).

[79] T. Asthalter, S. Rajagopalan, Th. Kauf, V. Rabe, and J. Christoffers, J. Phys. Chem. A **112**, 11514 (2008).

[80] I. Schlichting, J. Berendzen, K. Chu, A. M. Stock, S. A. Maves, D. E. Benson, R. M. Sweet, D. Ringe, G. A. Petsko, and S. G. Sligar, Science **287**, 1615 (2000).

[81] T. Punniyamurthy, S. Velusamy, and J. Iqbal, Chem. Rev. **105**, 2329 (2005).

[82] P. Stavropoulos, R. Ç.-Çetin, and A. E. Tapper, Accounts Chem. Res. **34**, 745 (2001).

[83] V. Rabe, W. Frey, A. Baro, S. Laschat, M. Bauer, H. Bertagnolli, S. Rajagopalan, T. Asthalter, E. Roduner, H. Dilger, T. Glaser, and D. Schnieders, Eur. J. Inorg. Chem. **2009**, 4660 (2009).

[84] D. H. R. Barton, J. Boivin, M. Gastiger, J. Morzycki, R. S. H.-Motherwell, W. B. Motherwell, N. Ozbalik, and K. M. Schwartzentruber, J. Chem. Soc., Perkin Trans. 1, 947 (1986).

[85] V. Rabe, *Neue nicht-Häm-Eisenkomplexe: Synthese, spektroskopische Charakterisierung und Anwendung in der katalytischen aeroben C-H-Oxidation*, Dissertation, Universität Stuttgart, 2009.

[86] R. D. Cannon and R. P. White, Chemical and Physical Properties of Triangular Bridged Metal Complexes, In *Progress in Inorganic Chemistry*, Edited by S. J. Lippard, Vol. 36, pp. 195–298, John Wiley & Sons, Inc., New York, 1988.

[87] M. Takano, J. Phys. Soc. Jpn. **33**, 1312 (1972).

[88] S. J. Lippard, Angew. Chem. Int. Ed. **27**, 344 (1988).

[89] S. Mørup, *Paramagnetic and Superparamagnetic Relaxation Phenomena studied by Mössbauer Spectroscopy*, Dissertation, Technical University of Denmark, 1980.

[90] S. Mørup, Relaxation Phenomena in Frozen Solutions, In *Mössbauer Spectroscopy of Frozen Solutions*, Edited by A. Vértes and D. L. Nagy, pp. 71–113, Akadémiai Kiadó, Budapest, 1990.

[91] S. Rajagopalan, T. Asthalter, V. Rabe, U. van Bürck, F. E. Wagner, and S. Laschat, Hyperfine Interact. **187**, 35 (2008).

[92] M. Blume, Phys. Rev. Lett. **14**, 96 (1965).

[93] M. N. Burnett and C. K. Johnson, *ORTEP-III: Oak Ridge Thermal Ellipsoid Plot Program for Crystal Structure Illustrations*, Oak Ridge National Laboratory Report ORNL-6895, 1996.

[94] Origin, OriginLab, Northampton, MA.

[95] A. I. Chumakov, R. Rüffer, O. Leupold, and I. Sergueev, Struct. Chem. **14**, 109 (2003).

[96] J. T. Sage, C. Paxson, G. R. A. Wyllie, W. Sturhahn, S. M. Durbin, P. M. Champion, E. E. Alp, and W. R. Scheidt, J. Phys.-Condes. Matter **13**, 7707 (2001).

[97] N. W. Ashcroft and N. D. Mermin, *Solid State Physics*, Thomson Learning, Inc., Singapore, college edition, 1976.

[98] M. K. Johnson, D. B. Powell, and R. D. Cannon, Spectrochim. Acta **37A**, 995 (1981).

[99] L. Meesuk, U. A. Jayasooriya, and R. D. Cannon, J. Am. Chem. Soc. **109**, 2009 (1987).

[100] A. Karlsson, J. V. Parales, R. E. Parales, D. T. Gibson, H. Eklund, and S. Ramaswamy, Science **299**, 1039 (2003).

[101] M. D. Wolfe, J. V. Parales, D. T. Gibson, and J. D. Lipscomb, J. Biol. Chem. **276**, 1945 (2001).

[102] J.-U. Rohde, J.-H. In, M. H. Lim, W. W. Brennessel, M. R. Bukowski, A. Stubna, E. Münck, W. Nam, and L. Que, Jr., Science **299**, 1037 (2003).

[103] K. Chen, M. Costas, and L. Que, Jr., J. Chem. Soc., Dalton Trans., 672, (2002).

[104] B. Singh, J. R. Long, F. F. de Biani, D. Gatteschi, and P. Stavropoulos, J. Am. Chem. Soc. **119**, 7030 (1997).

[105] L. E. Cox and D. G. Peters, Inorg. Chem. **9**, 1927 (1970).

[106] L. Kocsis, J. Mink, F. Jalilehvand, L. J. Laffin, O. Berkesi, and L. Hajba, J. Raman Spectrosc. **40**, 481 (2009).

[107] C. G.-Walrand, Mol. Phys. **102**, 1361 (2004).

[108] E. M. Holt, S. L. Holt, W. F. Tucker, R. O. Asplund, and K. J. Watson, J. Am. Chem. Soc. **96**, 2621 (1974).

[109] R. D. Cannon, *Electron Transfer Reactions*, Butterworth & Co Ltd., London, 1980.

[110] S. Fukuzumi, Roles of Metal Ions in Controlling Bioinspired Electron-Transfer Systems. Metal Ion-Coupled Electron Transfer, In *Progress in Inorganic Chemistry*, Edited by K. D. Karlin, Vol. 56, pp. 49–153, John Wiley & Sons, Inc., New Jersey, 2009.

[111] A. Triantafillou, *Investigation of Transition Metal Carboxylates using Infrared, Raman and Inelastic Neutron Scattering Spectroscopies*, Dissertation, University of East Anglia, 1993.

[112] J. A. Stride, U. A. Jayasooriya, and J. Eckert, Angew. Chem. Int. Ed. **38**, 116 (1999).

[113] A. K. Boudalis, Y. Sanakis, C. P. Raptopoulou, A. Terzis, J.-P. Tuchagues, and S. P. Perlepes, Polyhedron **24**, 1540 (2005).

[114] P. Gütlich and J. Ensling, Mössbauer spectroscopy, In *Inorganic Electronic Structure and Spectroscopy*, Edited by E. I. Solomon and A. B. P. Lever, Vol. I, pp. 161–211, John Wiley & Sons, Inc., New York, 1999.

[115] S. Rajagopalan, T. Asthalter, V. Rabe, S. Laschat, G. Rauhut, and E. Roduner, J. Phys.: Conf. Ser. **217**, 012030 (2010).

[116] S. M. Gorun, G. C. Papaefthymiou, R. B. Frankel, and S. J. Lippard, J. Am. Chem. Soc. **109**, 4244 (1987).

[117] M. K. Johnson, R. D. Cannon, and D. B. Powell, Spectrochim. Acta **38A**, 307 (1982).

[118] F. A. Cotton, *Chemical Applications of Group Theory*, John Wiley & Sons, Inc., New York, third edition, 1990.

[119] C.-Y. Hsu and M. Orchin, J. Chem. Educ. **51**, 725 (1974).

Acknowledgments

First and foremost I offer my deep and sincerest gratitude to my thesis supervisor Dr Tanja Asthalter for her continuous support and encouragement throughout this work. I also convey respect to her for the enthusiasm to teach me all aspects of the science presented in this thesis. She accompanied me in all Mössbauer and nuclear inelastic scattering measurements in ESRF and München for my research work. More importantly, due to her, I got the opportunity to meet many great scientists and researchers. In addition, I thank her for the reading and corrections of this thesis.

It is a pleasure to thank Prof. Emil Roduner, under whom I worked for the last two years. When I approached him he immediately accepted me in his group and treated me as an integrated member in his group. He contributed a lot to this work by providing me a lot of suggestions and advices during the completion of this work and for the critical reading of this thesis.

I also acknowledge Prof. Helmut Bertagnolli, under whom I was working for the initial two years of this project. He provided me a wonderful pressure-free working atmosphere which allowed me to do this work successfully.

I should thank Dr Volker Rabe for making all the chemical compounds and reactions presented in this thesis and efficient team work in beamtimes. Special thanks go also to Prof. Sabine Laschat, who is responsible for a successful and fruitful SFB collaboration on this project-A3 and for accepting to be the chairperson for the defence of my thesis.

I thank the mechanical workshop people: Mr Thomas Weigend, Mr Walter Ottmüller and Mr Jochen Graf for making the stable and rigid Mössbauer setup, which I had sketched and shown to them and to Mr Jürgen Hußke for making the safety shutter. Special thanks to Prof. Erich Gerdau and his cooworker Dr Hans-Dierk Rüter for offering the Mössbauer parts (including drive and electronics) that enabled us to

set up a spectrometer in our institute. I also thank Dr Olaf Leupold for his vauble advices, which helped us to get good Mössbauer spectra.

My warm thanks to Dr Herbert Dilger for providing the expert advice and clever instructions for handling the Mössbauer radioactive source. I also thank him for the administrative procedures that he had taken in using the Mössbauer radioactive source in the laboratory. My friendly thanks go to Dr Stefan Jagiella for many helps in installing the spectrometer. I also thank Dr Wolf Wölfel and Andreas Schöne for allowing me to use Mössbauer spectrometer of the Physics Department (F-Praktikum) during my very initial stages of this work.

Special thanks to the laboratory assistants Diana Zauser, Birgit Feucht and Gabriele Bräuning for their help in laboratory and to Inge Blankenship, Susan Luginsland, Gisela Hoppe, Isabella Waldner and Dieter Leicht for the administrative help during the course of the work.

I thank the following people for help in computations: Prof. Guntram Rauhut for the helpful discussion on the use of Gaussian 03 software; the computational services offered by the supercomputer center (computers: bwGRiD, kizz, CUSS) at Universität Ulm for all the DFT calculations, especially to Dr Christian Mosch and Mr Thomas Nau who remotely took lot of efforts for running my big calculations and for their tips in using the computational resources in an efficient manner, and Prof. Klaus Müller for offering a computing account to access those remote computers.

My heartfelt thanks to the Mössbauer spectroscopy group: Dr Uwe van Bürck and Prof. Fritz Wagner at Technische Universität München for offering many opportunities to measure our samples. All the high quality spectra presented in this thesis would not have been possible without their help. Special thanks to Uwe van Bürck for his expert tips and tricks of overall instrumental aspect of Mössbauer spectroscopy and for guidance for the fitting procedure of spectra.

I sincerely offer my heartfelt thanks to all the people of the nuclear resonance beamline ID18 at ESRF, Grenoble (France) for giving the opportunity to measure, especially to Dr Sasha Chumakov for the efficient assistance during all NIS experiments and also for explaining the physics of NIS. I also thank the head of the ID18 group, Dr Rudolf Rüffer, for many scientific discussions while performing our experiments. Special thanks also to Dr Ilya Sergueev for his help during our last beamtime visit.

I thank all the colleagues of my group for providing a wonderful working atmosphere, especially to Sankaran and Eric for exchanging many nonscientific as well as

scientific ideas during our short coffee breaks. Special thanks to Fabrizia for making many wonderful pasta parties. I happily thank my family members for everything they have done for me. My friends: Kamal, Arunoday, Gurram, Srikumar, Anjan, Tahira, Sony and Venkata for making many get-to-gather parties during my stay and to my office-mates Alexander, Amga and Christopher for a pleasant working place. Hearty thanks also to my friends at Schwabstraße, where I spent most of my evenings: Siva, Suthan, Prahalatha, Sangeethan and Ramesh for making me to feel like I am in my home in Stuttgart.

Last but not least I thank the Deutsche Forschungsgemeinschaft, within the framework of the collaborative research center-Sonderforschungsbereiche 706 (SFB706-Katalytische Selektivoxidationen von C−H-Bindungen mit molekularem Sauerstoff) and the ‘Ministerium für Wissenschaft, Forschung und Kunst des Landes Baden-Württemberg’ for the generous financial support for this project-A3 from April 2006 to December 2009.

Rajagopalan S.

Curriculum vitae

Personal details

Name: Rajagopalan Subramanian
Date of birth: 13 September 1978
Place of birth: Mayiladuthurai, India
Parents: S. Subramanian and S. Prabhavathy
Siblings: S. Ganesan and S. Sankar

Educational qualifications

1984–1994: Primary schooling at St Josephs Matriculation High School, Maraimalai Nagar, India
1994–1996: Secondary schooling at JG National Higher Secondary School, Tambaram, India
1996–2000: Bachelor of Mechanical Engineering, Adhiparasakthi Engineering College (affiliated to University of Madras, Chennai), Melmaruvathur, India
2002–2005: Masters of Science in Materials Science and Engineering, Christian-Albrechts-Universität zu Kiel, Kiel, Germany
2006–2010: Promotion (Dr. rer. nat.) at Universität Stuttgart, Stuttgart, Germany